Kinetics of polymeric nanoparticulate carriers and cargo under physiological and pathological conditions in the retina

Thesis

for the degree of

doctor rerum naturalium (Dr. rer. nat.)

approved by the Faculty of Natural Sciences of Otto von Guericke University Magdeburg

by MMed Enqi Zhang

born on 30.01.1988 in Nei Mongol (China)

Examiner: Prof. Dr. Bernhard A. Sabel

Prof. Dr. Hans-Joachim Galla

submitted on: 14.07.2021

defended on: 20.01.2022

Abstract

PLGA (poly(lactic-co-glycolic acid))-based nanoparticles (NPs) are promising drug carrier systems because of their excellent biocompatibility. However, it is not well understood how the kinetics of such drug delivery system depends on its cargo. To answer this question, I analyzed the distribution of NP drug carrier systems after intravenous injection with *in vivo* and *ex vivo* fluorescent imaging of the rat retina. In my first project (Study I) I investigated PLGA NPs loaded with fluorescent lipophilic carbocyanine perchlorate (DiI) or hydrophilic Rhodamine 123 (Rho123) and revealed that DiI was partially retained within the NPs circulating in the retinal blood vessels and the released DiI accumulated in the blood vessel walls. In contrast, negligible Rho123 stayed associated with NPs and the dye almost completely disappeared from blood circulation within minutes.

As drug delivery systems will be used for the treatment of diseases, I further investigated the kinetics of PLGA NPs with the lipophilic fluorescent model drug coumarin 6 (Cou6) as cargo in the injured retina after optic nerve crush (ONC). Retina imaging revealed that Cou6 was rapidly released from NPs and penetrated the inner BRB within 15 min. *Ex vivo* microscopy of retinal flat mounts indicated that Cou6 accumulated predominantly in the extracellular space, and to a lesser extent in neurons. Seven days after ONC the area of distribution of Cou6 in ganglion cell layer parenchyma was increased and the elimination of the empty PLGA carrier was accelerated as compared to healthy controls.

In Study III, I adapted a statistical learning method which uses key physiochemical parameters of compounds to predict blood-brain barrier (BBB; similar to blood-retina barrier) passage and applied it to the model drugs DiI, Rho123 and Cou6. This *in silico* approach confirmed that Cou6 passes the BBB, whereas DiI does not. Therefore, the *in silico* approach is suitable to predict some aspects of the drug delivery process.

In conclusion, the temporal and spatial release pattern and distribution of nano carrier systems are significantly influenced by the properties of loaded compounds, the blood milieu and normal vs pathological conditions. These results emphasize the need for an individual *in vivo* profiling of NPs delivery systems depending on their cargo.

Zusammenfassung

Nanopartikels (NPs) basierend auf PLGA (poly(lactic-co-glycolic acid)) sind aufgrund ihrer hervorragenden Biokompatibilität vielversprechende Wirkstoffträgersysteme. Bisher weiß man jedoch noch nicht, wie die Kinetik einer solchen Darreichungsform vom Wirkstoff abhängt. Um diese Frage zu beantworten, analysierte ich die Verteilung von NP-Wirkstoffträgersystemen nach intravenöser Injektion mit fluoreszierender Bildgebung an *in vivo* und *ex vivo* Präparationen der Netzhaut der Ratte. In meinem ersten Projekt (Studie I) untersuchte ich PLGA-NPs, die mit einer fluoreszierenden lipophilen Carbocyaninperchlorat-Verbindung (DiI) oder einer hydrophilen Rhodamin-Verbindung (Rhodamin 123 (Rho123)) beladen waren. Dabei konnte ich zeigen, dass DiI teilweise in den NPs verblieb, die in den Netzhautblutgefäßen zirkulierten, und dass das freigesetzte DiI in den Blutgefäßwänden akkumulierte. Im Gegensatz dazu blieb nur verschwindend wenig Rho123 mit NPs assoziiert, und der Farbstoff verschwand innerhalb von Minuten fast vollständig aus dem Blutkreislauf.

Da Darreichungsformen zur Arzneimittelfreisetzung für die Behandlung von Krankheiten eingesetzt werden, untersuchte ich sodann die Kinetik von PLGA NPs, die mit lipophilem, fluoreszierenden Cumarin 6 (Cou6) als Arzneimittelsurrogat beladen waren, in der nach Sehnerv Quetschung (optic nerve crush; ONC) verletzten Netzhaut. Die Retina-Bildgebung ergab, dass Cou6 schnell aus NPs freigesetzt wurde und innerhalb von 15 Minuten die Gefäßwände der retinalen Blutadern überwand. *Ex-vivo*-Mikroskopie von retinalen Flachpräparaten zeigte, dass Cou6 vorwiegend im extrazellulären Raum des Retinagewebes und in geringerem Maße in Neuronen akkumulierte. Sieben Tage nach ONC war der Verteilungsbereich von Cou6 in der Ganglienzellenschicht vergrößert und die Eliminierung des leeren PLGA-Trägers im Blut im Vergleich zu gesunden Kontrollen beschleunigt.

In Studie III habe ich einen statistischen Lernalgorithmus angepasst, der anhand wichtiger physiochemischer Parameter von chemischen Verbindungen die Passage

über die Blut-Hirn-Schranke (BHS; ähnlich der Blut-Netzhaut-Schranke) vorhersagt. Diesen Algrorithmus habe ich bei den Modellsubstanzen DiI, Rho123 und Cou6 angewendet. Dieser *In-Silico*-Ansatz bestätigte, dass Cou6 die BHS überwinden kann, DiI jedoch nicht. Dieser Ansatz ist daher geeignet, einige Aspekte der Arzneimittelverteilung vorherzusagen.

Zusammenfassend lässt sich sagen, dass das zeitliche und räumliche Freisetzungsmuster und die Verteilung von Nanoträgersystemen maßgeblich von den Eigenschaften transportierten Wirkstoffe, dem Blutmilieu und normalen vs. pathologischen Bedingungen beeinflusst werden. Diese Ergebnisse unterstreichen die Notwendigkeit einer individuellen *In-vivo*-Charakterisierung von NP-Darreichungsformen in Abhängigkeit von dem transportierten Wirkstoff.

Table of Contents

Abbreviations

BBB	blood-brain barrier
BC	blood cell
BRB	blood-retina barrier
BV	blood vessels
CNS	central nervous system
Cou6	coumarin 6
Cy5.5	cyanine5.5 amine
Cy5.5-PLGA	cy5.5 covalently bound PLGA conjugates
Cy5.5-PLGA-Cou6	cy5.5-PLGA nanoparticles loaded with Coumarin 6
Cy5.5-PLGA-DiI	cy5.5-PLGA nanoparticles loaded with DiI
Cy5.5-PLGA-DiI/P188	cy5.5-PLGA-DiI nanoparticles coated with poloxamer 188
Cy5.5-PLGA-Rho123	cy5.5-PLGA nanoparticles loaded with rhodamine123
Cy5.5-PLGA-Rho123/P188	cy5.5-PLGA-Rho123 nanoparticles coated with poloxamer 188
DiI	1,1'-dioctadecyl-3,3,3',3'-tetramethylindocarbocyani-ne perchlorate
DLS	dynamic light scattering
EDC	1-ethyl-3-(3-dimethylaminopropyl)carbodiimide
EE	encapsulation efficiency
ELS	electrophoretic light scattering
FBS	fetal bovine serum
FN	false negatives
FP	false positives
GCL	ganglion cell layer
HBA	hydrogen bound acceptors
HBD	hydrogen bound donors

HSA	human Serum Albumin
Hoechst	Hoechst 33342
HTS	high throughput screening
ICON	*in vivo* Confocal Neuroimaging
IOP	inner ocular pressure
MW	molecular weight
NPs	Nanoparticles
ONC	optic nerve crush
P188	poloxamer 188
PBCA	poly(butyl cyanoacrylate)
PCA	principal component analysis
PCC	pearson correlation coefficient
PDI	polydispersity index
PDMAEMA	poly(2-(dimethylamino)ethyl methacrylate)
PLA	polylactic acid
PLGA	poly(lactic-co-glycolic acid)
PLGA-Cou6	PLGA nanoparticles loaded with Coumarin 6
PLGA-DiI	DiI-loaded PLGA nanoparticles
PLGA-DiI/P188	PLGA-DiI nanoparticles coated with poloxamer 188
PLGA-Rho123	rhodamine123-loaded PLGA nanoparticles
PLGA-Rho123/P188	PLGA-Rho123 nanoparticles coated with poloxamer 188
PVA	polyvinyl alcohol
RBC	rotatable bonds count
RGC	retinal ganglion cell
Rho123	rhodamine 123
SEM	scanning electron microscopy
SRCC	Spearman’s rank correlation coefficient
SVM	support vector machine
TEM	transmission electron microscopy

TLC	thin layer chromatography
TN	true negatives
TON	traumatic optic neuropathy
TOS	overlap score at different threshold
TOS_h	threshold overlap score at the highest intensity
TP	true positives
TPSA	topological polar surface area

List of Figures

List of supplementary Figure

List of Tables

List of Supplementary Tables

1. General Introduction

The basic aim of my work was to understand how nanoparticles (NPs) deliver their cargoes in the healthy and diseased central nervous system tissue. Therefore, I studied several areas of research, ranging from neuropathology to nanoparticle engineering. This chapter will give an introduction into the retina model and nanoparticles used, the anatomical, physiological and pathological details which are important for understanding the distribution of the nanosystems in the different compartments, and the reason why the study of biological environments in life or organisms is important. They will provide insight into the basics and applicability of nanoparticle chemistry and engineering.

1.1 Retina and optic nerve injury

It is well known that the human eye is one of most significant sensory system and most sensitive organ, as it collects the most information from the external environment (Irsch and Guyton, 2009). The eye includes two part: the anterior segment (cornea, iris, pupil, and crystalline lens etc.) and the posterior segment (vitreous chamber, vitreous body, retina, and choroid etc.). Most of the prevalent eye diseases happen at the posterior eye, especially at the retina (Thrimawithana et al., 2011). The retina is part of the central nervous system (CNS), located in the back of eye, and it is easily approachable (Dowling, 1987). It is a thin layer of light-sensitive tissue which has a highly ordered anatomical organization and contains five types of neurons: photoreceptors, bipolar cells, retinal ganglion cells, horizontal cells and amacrine cells, which are wired together by cell circuit (Holmes, 2018).

Many eye diseases can induce optic nerve injury which will further lead to retrograde degeneration of retinal ganglion cells (RGCs) in the retina and subsequent vision loss which significantly impairs the quality of life of patients (Sabel et al., 2019). In the case of glaucoma, some scientists think that the elevated inner ocular pressure (IOP) can

distort the lamina cribrosa, which subsequently produces shear force and compressive force on the axons of ganglion cells, while others believe that this increased pressure will affect the capillaries, which will alter the blood supply to the optic nerve head and axon damage can happen (Findl et al., 1997; Pillunat et al., 1997; Morgan et al., 1998; Weber et al., 2008). In addition, when IOP is elevated, the optic nerve head glia may release factor such as nitric oxide and tumor necrosis factor α which are neurotoxic and damage the optic nerve (Neufeld et al., 1997; Weber et al., 2008). Along with raised IOP, the rapid rotation and lateral translation of the globe can also cause the optic nerve injury from a blunt object trauma, which is implied by a computer model study (Cirovic et al., 2006). Traumatic optic neuropathy (TON) which refers to the injury to the optic nerve following trauma (1.5% to 4% secondary to the head trauma), is another important cause of vision loss (Guy et al., 2014). After the optic nerve is injured secondary to the trauma, the optic nerve will become more swollen which can induce further damage (Yu-Wai-Man and Griffiths, 2013). In a study on the optic nerve lesions, changes in blood flow to the optic nerve and permeability of micro vessels in streptozotocin induced diabetic rats showed that these rats had atrophic optic nerve fibers, reduced blood flow to the optic nerve and increased microvascular permeability (Zhao et al., 2010). Over the last few decades, the importance of developing efficient treatments against RGCs degeneration that follows an injury to the optic nerve and improve visual recovery has been increasingly recognized.

1.2 Retinal drug delivery

In the ophthalmic field, the retinal drug delivery to treat eye diseases involving optic nerve injury is important but challenging for pharmaceutical scientists. Although visual impairments are mostly caused by disorders affecting the retina and, like abovementioned affects the patient's life quality, the current treatment options for the posterior segments, typically, the retina are not sufficient (Toda et al., 2011). As shown in Figure 1.1, there are four main routes to deliver drugs to the anterior and posterior segments: the topical route, intravitreal route, periocular route, and systemic route

(Bisht et al., 2018). Drugs delivered by the periocular route firstly have to cross the sclera, choroid, and retinal pigment epithelial in order to arrive at the retina (Raghava et al., 2004). Current treatments of eye diseases largely focus on eye drops, which is very efficient to treat the anterior segments of eye. However, when it comes to diseases of the posterior eye segments, delivery of compounds is most restricted because of the corneal, conjunctival barrier, and drainage and tear fluid turnover, and drugs cannot reach the posterior segments sufficiently (Urtti et al., 1990; Toda et al., 2011). Intravitreal injection can overcome these problems achieving high concentrations of drugs in the vitreous and retina. However, this requires repetitive injections which may cause adverse side-effects such as cataracts and endophthalmitis (Raghava et al., 2004; Bisht et al., 2018). Intravenous drug administration is another alternative for the treatment of retinal disorders. Recently, with the development of NPs, a number of NPs-based drug delivery systems have been reported and investigated. However, to be efficient for systemic delivery, the nature of the NPs has to be comprehensively considered: their biodegradability and biocompatibility, their physicochemical properties (e.g., surface charge, size, shape), the existence of complex fluid force, blood components, and structure and function of the inner BRB, which strictly regulates the transportation of NPs from the blood circulation to the target retina.

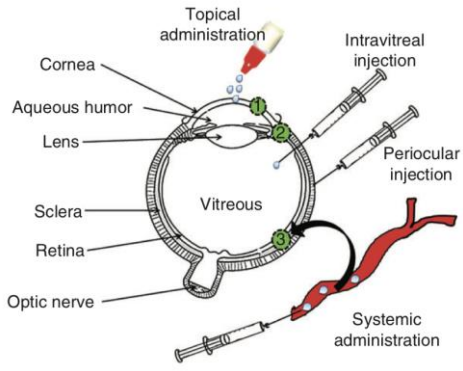

Figure 1.1 Schematic illustration of routes of ocular drug delivery.

(1) Corneal barrier, (2) blood-aqueous barrier, and (3) blood- retinal barrier. (Adapted from Bisht et al., 2018).

1.3 PLGA nanoparticles

NP-based drug delivery systems have the potential to improve bioavailability, enhance drug solubility and show excellent transportation of different drugs including genes, proteins, peptides, and vaccines. It has been reported that NPs show higher intracellular uptake than microparticles due to their reduced size and improved mobility (Desai et al., 1997). An *in vitro* study has shown that the cell uptake of 100 nm nanoparticles is 2.5-fold greater than that of 1 μm microparticles, and 6-fold greater than the uptake of 10 μm microparticles in a Caco-2-cell line (Desai et al., 1997). Other studies report that NPs with size of 10-150 nm are favorable for systemic drug delivery (Davis, 2008). Polymeric NPs are colloidal particles with a size which can be in the range of 10 -1000 nm. The cargo can be either homogenously distributed among the matrix or encapsulated inside the polymers. Examples of such polymers used for NPs include polylactic acid (PLA), poly-(lactide-co-glycolic acid) (PLGA), polyanhydrides, poly-ε-caprolactone (PCL) and poly-alkyl- cyanoacrylates (PACA) (Kumar et al., 2012). Among them, one of the most successfully developed polymers is PLGA, which has been approved by the Federal Drugs Administration (FDA) and European Medicine Agency (EMA), due to the good biodegradability and biocompatibility (Danhier et al, 2012).

The biodegradable nature of PLGA was first discovered by its application for surgical sutures in the 1960s (Jain, 2000; Hines and Kaplan, 2013). Since then, a wide range of PLGA derived materials has been designed and fabricated. To date, the PLGA NPs have been largely established for delivery of all kinds of compounds, including hormones, antibiotics, cytokines, and vaccines (Danhier et al, 2012). Preparation of PLGA NPs is usually based on emulsification-solvent diffusion technique (Quintanar-Guerrero et al., 1997). As shown in Figure 1.2, at first, the drugs and polymer are dissolved in organic solvent and then mixed with aqueous phase under high energy emulsification, and then, water is added to form the nanospheres when the solvent is evaporated, this leads to the colloidal suspension (Holmkvist et al., 2016). Under

physiological condition, PLGA will be finally hydrolyzed to two original monomers: lactic acid and glycolic acid (Figure 1.3). Lactic acid will enter into the tricarboxylic acid circle and then be metabolized, and glycolic acid will be metabolized in the same way and eliminated through the kidney (Hines and Kaplan, 2013).

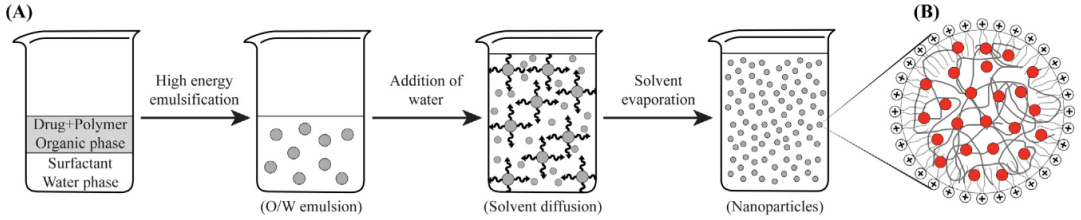

Figure 1.2 Production of PLGA NPs.

(A) The general process to prepare PLGA nanoparticles by the emulsification-solvent diffusion technique. (B) Proposed structure of the nanoparticles loaded with drug. (Adapted from Holmkvist et al., 2016).

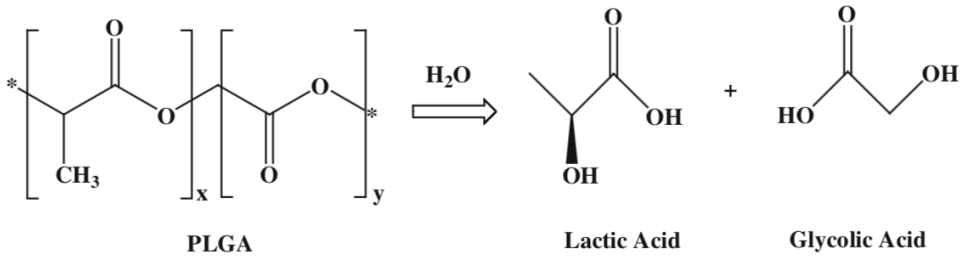

Figure 1.3 Chemical structure of PLGA and its biodegradation by hydrolysis in the body.

Adapted from Choi et al., 2012.

Given this advantage, PLGA has also been developed for ocular applications. Singh et al. demonstrated that by functionalization of PLGA NPs with arginine-glycine-aspartic acid (RGD) peptide and transferrin, PLGA NPs can be intravenously injected for targeted delivery of anti-vascular endothelial growth factor (VEGF) interceptor plasmid to inhibit choroidal neovascularization to prevent vision loss of age-related macular degeneration (AMD) (Singh et al., 2009). In addition, Luo et al. found that intravenously injectable PLGA NPs can deliver recombinant plasmid expressing Flt23k

to neovascular lesions of the retina and suppresses subretinal fibrosis, with 40% restoration from AMD was observed in murine models (Luo et al., 2013). However, these studies concentrate more on the effects of treatments and the kinetic and integrity of PLGA NPs in the blood circulation is only poorly explored.

1.4 Blood circulation

The blood circulation is the first biological environment that PLGA NPs will meet following intravenous (i.v.) administration. It can transport the vital nutrients, oxygen, ions and other molecules to the cells and meanwhile, take away the waste products from them. As a fluid, blood flow shares similarity with global fluid, however, as a biological network system, the blood components within it make the whole surrounding environment unsteady and complicated, making it difficult to predict of the dynamics of PLGA NPs. Therefore, traditional nano-bio interaction studies under static conditions such as incubation of NPs with blood serum can only have limited meaning.

1.4.1 The complex fluid patterns of the blood flow

The diameter of vascular system spans from capillary width of around 8 μm to artery width with approximate 4 mm, i.e., the size scale is not consistent throughout the body (Daly and Leahy, 2013). Furthermore, given other complex geometries such as non-linear curves, uneven cross section and existence of branches of blood vessels, the forces in the blood flow change correspondingly. The flow patterns can be predicted by Reynolds number (Re):

$$Re = \frac{\rho \bar{v} D_H}{\eta}$$

where $\bar{v}$ is the mean velocity, D_H the hydraulic diameter, and η the dynamic viscosity of the fluid. Generally, if Re < 2400, the viscous forces will be dominant and the laminar flow will be formed, which is characterized by parallel flow layers, reduced velocity toward the vessel wall, and the increased velocity toward the center of blood flow (Barral and Croibier, 2011). If Re > 4000, turbulent flow will start, as inertial

forces will be the leading one (LaNasa and Upp, 2014). Under normal physiological conditions, the main flow pattern in both capillary and artery is laminar, as the Re value for capillaries is 0.001 (Yoganathan et al., 1988; Ku, 1997; Fullstone et al., 2015) and those of artery, arteriole, venule and vein is 450, 0.5, 0.01 and 125, respectively (Daly and Leahy, 2013). However, for the flow in the heart, the Re number at the peak of systole can reach 4000 (Ku, 1997). Under pathological condition such as stenosis, turbulence patterns and reduced flow can appear (Ku, 1997). Meanwhile, there are different forces acting on the blood vessels (Figure 1.4) and blood flow patterns also change at the vascular intersections, curves, and branches. By combining the transgenic zebrafish embryo model and computational fluid dynamics method, Gomez-Garcia et al illustrated the shear stress and flow pattern in the zebrafish ventral vein, showing that the time-average wall shear stress is lowest at the branches of vessels and downstream of curvature area, where the flow disturbance is highest, and the accumulation of NPs is also high in these areas (Gomez-Garcia et al., 2018).

Additionally, Brownian motion is another force which needs to be considered. Liu et al. developed a multiscale method for NPs transportation in the cellular blood flow by coupling the lattice-Boltzmann method and Langevin dynamics and found that Brownian motion plays an important role for NPs distribution in 20 μm venules (Liu et al. 2018). The Brownian force at the blood vessel wall can increase due to the glycocalyx, a gel like layer at the cell wall, enhancing the contact time between substrates and the blood vessel wall (van den Berg et al., 1992; Fullstone et al., 2015). The complexity of blood environment is further increased, considering the cyclic nature of the heart pump which induces a pulsatile pressure and blood flow (Caro et al., 1978) Furthermore, the blood flow near the vessel wall is retarded due to the existence of shear stress generated by the endothelium cells, and the blood vessel wall is elastic (Daly and Leahy, 2013). This makes analysis of NPs' behavior within the blood circulation rather challenging.

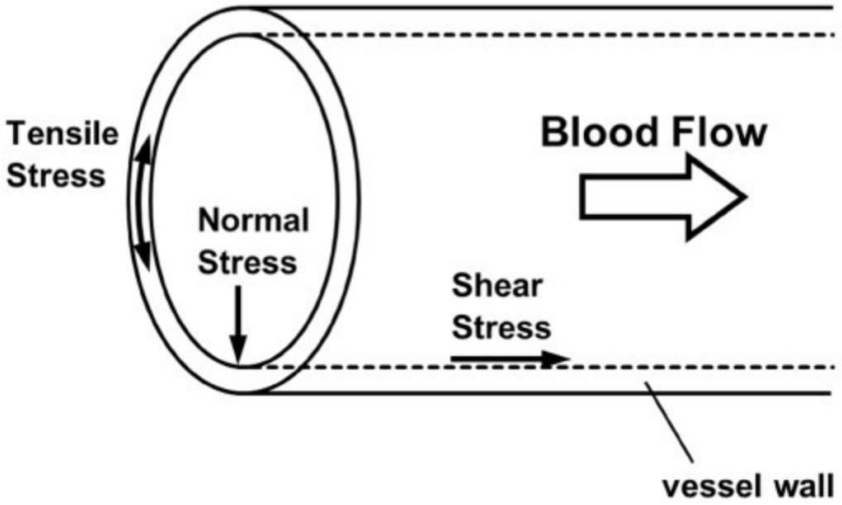

Figure 1.4 Forces on the blood vessels.

Shear stress, which is induced by the blood flow. Normal stress, which is caused by hydrostatic pressure. Tensile stress, which is generated from stretch of the vessel wall. (Adapted from Hsieh et al., 2014).

1.4.2 Blood components

NPs delivery cannot be simply evaluated by Newtonian flow. Blood, unlike the global fluid, is filled densely with cells including red blood cells (RBCs), white blood cells (WBCs) and platelets (Figure.1.5). About 54% of the volume are made up of plasma including different proteins, ions, hormones, etc., and 1% of the volume are composed of WBCs with ~10 μm in diameter and platelets with 2-3 μm in diameter (Ji et al., 2008; Thon and Italiano, 2012). RBCs, whose resting form is a biconcave disk with average 7.8 μm in diameter and deformable, constitute 45% of the blood volume (Strohm et al., 2013), offering non-Newtonian properties to the fluid. In capillaries, the diameter can be comparable to the size of the red blood cells (McWhirter et al., 2011).

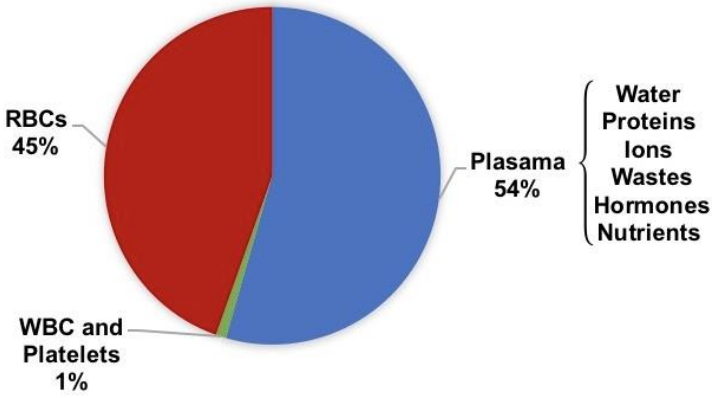

Figure 1.5 Blood components.

It includes red blood cells, white blood cells, platelets, and plasma. RBCs, red blood cells. WBC, white blood cells.

The presence of RBCs tumbling motion can enhance the NPs dispersion from the center of blood flow to the blood vessel wall. More NPs are found in regions near blood vessel walls with haematocrit of 38%, because it redistributes along the RBCs tumbling motion under the shear flow, and the improvement of dispersion rate of 100 nm NPs is more than that of 10 nm NPs (Tan et al., 2012). The study by Fullstone and colleagues demonstrated that the average dispersion factor in the capillary model increased at the intermediate haematocrit level, and this factor will be decreased since two separate phases (cellular phase and cell-free phase) can be formed at the higher haematocrit level due to the small space between the RBCs (Fullstone et al., 2015). This suggests that only the NPs in the region near the blood vessel wall can have a chance to bind to the blood vessel wall, when the diffusion factor is low. Therefore, the RBCs properties and their dynamic effects exert influence on the blood fluid property which will further influence the motion of NPs in the vicinity of a blood vessel wall and their binding time with endothelial cells and subsequent transportation across the wall.

Apart from the hydrodynamic forces, NPs in the blood circulation are also involved in multivalent interactions with bio-surfaces. In the blood plasma there are more than 3700 identified proteins (Cedervall et al., 2007). These proteins themselves such as LDL,

HDL (8-10 nm) are biological nanoparticles (Kontush et al., 2015). The interaction of NPs surface with proteins, either through specific or unspecific adsorption, can change the NPs residency in the blood, and the way by which cell components in the blood will interact with and process NPs. When proteins are adsorbed to some NPs, a protein corona will be formed which provides the NPs with a new identity (Lynch et al., 2009). According to a study on the plasma proteins adsorbed onto the copolymer NPs, the generation of protein coronas is not a static process, but a dynamic one: the proteins with high proportion in the plasma such as human serum albumin (HSA) and fibrinogen will occupy the surface of the NPs and then they will dissociate quickly from the NPs and are replaced by proteins with high affinity like apolipoproteins (Cedervall et al., 2007a). The protein adsorption could be dependent on the surface charge of NPs. Alexis et al. found that low level of plasma protein adsorption was observed on the neutral or negatively charged surfaces of NPs (Alexis et al., 2008). Another study from Gessner et al. using two-dimensional electrophoresis gel testified that the increased surface charge density will increase the protein adsorption (Gessner et al., 2002). In addition, the hydrophobicity of NPs surface also plays a role in the protein binding to the NPs, in that few proteins were retrieved from the less hydrophobic copolymer NPs, for example, more hydrophobic particles of 200 nm have surface coverage of 116 ± 37% whereas the surface coverage for more hydrophilic particles of 200 nm is 21 ± 15% (Cedervall et al., 2007b).

All of these properties make it difficult to obtain a blood flow model. Even though lots of models have been established and some studies used microfluidic based blood vessel mimicking devices, which has been successful in the study of NPs distribution, most of the studies only focused on one aspect of blood environment. For example, some studies emphasized the effect of plasma protein on the NPs by incubation of NPs in the blood sample without considering the fluid force effect on the NPs surface. Therefore, a good understanding of the blood circulation milieu is still missing.

1.5 Blood flow in the retina

The choroidal vessels and central retinal artery which originate from the ophthalmic arteries supply the blood for the eye. The central retinal arteries are the only blood supply arteries to the inner retina. They enter the eye through the optic foramen and divide into two distinct vascular plexuses: superficial vascular plexus in the ganglion cell layer of retina and the deep vascular plexus in the inner nuclear layer of the retina, where they further divide into capillaries with smaller diameters reaching to the peripheral retina by dichotomously branching or branching at right angles to the former vessels (Anand-Apte and Hollyfield, 2010) (Figure.1.6).

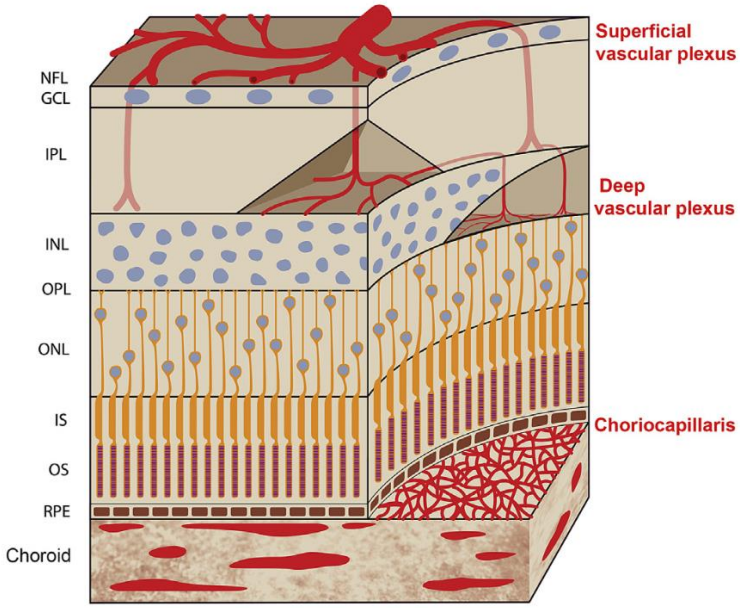

Figure 1.6 Blood vessels of the retina.

Two major blood vessels are shown here: choriocappillaris which support the retinal pigment epithelium and the photoreceptors, and the vascular plexuses in which the superficial ones supplying the nerve fibers and ganglion cells, and the deep ones supplying the inner nuclear layer and outer plexiform layers. NFL, nerve fiber layer; GCL, ganglion cell layer; IPL, inner plexiform layer; INL, inner nuclear layer; OPL, outer plexiform layer; ONL, outer nuclear layer; IS, inner segment layer; OS, outer segment layer; RPE, retinal pigment epithelium. (Adapted from Danesh-Meyer et al. 2015).

Studies on the normal human eye found that retinal blood flow rate is significantly correlated with the vessel diameter with a coefficient of r = 0.89 ($P < 0.001$) using the canon laser blood flowmeter (Garcia Jr. et al., 2002). In the pathological situations, the change in diameter of the retinal blood vessels can be observed. A study of the effect of increased inner ocular pressure (IOP) on the retinal perfusion showed that when the IOP was elevated (10 mmHg to 80 mmHg), both the density of capillaries and diameter of larger vessels declined and retinal blood flow was also reduced linearly (Zhi et al., 2012). The blood flow might be associated with the degree of eye disease damage. For example, advanced glaucomatous damage can lead to the decreased flow in lamina cribrosa and rim area, but no significant difference of the blood flow in the peripapillary retina was observed (Harju and Vesti, 2001). Grunwald et al. found that the mean optic nerve head relative blood flow from 5 measurement sites in glaucoma patients is decreased by around 24% compared to the control subjects (Grunwald et al., 1998). The abnormal optic nerve head autoregulation is commonly seen in the primary open angle glaucoma patients (Bata et al., 2019). In addition, the difference of local blood supply to the retina induced by acute high IOP might be associated with the selective loss of RGCs (Tong et al., 2010). However, it seems hard to say if the abnormal circulation of optic nerve head, retina and choroid is the cause or the result of glaucoma. But the abnormal blood flow and eye disease such as glaucoma are closely related. Therefore, the abnormal circulation in the retina further aggravates the difficulty to analyze the NPs as retinal drug delivery system under pathological condition.

1.6 Inner blood-retinal barrier

1.6.1 The cellular basis of the inner BRB transport: transcellular pathway and paracellular pathway

The BRB is composed of outer BRB which is located between the choriocapillaris and retina, and the inner BRB which regulates the transport of blood borne molecules from the luminal side to the abluminal side (Díaz-Coránguez et al., 2017). The retina capillary wall consists of the endothelial cells that are not fenestrated and linked with

tight junctions between them, basement membrane and intramural pericytes (Anand-Apte and Hollyfield, 2010). These endothelial cells together with Müller cells and astrocytes form the inner BRB which prevents large molecules such as proteins, cells and also ions from permeating out of the blood circulation (Anand-Apte and Hollyfield, 2010). However, CNS barriers do not block all the molecules' transport through the barrier. There are still some pathways that allow the specific molecules to cross the barrier. As shown in Figure 1.7, small lipophilic molecules can cross the inner BRB mainly by diffusion through the endothelial cells, other relatively large lipophilic and hydrophilic substances can be transported by an ATP-dependent process under the aid of receptor mediated transport, by pinocytic vesicles, carrier-mediated transporters, and ion transporters (Díaz-Coránguez et al., 2017). However, the expression of these transporters, vesicles and receptors are quite low at this unique inner BRB (Sagaties et al., 1987).

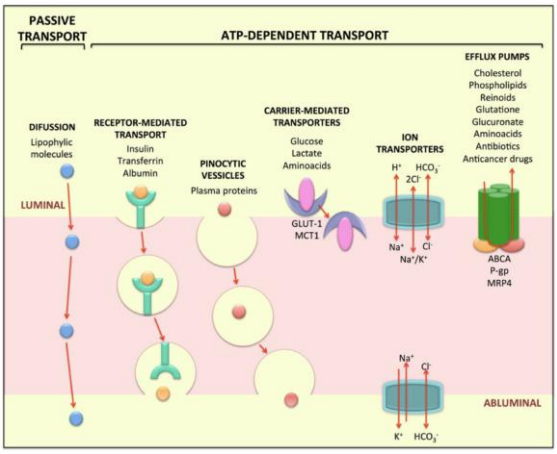

Figure 1.7 Transcellular transport across retinal endothelial cells.

Adapted from Díaz-Coránguez et al., 2017.

In addition to transcellular transport, paracellular transport is another possible way for substances to cross the BRB (Figure 1.8). Tight junctions, which are formed by fusion of adjacent endothelial cell membranes at several points, namely "kissing points", along the paracellular space, serve as gates and fences which restrict the molecules passing through the paracellular space and maintain the cell polarity by preventing the diffusion

of proteins or lipids between the apical and basolateral membrane (Reese and Karnovsky, 1967; Díaz-Coránguez et al., 2017). There are 40 proteins (transmembrane proteins, scaffolding proteins and effector proteins), including the three integral membrane proteins: claudin, occludin and junctional adhesion molecules (JAM) from immunoglobulin superfamily, which constitute the tight junctions and interact with cytoskeletal scaffolding proteins such as ZO proteins, which are members of the membrane associated guanylate-kinase protein family (Greene and Campbell, 2016). Therefore, modulation of tight junction to enhance BBB and BRB penetration through the paracellular pathway is a possible way to enable drugs to target cells in retina and brain.

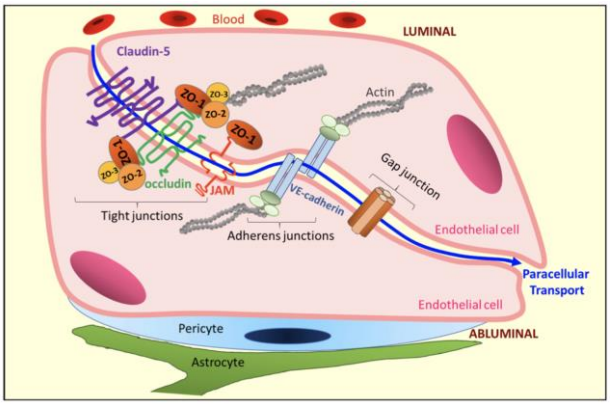

Figure 1.8 Paracellular transport across retinal endothelial cells.

In the BRB, molecules can move from the blood (luminal) into the retinal (abluminal) side via the paracellular space, which is located in between two adjacent cells (blue line). Some of the molecules central to control of paracellular transport of the BRB are indicated. (Adapted from Díaz-Coránguez et al., 2017).

1.6.2 Comparison of inner BRB and BBB

The blood brain barrier (BBB) and blood retina barrier (BRB) are barriers of the CNS (Engelhardt and Coisne, 2011). Although the inner BRB and BBB have a similar anatomy, there are studies suggesting that drugs show different abilities to permeate the BRB and BBB. For example, lipophilic substances exhibited high permeabilities across both of these two barriers, but their retinal uptake index is 4-fold higher compared to

the brain uptake index (Toda et al., 2011). By measuring the transfer of a vascular tracer, namely ^{14}C-α-amino-isobutyric acid (^{l4}C-AIB), Stewart and Tuor found that this compound was nearly 4 times higher in the retina than in the brain (Figure 1.9), possible reasons are that the density of endothelial vesicles and junctions in retina is higher than in brain vessels, and 4 times more pericytes are found in the retina compared to the brain which could explain the enhanced leakage (Stewart and Tuor, 1994). The study on the relationship of lipophilicity of compounds and their BRB permeability and comparing them with BBB permeability showed that they are correlated, and lipophilic compounds have higher permeability through paracellular transportation in BRB than in BBB (Hosoya et al., 2010). In addition, it was shown that higher concentration of P-glycoprotein has a higher impact on the permeation of some drugs like quinidine and verapamil in the BBB as compared to the BRB (Fujii et al., 2014).

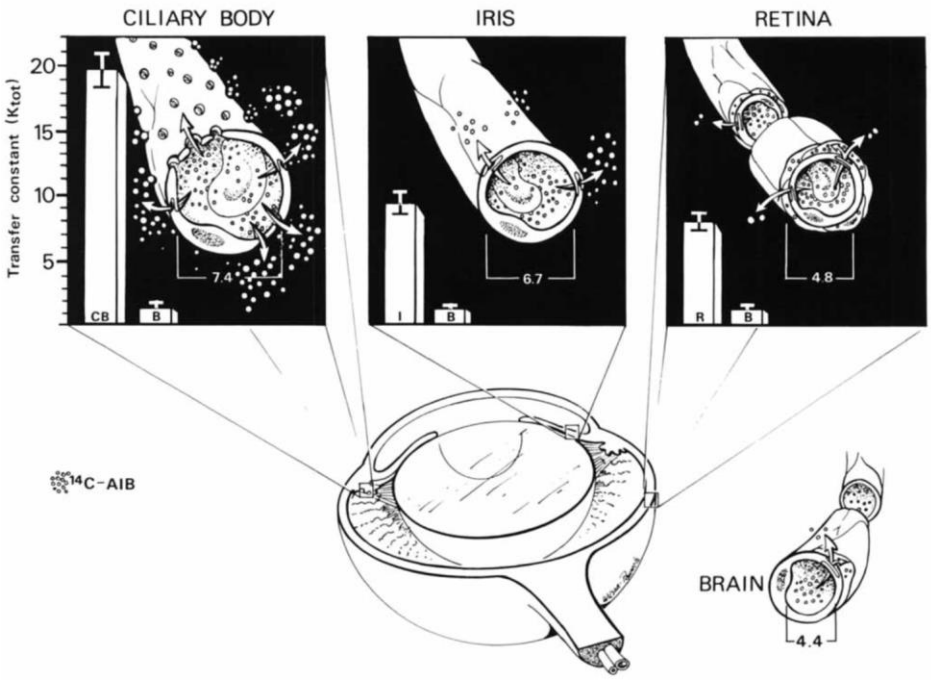

Figure 1.9 Comparison of transfer constant for ^{I4}C-AIB in ciliary body, iris, and retina with brain.

The possible permeability routes include paracellular routes, by which the molecules pass through the junctions, e.g., in ciliary body or iris, and transcellular routes, by which the

molecules pass through fenestrations, e.g., in ciliary body, and probably through endothelial vesicles. (Adapted from Stewart and Tuor, 1994).

1.7 Lipinski rules on barrier permeability of drugs

Regarding the strong barrier effect of BRB and BBB, searching for appropriate physicochemical properties of potential barrier permeable drug or released drug from the formulation is important. Over the decades, many physicochemical properties are widely studied (Li et al., 2005; Geldenhuys et al., 2015). The physicochemical property of a drug is one of the factors, important for the absorption, distribution, metabolism, and excretion (ADME) of drugs in the human body (Hurst et al., 2007). In 1997, Lipinski and his colleagues proposed that the drugs with good absorption and permeability are those with molecular mass less than 500 Daltons, less than 5 hydrogen bonds donors, no more than 10 hydrogen bond acceptors, and partition coefficient (log P) less than 5 (Lipinski et al., 1997). For example, by using this rule combining the DNA binding studies, one form of thiazoles was selected as a potential antibacterial molecule which showed good ADME profile and displayed inhibitory effect on the DNA gyrase (Santosh et al., 2018). The rules were further developed to identify the drugs with good central nervous system (CNS) and gastrointestinal absorption, in which the molecular weight was further lowered to 400 Daltons, the hydrogen bond acceptors declined to less than 7, and hydrogen bond donors were reduced to less than 3 (Fernandes et al., 2016). However, for the newly produced drugs lying outside the parameter cutoffs, it is believed that the Lipinski's rule is limited (Nagpal et al., 2013). Müller et al. selected one compound among the natural or semi-synthetic ecdysteroids by using the comprehensive physicochemical parameters, such as lipophilicity, topological polar surface area (TPSA), brain to plasma ratio (clog BB), and *in vitro* permeability (Müller et al., 2017).

1.8 Current study models of BBB and inner BRB

Various models are available to study the BBB and BRB. Franke et al. in 1999 developed primary cultivation techniques of porcine brain capillary endothelial cells,

which shows comparable BBB permeability of the selected drugs as *in vivo* experiment (Franke et al., 1999). Until today, monocultures of primary porcine brain capillary endothelial cells still remained as an efficient *in vitro* model for neuropharmaceutical research targeting BBB (Galla, 2018). Another type of model is using co-culture methods. Wisniewska-Kruk et al. demonstrated an *in vitro* BRB model using the co-culture of the bovine retinal endothelial cells, bovine retinal pericytes, and rat glial cells, showing that the high trans-endothelial resistance and reduced permeability of the tracers are typical features of BRB (Wisniewska-Kruk et al., 2012). Another human-based *in vitro* BRB model was reported using the co-culture of the retinal pericytes, retinal astrocytes, and retinal endothelial cells to study the level of junction proteins ZO-1 and VE-cadherin in diabetic retinopathy (Fresta et al., 2020). In addition, co-culture systems of human microvascular endothelial cells, retinal pericytes and Müller cells are developed to study the impact of thiamine and fenofibrate on the diabetic retinopathy (Mazzeo et al., 2020). Moreover, the transgenic zebrafish line is one of the examples that has been studied to establish an *in vivo* BBB and inner BRB model, which can express the fusion protein of vitamin D binding protein and enhanced green fluorescent protein in the blood plasma (Xie et al., 2010). However, although these models are beneficial for the molecular mechanism studies such as forward or reverse genetic screens, they are not sufficient for the kinetic study of NPs as drug delivery system in the blood circulation.

The *in vivo* confocal neuroimaging (ICON) technique was first reported in 1997 and used the eye as a “window of brain” to noninvasively visualize the retina in the living animals with high resolution. The technique was based on confocal laser-scanning microscopy with adjusted optics by an eye contact lens (Sabel et al 1997). Given these advantages, ICON was subsequently used to record, for example, the morphology changes of RGCs as a cellular response to optic nerve injury and calcium activation dynamic between surviving and dying RGCs (Figure 1.10) (Prilloff et al., 2010a). Therefore, it was considered an ideal method to observe the kinetics of NPs in the retinal blood circulation and passage of NPs through the blood retinal barrier.

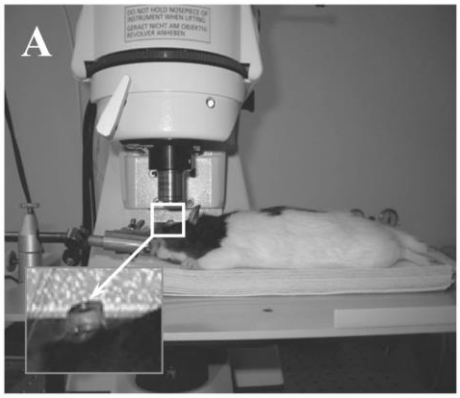

Figure 1.10 Example of ICON set up.

Anaesthetized rat placed under a scanning laser microscope. The inset image shows that a contact lens was placed on the eye. ICON, *in vivo* confocal neuroimaging. (Adapted from Prilloff et al., 2010a).

1.9 Objectives

My interest in the PLGA NPs delivery systems has prompted me to explore the dynamics of the distribution of PLGA NPs within the blood circulation and their potential to permeate the inner BRB. By using *in vivo* real time monitoring, *ex vivo* localization and classification method, I illustrate the influence of the *in vivo* biological environment on the interaction between the model drugs as cargoes and PLGA NPs as carriers and the role of physicochemical properties of drug candidates on the interactions between model drugs and inner BRB. Furthermore, I used the optic nerve crush model to evaluate if the kinetics of PLGA NPs delivery system will change under the optic nerve injured condition and if this pathological condition induces any changes on the delivery of NPs to the retina. While my work covered the biological approaches to understand the relationship between the basic properties of model drugs and their BRB permeability, classification of studied model drugs with Lipinski rules, and size study of the NPs incubated in serum or PBS by dynamic light scattering, the NPs used for my study were provided by our cooperation partners from the group of Dr. Svetlana Gelperina (D. Mendeleev University of Chemical Technology of Russia, Moscow, Russia).

The specific objectives of this thesis are the following:

Study I: Can model drugs be released from PLGA NPs during the blood circulation in the retinal blood vessels? How are the kinetics of PLGA drug delivery systems under real-life conditions and real-time at biological barriers? Is there any difference between the kinetics of lipophilic model drug as cargo and hydrophilic model drug as cargo? Is a mutual interaction of model drugs and PLGA NPs influencing the kinetic?

Study II: How is the distribution of PLGA NP systems when encapsulating poorly water-soluble model drug? Is the poorly water-soluble model drug released from PLGA NPs during the blood circulation in the retinal blood vessels of healthy and optic nerved injured retina? Do pathological changes in the retina influence the kinetics of PLGA nano-carriers as compared to the normal retina?

Study III: Do molecular structure descriptors from Lipinski rules correlate with the permeability of poorly water-soluble model drugs in the Study I and Study II to inner BRB and BBB? How efficient and what is accuracy to predict the BBB or BRB permeability by combining the machine learning method and Lipinski rules?

Understanding the nano-bio interactions in the blood circulation in normal or pathological condition will provide the possibility to help design safe and applicable NPs for diverse eye or CNS disease in the field of nanomedicine.

2. Study I: Release kinetics of fluorescent dyes as model drugs from PLGA nanoparticles in retinal blood vessels[1]

2.1 Introduction to Study I

Nanoparticles may be of value to serve as drug delivery systems and as imaging or diagnostic agents (Duncan, 2005). However, despite much effort, only few nanoparticle systems could be translated to clinical applications (Lü et al., 2009). Polyesters, including polylactic acid (PLA) and poly (lactic-co-glycolic acid) (PLGA), which are FDA and EMA approved polymers (Makadia and Siegel， 2011; Cheredd et al., 2016), are generally well tolerated by biological systems and such nanoparticles (NPs) are therefore the most broadly studied class of biodegradable drug delivery systems. PLA or PLGA NPs have several advantages: (i) they protect drugs from degradation; (ii) show good bioavailability of therapeutic compounds (Thomas et al., 2014.) and help to achieve sustained release (Makadia and Siegel, 2011); (iii) well described methods are available for their preparation with various types of drugs (Lü et al., 2009); (iv) they have favorable physicochemical and surface properties in the nanometer range, facilitating cellular uptake of the drug to specific tissues and cells (He et al., 2010); and (v) they have good safety profile (Semete et al., 2010). Moreover, due to their small size, PLGA NPs can penetrate specific tissues via fenestrations present in the endothelium of cancerous and inflamed tissue or via receptors overexpressed by target cells (Malam et al., 2009). As a consequence, these NPs are effective for the sustained delivery of lipophilic and hydrophilic drugs and can be administrated by multiple ways

1. This work was published: Zhang, E., Zhukova, V., Semyonkin, A., Osipova, N., Malinovskaya, Y., Maksimenko, O., Chernikov, V., Sokolov, M., Grigartzik, L., Sabel, B.A., Gelperina, S., Henrich-Noack, P., (2020). Release kinetics of fluorescent dyes from PLGA nanoparticles in retinal blood vessels: *In vivo* monitoring and *ex vivo* localization. Eur. J. Pharm. Biopharm. 150, 131–142. DOI: 10.1016/j.ejpb.2020.03.006

such as peroral, subcutaneous injection or intravenous injection (i.v.) (Barichello et al., 1999; Danhier et al., 2012).

Despite this pronounced potential of PLGA NPs as delivery system, little attention was payed to their real-time kinetic profile or correlation between PLGA carriers and cargoes in the blood circulation of the retina. Generally, protocols for *in vivo* pharmacokinetics studies include collecting the blood samples at different time points, separating the plasma, and then detecting the nanoparticles of interest in the blood (Win and Feng, 2006; Kalaria et al., 2009; Booysen et al., 2013). No doubt that by the analyses using wide array of precise instruments, such as spectrophotometers, high performance liquid chromatography, capillary zone electrophoresis systems etc., scientists can quantify the concentration of NPs in the blood precisely and efficiently. However, these methods are limited, when the integrity of particle loaded with cargoes and interaction between them has to be considered under the complex retinal blood circulation *in vivo*. Furthermore, most of the existing *in vivo* studies on the treatment of different diseases with NPs are restricted to one single substance as a model drug, loaded in NPs and focusing on its distribution in tissue section or homogenate postmortem (Semete et al., 2010; Song et al., 2011; Rafiei and Haddadi, 2017). Other reports concentrate on the design of novel carrier system *in vitro* (Fonseca et al., 2002; Budhian et al., 2008). However, when it comes to clinical translation, especially through the most often used intravenous injection, the complex *in vivo* environment of the retinal blood circulation was not studied, though it is expected to influence the integrity of NPs and the release of the loaded drug. Such factors included the serum composition, blood pressure, and high blood flow velocity, shear forces and other parameters.

To overcome these limitations, the aim of the present study was to evaluate the kinetics of PLGA NPs in the retinal blood circulation *in vivo* using eye as a convenient imaging model. To this end, NPs were loaded with fluorescent dyes, either lipophilic DiI (1,1'-dioctadecyl-3,3,3',3'-tetramethylindocarbocyanine perchlorate) or water-soluble

Rho123 (Rhodamine 123). These two dyes were widely encapsulated into the NPs, as model fluorescent probes. Whereas Rho123 is a substrate of the P-glycoprotein (P-gp) (Castro et al., 1989; Masereeuw et al., 1997; Liang et al., 2005), DiI is a cell membrane stain which has strong fluorescence and slow fading feature (Schlessinger et al., 1977; Li et al., 2008; Chang et al., 2009). These NPs were then injected intravenously *in vivo* and the biodistribution and kinetics of these cargoes were studied in the retina by visualizing fluorescent signal in the retinal blood vessels with *in vivo* Confocal Neuroimaging (ICON) system (Sabel et al., 1997; Prilloff et al., 2010). Subsequently, preparations of whole mounted retinae were analyzed for the distribution of NPs at higher resolution.

In addition, as the cargo release kinetics need to be taken into account, detecting the location of the fluorescence signal from cargoes alone may not fully reveal the location of the NPs. Therefore, to evaluate the integrity of NPs in the retina, Cyanine5.5 amine (Cy5.5) was chemically linked to the carrier-polymer PLGA and then I analyzed colocalization of the Cy5.5 and cargo signals.

This study demonstrated for the first time, that the integrity of carrier-cargo systems in the blood circulation *in vivo* in the retina changes according to the encapsulated cargoes (drug or diagnostic markers). In this way, it is necessary to develop and individually examine carefully designed PLGA delivery systems with respect to target and route of administration.

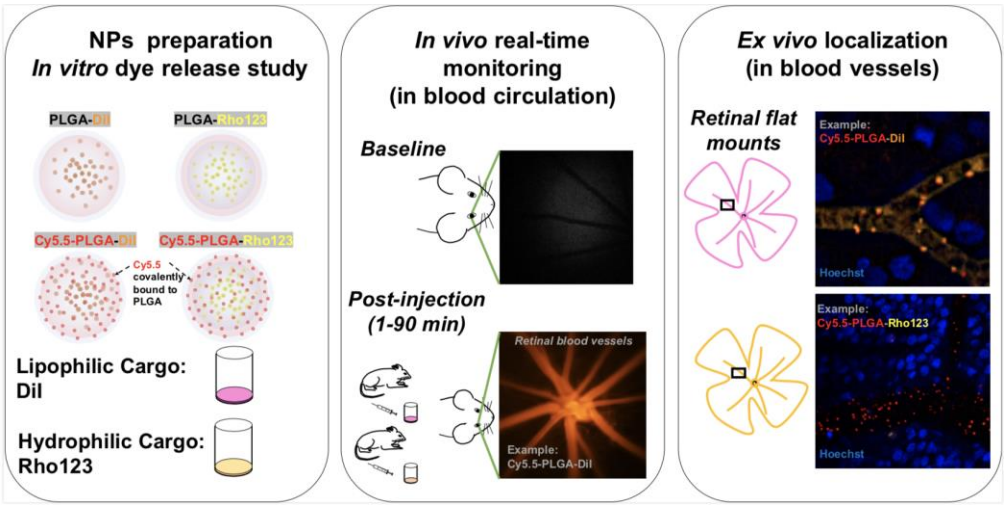

Figure 2.1 Scheme of Study I

2.2 Material and methods of Study I

2.2.1 Chemicals

Cy5.5®, analogue amino-derivative for conjugation	Lumiprobe Life Science solutions, USA
Poly(lactic-co-glycolic acid) (PLGA, Resomer® RG 502H)	Evonik Röhm GmbH, Germany
Kolliphor P188®, poloxamer 188	BASF, Germany
F-12K medium	Life Technologies Europe BV, Netherlands
Fetal bovine serum	ATCC, USA
Horse serum	ATCC, USA
Newborn calf serum	ATCC, USA
Penicillin/streptomycin	Biochrom AG, Berlin, Germany
Ketamine (100 mg/ml)	Arzneimittelvertrieb GmbH, Ascheberg, Germany
Medetomidine hydrochloride (1 mg/ml)	Vetoquinol GmbH, Ravensburg, Germany
Neosynephrine-POS 5%	Ursapharm GmbH, Saarbrücken, Germany
Vidisic® optical gel	Bausch & Lomb, Berlin, Germany

Saline (0.9%)	Fresenius Kabi Deutschland GmbH, Bad Homburg, Germany
Hoechst 33342	Cayman Chemicals, Hamburg, Germany
1'-dioctadecyl-3,3,3',3'-tetramethylindocarbocyanine perchlorate (DiI) and other chemicals	Sigma-Aldrich

2.2.2 Fluorescence dye loaded PLGA NPs

The particles were provided by group of Dr. Svetlana Gelperina (D. Mendeleev University of Chemical Technology of Russia, Moscow, Russia). See publication (Zhang et al., 2020). Briefly, DiI-loaded PLGA NPs (PLGA-DiI) and Rhodamine123-loaded PLGA NPs (PLGA-Rho123) were produced by a high pressure o/w and w/o/w emulsion solvent evaporation technique, respectively. Free DiI was removed from the nanosuspension by centrifugation, and free Rho123 was removed from the nanosuspension by gel filtration chromatography using a Sephadex G-25 column. Then the NPs were freeze-dried. Cy5.5-PLGA NPs were prepared by covalently binding Cyanine5.5 amine to a carboxylic terminal group of PLGA (Resomer® RG 502H) via a carbodiimide coupling reaction (Malinovskaya et al., 2017). Then, Cy5.5-PLGA NPs labeled either with DiI (Cy5.5-PLGA-DiI NPs) or with Rho123 (Cy5.5-PLGA-Rho123 NPs) were prepared again by either o/w (DiI) or w/o/w (Rho123) emulsification technique.

Table 2.1 Physicochemical characteristics of PLGA NPs.

Sample	Content of dye, µg/ mg PLGA	Encapsulation efficiency, %	Average diameter, nm	PDI	ζ-potential, mV
PLGA-DiI	11.8	83	130 ± 2	0.156 ± 0.009	-23.8 ± 9.1
PLGA-Rho123	5.0	96.4	132 ± 1	0.148 ± 0.022	-29.7 ± 0.4
Cy5.5-PLGA-DiI	DiI: 6.2 Cy5.5: 1.37	100	137± 1	0.136 ± 0.022	-18.0 ± 0.7
Cy5.5-PLGA-Rho123	Rho123: 8.7 Cy5.5: 0.45	94.9	133 ± 2	0.175 ± 0.024	-23.0 ± 4.3

PLGA NPs were prepared using PLGA (50/50, Resomer® 502H) and 1% PVA (9-10 kDa) solution as an external medium for o/w emulsion. (n=3, mean ± SD)

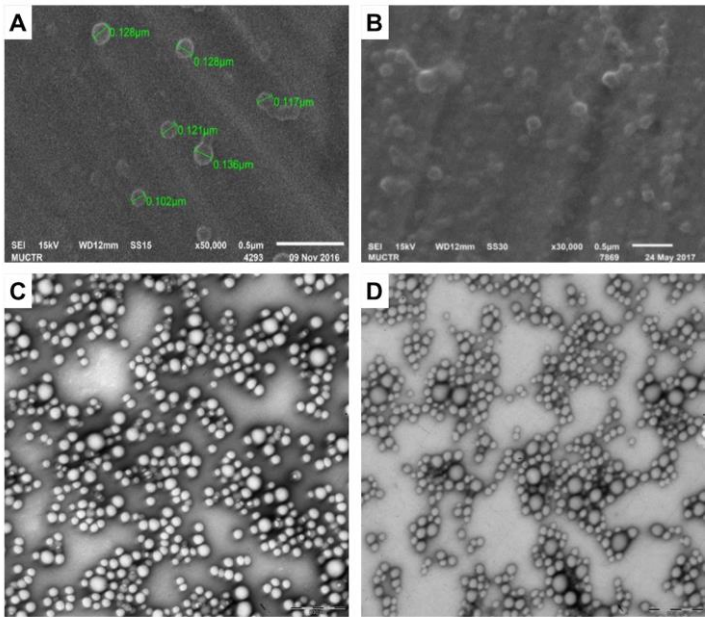

Figure 2.2 Morphology of NPs under electron microscopy.

SEM image of PLGA-DiI NPs (A) and PLGA NPs covalently linked with Cy5.5 (Cy5.5-PLGA /PLGA = 1:1, w/w) (B). TEM image of PLGA-DiI NPs (C) and PLGA-Rho123 NPs (D). Scale bar 0.5 μm.

Dye release studies in vitro (were assisted by the group of Dr. Svetlana Gelperina, D. Mendeleev University of Chemical Technology of Russia, Moscow, Russia)

The release of the dyes from PLGA NPs was evaluated in 1% (m/v %) solution of the poloxamer 188 in 0.15 M PBS at pH 7.4. The NPs were resuspended in release medium, and the resulting suspension was diluted 25-fold with 1% poloxamer 188 solution and then incubated at 37ºC under continuous shaking (orbital shaker-incubator ES-20, Biosan, Latvia). At regular intervals (24 h, 48 h and 7 d), the 1.5 ml aliquots of the suspension were sampled and centrifuged at 48380 g, 18ºC for 30 min (Avanti JXN-30, Beckman, USA). The amount of the released dye in NPs was determined spectrophotometrically in supernatants in the presence of 50% ethanol. For Rho123 PLGA NPs, their stability was also estimated in 0.15 M PBS medium (pH 7.4) following a similar procedure. The experiments were performed in triplicates.

2.2.3 Estimation of stability of PLGA NPs in serum

Stability of the NPs in serum was evaluated based on their size distribution after incubation in phosphate buffered saline (PBS, pH 7.4) containing 0%, 10%, or 50% of fetal bovine serum (FBS). The PLGA-DiI NPs or PLGA-Rho123 NPs coated with 1% poloxamer 188 were dispersed in the FBS to the concentration of 5 mg/ml; the suspensions were incubated for predetermined periods (10, 30, 60, 90 min) and analyzed by a dynamic light scattering method.

2.2.4 Cell viability test

To analyze the effect of the NPs coated with poloxamer (P188) (PLGA-DiI/P188 NPs and PLGA-Rho123/P188 NPs) on the viability of HEK-293 cells, the MTT assay was used. Cells were propagated in DMEM medium supplemented with 10% newborn calf serum and 1% penicillin. HEK-293 cells were seeded in 96-well plates, 1×10^4 cells/well in 100 μl medium. After attachment of cells, 200 μl of the fresh medium with either PLGA-DiI/P188 NPs or PLGA-Rho123/P188 NPs was added. The final concentrations of NPs were 0, 0.1, 0.2, 0.4, 0.8, 1.6 mg/ml. After incubation for 24 h, cells were gently washed with PBS for three times to remove the residue of NPs. Then 10 μl of 5 mg/ml MTT assay solution was added to each well. The culture medium was discarded and 100 μl dimethyl sulfoxide (DMSO) was added to solubilize the intracellular formazan crystals for 4 h of incubation at 37°C in 5% CO_2. The Formazan produced by mitochondrial reduction of thiazolyl blue tetrazolium bromide was quantified by measuring the absorbance at 490 nm. The plate was shaken for 10 minutes (5-6 rpm) before measurement, and absorbance was detected by a microplate reader (Dynex Technology, Germany). The percentage of surviving cells was estimated by dividing the absorbance values of the cells by average values from the control cells (medium without NPs) (6 replicates for each group).

2.2.5 Animals

All procedures were performed under ethical approval according to the requirement of the German National Act on the use of experimental animals (Ethic committee Referat Verbraucherschutz, Veterinärangelegenheiten; Landesverwaltungsamt Sachsen-Anhalt, Halle).

Adult male Lister hooded rats (Crl: LIS strain; Charles River) with an average body weight of 315 ± 23 g were housed on a 12 h light/12 h dark cycle under standard environment conditions at ambient temperature of 22°C at 50-60% humidity. Animals had access to food and water ad libitum, except on the day before induction of narcosis, where food was removed. Animals were kept at least 1 week for adaption in group cages and were handled before starting the experiment to reduce the stress.

2.2.6 *In vivo* confocal neuroimaging

Freshly prepared suspensions of different NPs loaded with fluorescent dyes were administrated intravenously. For PLGA NPs group coated with poloxamer 188 (P188), NPs were dispersed in 0.5 ml of a sterile 1% poloxamer 188 solution in deionized distilled water (dd water); for non-coated PLGA NPs group, PLGA NPs were resuspended in 0.5 ml sterilized dd water. For free dye groups, 1 mg/ml stock solutions of DiI (in ethanol) and Rho123 (in sterilized dd water) were prepared and then diluted with saline for injection, by reference to previous reports (Aston and Cullumbine, 1959; Peng et al.,1970; Doerge et al., 2010). Dosage of all PLGA NPs samples was adjusted to DiI concentration of 0.2 mg/ml and Rho123 concentration of 0.16 mg/ml. Double stained Cy5.5-PLGA NPs were resuspended in 0.5 ml 1% poloxamer 188 and injected according to the DiI/ Rho123 concentration. All samples were vortexed gently and left for 30 min at ambient temperature before use. The animals were anesthetized with an intraperitoneal injection of Ketamine (75 mg/kg) and Medetomidine (0.5 mg/kg). The eyes of anaesthetized rats were treated with Neosynephrine-POS 5% to relax the iris, and Vidisic® eye gel was applied to protect the eye from drying out and used as

immersion medium for the contact lens as well. Then, the rats were fixed under a confocal scanning microscope with the eye positioned in working distance underneath the objective lens and a cannula was inserted into the tail vein. After the 0.5 ml intravenous injection, the fluorescence of the NPs was observed in the retina, and the images were captured at different time points 0 (baseline), 1, 3, 5, 15, 30, 60, 90 min. The rats were kept on the heating plate during all the *in vivo* imaging process. All the images were obtained from the same resolutions (×5 magnification and same image size).

2.2.7 Visualization of PLGA NPs in the blood vessels of flat mount retina

After *in vivo* real-time imaging, rats were euthanized with an overdose of aforementioned anesthetic and the eyeballs were enucleated and placed into cooled HEPES buffered solution (135 mM NaCl, 5 mM NaOH, 2.5 mM KCl, 7 mM $MgCl_2$, 10 mM HEPES, 10 mM glucose; pH 7.4). The anterior segment of eye and vitreous body were removed. The whole retina was then carefully separated from the sclera, flatted on the modified culture plate, and the whole mounts were then incubated with 0.1 mg/ml Hoechst 33342 (Hoechst) in HEPES solution for 20 minutes for nuclei staining. Flat mount retina was fixed with 4% paraformaldehyde solution for 20 minutes and washed afterwards with HEPES solution. The images were captured immediately after preparation of retinal flat mount with a Zeiss microscope (Jena, Germany).

2.2.8 Statistical analysis

The quantification analysis of fluorescence signal in the retina and threshold overlap score at the highest intensity (TOSh), Pearson correlation coefficient (PCC), Spearman's rank correlation coefficient (SRCC), were performed and evaluated by means of MATLAB (MathWorks, Inc., Natick, MA, USA), Image J (US National institutes of Health, Bethesda, USA) software and EzColocalization ImageJ plugin (Stauffer et al., 2018). Data were fitted with double exponential function.

2.3 Results of Study I

2.3.1 Nanoparticle characterization *in vitro*

2.3.1.1 Physicochemical properties of NPs

Fluorescent PLGA NPs were prepared using an emulsification-solvent evaporation method and then washed from the free dye either by centrifugation (DiI) or gel permeation chromatography (Rho123). An additional Cy5.5 label was introduced by covalently binding to the polymer in order to distinguish the distribution of the carrier per se and the fluorescent cargo. The physicochemical parameters of the fluorescently labeled PLGA NPs, i.e. PLGA-DiI, PLGA-Rho123, and double-stained Cy5.5-PLGA-DiI, Cy5.5-PLGA-Rho123 NPs are shown in Table 2.1. All NPs exhibited similar average sizes of ~130 nm and a relatively narrow size distribution (PDI < 0.2). The encapsulation efficiency was in the range of 83-100% in the case of DiI and up to 96.4% in the case of Rhodamine 123. Covalent attachment of Cy5.5 to the polymer did not significantly alter the sizes of NPs. The zeta potentials of all nanoparticles were negative. As shown in the SEM and TEM images, the NPs had spherical shapes and smooth surfaces (Figure 2.2A-D).

2.3.1.2 Dye release studies in vitro

The kinetics of the dye release from the NPs was evaluated under the simulated physiological conditions (PBS, pH 7.4, 37°C) with addition of 1% poloxamer 188 as a solubilizing agent for poorly soluble fluorescent dyes. As shown in Table 2.2, both PLGA-DiI and Cy5.5-PLGA-DiI NPs exhibited minimal release of DiI (8.5 %) up to 24 h. In contrast, Rho123 quickly diffused into the medium during the first 24 h (54%), but thereafter only slow additional release was observed (approximately 10 % during the next 7 days). No release of conjugated Cy5.5 was observed during the period of up to 7 days, which was also confirmed by thin layer chromatography TLC (data not shown) indicating the stable covalent bond.

Table 2.2 *In vitro* release of fluorescent dyes DiI and Rho123 from PLGA NPs.

Type of NPs	Amount of released dye, %		
	24 h	48 h	7 days
PLGA-DiI	8.2 ± 0.4	11.95 ± 0.4	17.3 ± 1.4
Cy5.5-PLGA-DiI	8.5 ± 3.0	11.9 ± 0.9	13.2 ± 0.3
PLGA-Rho123	54.0 ± 1.1	58.8 ± 0.9	65.5 ± 0.8
Cy5.5-PLGA-Rho123	50.5 ± 2.6	55.0 ± 1.8	NA

In vitro release of fluorescent dyes DiI and Rho123 from PLGA NPs in a solution of 1% poloxamer 188 in 0.15 M PBS (pH 7.4, 37°C, n = 3, mean ± SD).

2.3.1.3 In vitro interaction of PLGA NPs with FBS and cell viability assay

The sizes of the PLGA NPs coated with poloxamer 188 upon incubation with PBS, 10% FBS, and 50% FBS were also evaluated (Figure 2.3A). The size distribution profiles of the PLGA-DiI/P188 NPs incubated in 10% or 50% serum were similar. Similarly, the peak of the PLGA-Rho123/P188 NPs size distribution showed no obvious changes in 10% serum and 50% serum after 90 min incubation. No time dependent flocculation could be detected over a time period of at least 90 minutes, indicating a sufficient stability for further NPs *in vitro* evaluation.

To evaluate the toxicity of PLGA-DiI/P188 NPs and PLGA-Rho123/P188 NPs, MTT test was performed after 24 hours incubation of HEK-293 cells with the particles. Although the cell viability gradually declined as the concentration of NPs increased from 0.1 to 1.6 mg/ml, cells tolerated both NPs well. As shown in Figure 2.3B even with increasing NP concentrations up to 1.6 mg/ml, the cell viability decreased only to ~70% for PLGA-DiI/P188 and ~68% for PLGA-Rho123/P188.

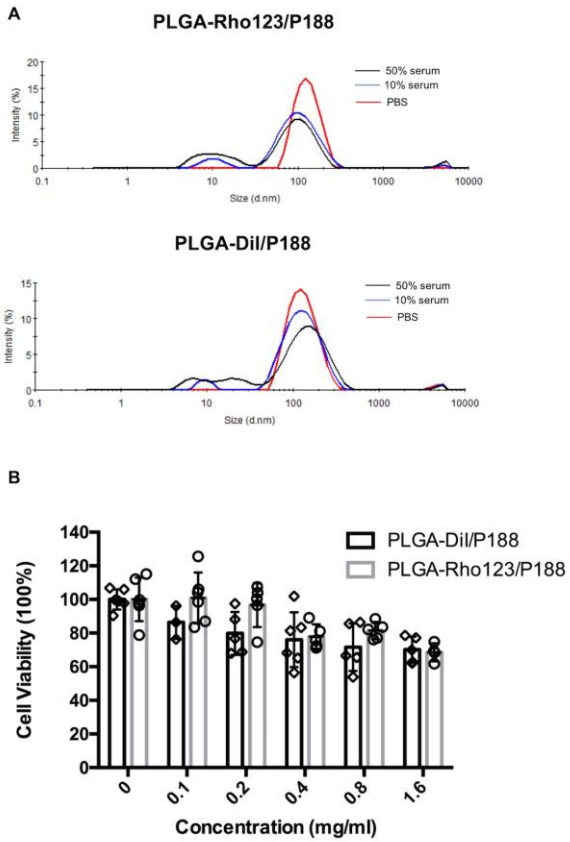

Figure 2.3 *In vitro* interaction of PLGA NPs with FBS and cell viability assay.

A, Examples of particle size distribution of PLGA-Rho123/P188 NPs (upper panel) in PBS and PLGA-DiI/P188 NPs (lower panel) in PBS and FBS (10% and 50%) after 90 min of incubation (n=3). B, Cell viability of HEK-293 cells after incubation with PLGA-DiI/P188 NPs or PLGA-Rho123/P188 NPs for 24 h (n=6, error bars represent mean ± SEM).

2.3.2 Comparison of kinetics and location between lipophilic and hydrophilic cargoes from PLGA NPs in blood vessels

2.3.2.1 In vivo real-time study of cargoes DiI or Rho123 loaded in PLGA NPs in retinal blood vessels by ICON

To trace the distribution of cargoes (DiI/Rho123) loaded in the NPs within the relevant timespan (0-90 min) in the retinal blood vessels, *in vivo* real-time imaging was used to analyze the fate of these cargoes in the retina (Figure 2.4). After the i.v. injection of PLGA-DiI NPs, the fluorescence signal from both poloxamer 188-coated and non-coated particles, reached the maximum within first minute (Figure 2.4A-B). Strong

decrease of the fluorescence signal (DiI) in the retinal blood vessels was observed throughout first 30 min, presumably reflecting clearance of NPs from the blood circulation in the retina. The residual staining which remained relatively stable up to 90 min (Figure 2.4D) could be explained by either that NPs persisted in the blood or stained the blood vessel wall (or both) (Figure 2.4A-B).

Additional experiment indicated that this DiI signal from PLGA-DiI/P188 NPs sustained in the blood vessels for more than 2.5 hours. However, injection of free dye showed different kinetics (Figure 2.4C), with fluorescence increasing strongly within first few minutes, reaching the maximum at 30 min and starting slow decay after 1 h (Figure 2.4C-D). Unsurprisingly, in the presence of poloxamer 188, the PLGA-DiI NPs were more homogeneously distributed than the uncoated NPs, because more coalescence (spots) of the NPs in the blood vessels were visible, when uncoated NPs were injected, as shown in Figure 2.4B. When imaging the Rho123-loaded NPs, the fluorescence signal (Rho123) also reached the maximum within 1 min after injection (Figure 2.4E-F), however, unlike the DiI-loaded NPs, this signal (Rho123) dramatically decreased within 5 min, and virtually disappeared after 15 minutes. Free Rhodamine 123 was found to be eliminated already after 5 min (Figure 2.4G).

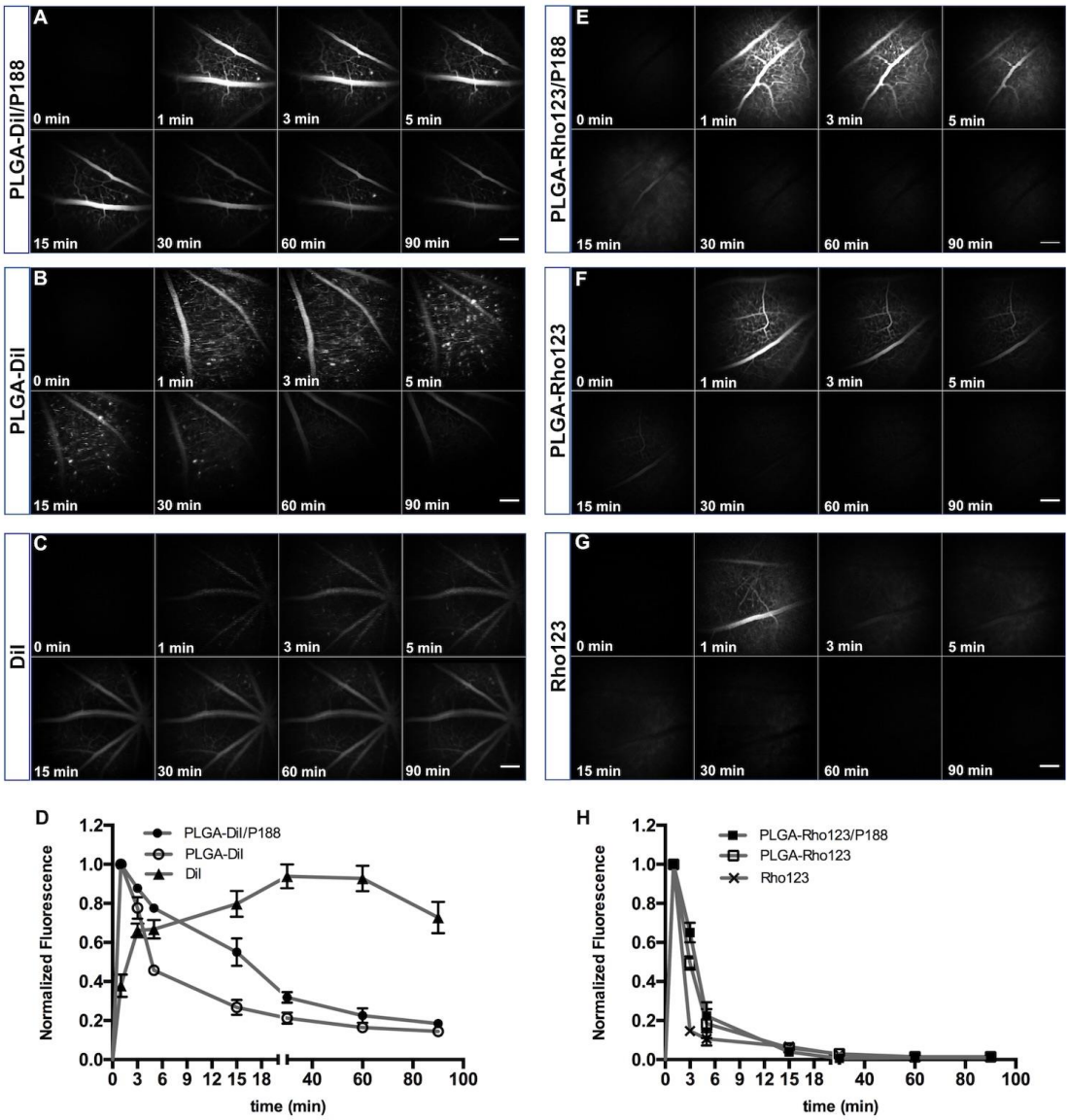

Figure 2.4 *In vivo* real-time signal monitoring and quantification of fluorescence signal in the retinal blood vessels after intravenous injection of PLGA NPs or free fluorescent dye.

PLGA-DiI NPs coated with poloxamer 188 (A), uncoated PLGA-DiI NPs (B), and free DiI (C) and the corresponding normalized DiI fluorescence intensity in D. PLGA-Rho123 NPs coated with poloxamer 188 (E), uncoated PLGA-Rho123 NPs (F), and free Rho123 (G) and the corresponding normalized DiI fluorescence intensity in H. Images were captured before i.v. injection (0 min) and at defined intervals, as indicated, until 90 min post injection by ICON technique. Scale bar in all images 200 μm. The signal value at

given point was normalized to the maximum fluorescence in respective group. n=3-5/group, error bars represent mean ± SEM.

2.3.2.2 Final location of cargoes from PLGA NPs in retinal flat mounts

A clearly different distribution regarding the PLGA-DiI/P188 NPs and the PLGA-Rho123/P188 NPs was observed in the retinal flat mounts (Figure 2.5). The PLGA-DiI/P188 NPs (spots) were located mainly in the lumen of the blood vessels in which DiI signal was also found on the blood vessel wall. It can be assumed that DiI diffused out of NPs and stained the blood vessel walls. Other researchers have already demonstrated that an aqueous DiI solution formulated to avoid precipitation of this dye can penetrate into endothelial cell membranes upon contact and then directly label blood vessels after cardiac perfusion within 1 h (Li et al., 2008). In this study, DiI incorporated into the PLGA NPs with narrow distribution (PDI 0.156 ± 0.009, Table 2.1) also illustrates the ability of DiI to label blood vessels in the retinal flat mount (Figure 2.5A-E). In agreement with *in vivo* data shown in Figure 2.4, at 2 h post injection of PLGA-Rho123/P188 NPs (Figure 2.5F and 2.5G), no Rho 123 fluorescence signal was detected. This observation suggests that it has been eliminated from the blood circulation in the retina.

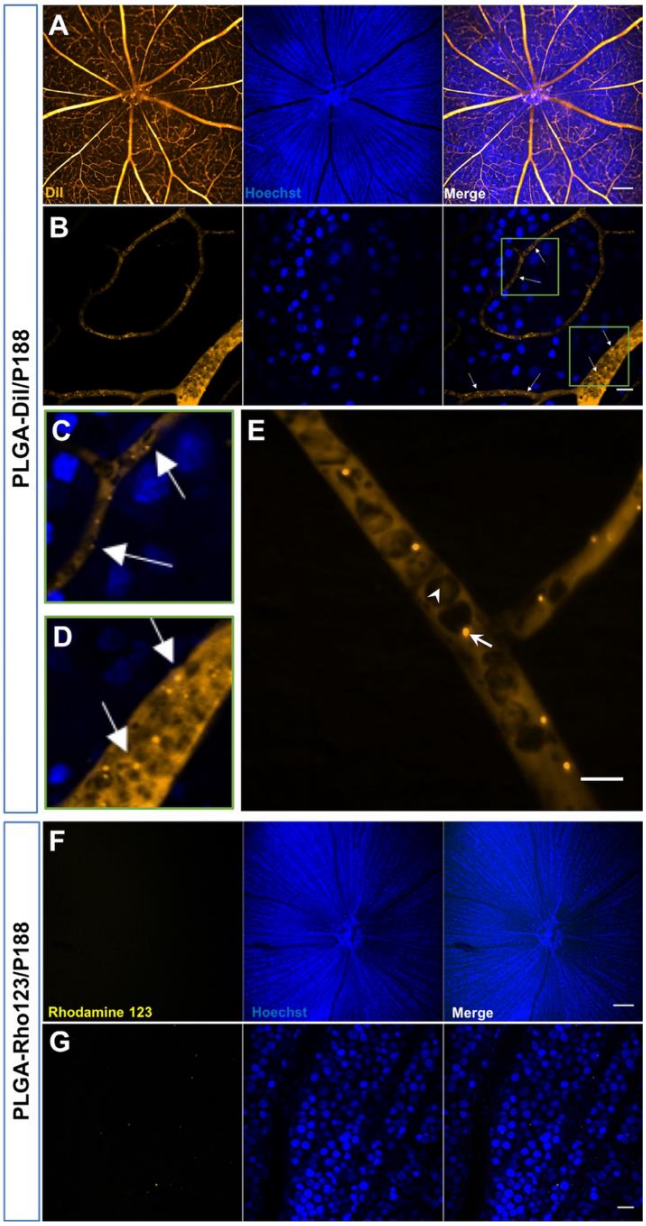

Figure 2.5 Retinal flat mounts after *in vivo* real-time imaging analysis at 2 h time point post injection.

After injection of PLGA-DiI/P188 NPs, DiI fluorescence (orange) is seen in the branches of blood vessels (A-E). C and D: green square area from B. In E, arrowhead: blood cell, arrow: NPs accumulations. Rho123 signal (yellow) was not detected in the flat mount prepared at the 2 h time point after PLGA-Rho123/P188 NPs injection (F, G). Blue: nuclei Hoechst staining. Images were taken with 5× magnification (A, F) and 50× magnification images (B, E, and G). Scale bar: 200 μm (A, F), 20 μm (B, E, and G).

2.3.3 Correlation of cargoes and carrier in blood vessels of the retina

2.3.3.1 In vivo real-time monitoring fluorescent cargoes DiI or Rho123 and Cy5.5-PLGA carriers in retinal blood vessels by ICON

Detection of the fluorescence signal from cargoes could be misleading in estimation of the NPs, as it may reflect released dye and not the localization of the NPs per se. To be able to distinguish between released and encapsulated dye, PLGA covalently linked with Cy5.5 (Cy5.5-PLGA) was used. After the first set of experiments with DiI, it was investigated that whether lesser amounts of Cy5.5 could be used, while still yielding a

sufficient signal. It was found that brightness of nanoparticles did not change significantly while the Cy5.5-PLGA fraction used in the preparation increases up until a threshold of about 60% (by weight): 0.74×10^6 $M^{-1}\cdot cm^{-1}$/mg and 1.04×10^6 $M^{-1}\cdot cm^{-1}$/mg at the Cy5.5-PLGA/PLGA ratios (100 mg:500 mg and 100 mg:100 mg, respectively). Given that alterations to the NPs compositions should be minimal when labeling them for visualization, the (100 mg: 500 mg) of polymers in further experiments with Rho123 was used.

The spatial and temporal monitoring of Cy5.5-PLGA and their cargoes are conducted and shown in Figure 2.6A and 2.6B. Difference in DiI and Rho123 kinetic was similar to previous experiment i.e. slow decay in DiI and fast disappearance of Rho123 (Figure 2.4). There was bright signal of Cy5.5 and this signal slowly declined to approximately 67% from maximum at the end of experiment of Cy5.5-PLGA-DiI. DiI fluorescence was changed in parallel with Cy5.5 signal. In contrast, in Cy5.5-PLGA-Rho123, Rho123 signal disappeared in 15 min, although Cy5.5 was still present (>90 min). The quantified profile of fluorescence of Cy5.5 covalently bound to the NPs and that of the cargoes DiI or Rho123 are displayed in Figure 2.6C and D, respectively. The $t_{1/2}$ of normalized fluorescence for Cy5.5 (177.9 min) in the retinal blood vessels was longer than that of the DiI (80.8 min), when Cy5.5-PLGA-DiI/P188 were injected. In Cy5.5-PLGA-Rho123/P188 NPs group, both NPs and Rho123 cargoes showed a rather quick elimination from the blood vessels: $t_{1/2}$ values of normalized fluorescence in the retinal blood vessels were 28.9 min and 6.6 min, for Cy5.5 and Rho123, respectively. Cy5.5 sustained longer in the group treated with the Cy5.5-PLGA-DiI/P188 NPs as compared to the Cy5.5-PLGA-Rho123/P188 NPs.

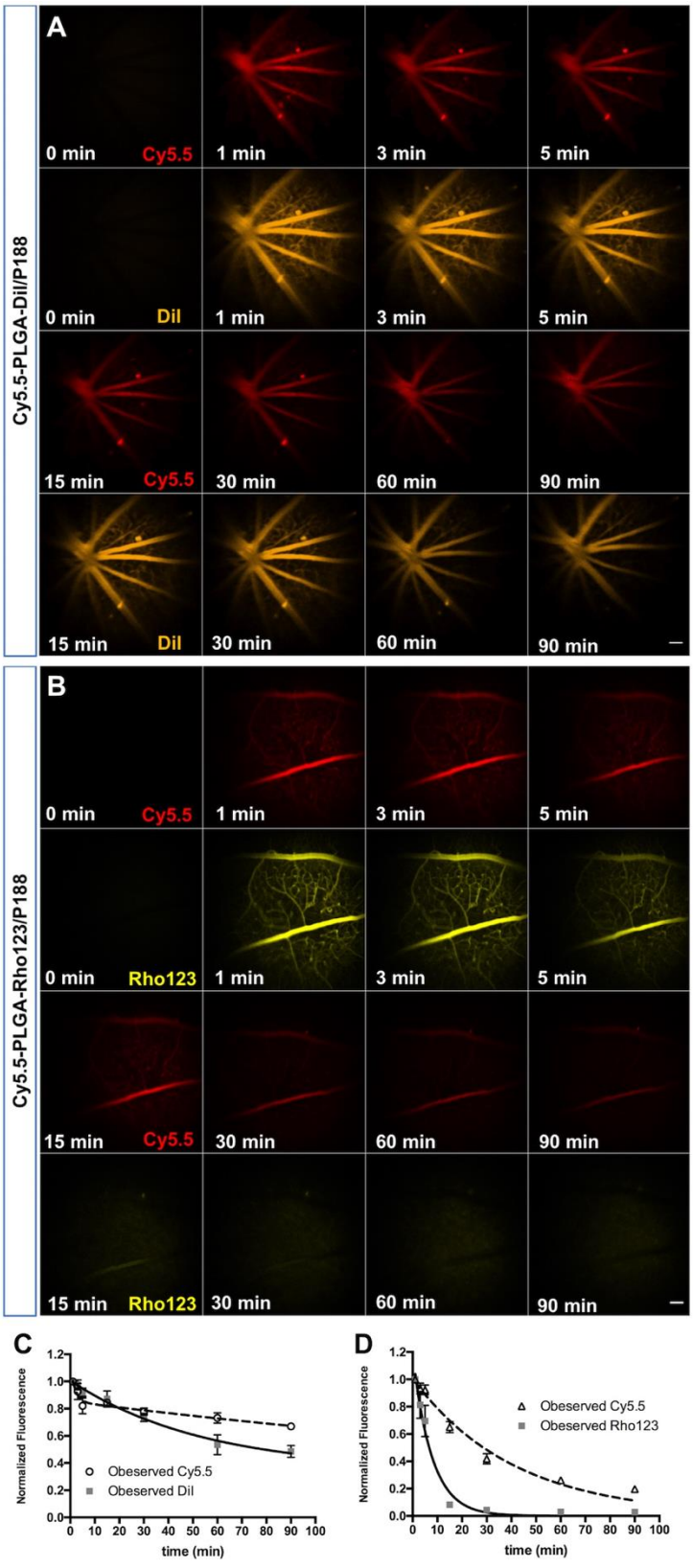

Figure 2.6 *In vivo* real-time signal monitoring of PLGA carriers covalently labeled with Cy5.5 and loaded cargoes DiI or Rho123 in retinal blood vessels.

DiI and Cy5.5 signals were quantified in the branches of retinal blood vessels after intravenous injection of Cy5.5-PLGA-DiI/P188 NPs (A) or Cy5.5-PLGA-Rho123/P188 NPs (B). Images were captured before injection (0 min) and until 90 min at defined time points by ICON technique. Scale bar 100 µm. C, experimental data of normalized fluorescence intensity of Cy5.5, DiI and corresponding fitting curve (line) (n=3, error bars represent mean ± SEM). D, experimental data of normalized fluorescence intensity of Cy5.5, Rho 123 and corresponding fitting curve (line) (n=4, error bars represent mean ± SEM).

2.3.3.2 Ex vivo localization of cargoes DiI, Rho123 and Cy5.5-PLGA carriers in retinal blood vessels

Figure 2.7A shows the distribution of Cy5.5-PLGA carriers in the retinal blood vessels at 2 h after injection of Cy5.5-PLGA-DiI /P188 NPs as sparkling spots that overlap with DiI signals. However, a pronounced, diffuse of DiI signal was also found on the blood vessel wall, which is consistent with results shown in Figure 2.5A-E. In Cy5.5-PLGA-Rho123/P188 NPs group, signal from Cy5.5-PLGA vehicles still existed after 2 h; on the contrary, Rho123 signals were too weak to be detected at this time point (Figure 2.7B). Therefore, to further evaluate the dynamic of PLGA-Rho123/P188 NPs in the retinal blood vessels, retinal flat mounts at 5 min after injection of PLGA-Rho123/P188 NPs were analyzed. Here, both Cy5.5 signal from PLGA polymer and the Rho123 cargo showed strong fluorescence at the same location (Figure 2.7C). Plot profile of Cy5.5-PLGA NPs, DiI signal and Hoechst are shown in Figure 2.7D, demonstrating that some of the Cy5.5 signals colocalized with DiI signal in the blood vessels (BV). However, DiI was also visible beyond the NPs spots as indicated in both Figure 2.7A and the green curve from BV on the right side of Figure 2.7D. This suggests that DiI had diffused out of the NPs and stained the blood vessel wall within 2 h. To further quantify the relationship of signals from Cy5.5-PLGA NPs, cargo DiI and Hoechst (cell nuclei), overlap score at different threshold (TOS) metric matrix from two signals were also presented (Stauffer et al. , 2018). The matrix showed negative values between Cy5.5 and Hoechst. This can be interpreted as antilocalization (Figure 2.7E), indicating that the PLGA NPs are not colocalized with nuclei of cells in retina tissue at 2 h after injection. Conversely, TOS metric matrix in Figure 2.7F showed colocalized values between Cy5.5 and DiI, confirming the visual evidence from Figure 2.7A. Specifically, in the Cy5.5-PLGA-Rho123/P188 group, the Cy5.5 signal from PLGA NPs at 2 h (Figure 2.7G) was strong and clearly detectable, whereas the Rho123 signal was virtually completely gone. In contrast, at the 5 min time point after injection both Cy5.5 signal from PLGA polymer with Rho123 cargo showed high intensity (Figure 2.7J). All TOS matrix showed that Cy5.5 have similar antilocalization or non-

colocalization with Hoechst (Figure 2.7H and K). Nevertheless, Cy5.5 has low colocalization with Rho123 at 2 h after injection (Figure 2.7I) and high colocalization with Rho123 at 5 min (Figure 2.7L). This is consistent with results shown in Figure 2.6B, that both signals, i.e. Cy5.5 from NPs and Rho123 as cargo, were observed at 5 min, however, at 90 min, only Cy5.5 signals from NPs were detectable. Localization was also furtherly confirmed and evaluated using three correlation coefficients: TOS_h, PCC and SRCC. TOS_h represents threshold overlap score at highest intensity which can better illustrate the correlation between two on-target signals (Stauffer et al., 2018). In the Cy5.5-PLGA-DiI/P188 group, the values for TOS_h, PCC, and SRCC were used to evaluate the relationship between Cy5.5 and DiI which were 0.412 ± 0.020, 0.603 ± 0.018, and 0.407 ± 0.036, respectively, at 2 h (Figure 2.7M). This indicates the partial colocalization between PLGA vehicles and DiI cargoes, which is consistent with Figure 2.7A and D; values for TOS_h, PCC, and SRCC between Cy5.5 and Hoechst were -0.535 ± 0.095, -0.109 ± 0.023, and -0.177 ± 0.036 suggesting antilocalization between PLGA vehicles and cell nuclei (Figure 2.7M). Since the TOS_h score was highest score at the sites where Cy5.5 and Hoechst have the highest intensity signal representing the value of maximal on-target signals, it can be assumed that Cy5.5 is not colocalized with nuclei. When NPs were intravenously injected and measured after 2 h in the Cy5.5-PLGA-Rho123/P188 group, values for TOS_h, PCC, and SRCC between Cy5.5 and Rho123 were 0.069 ± 0.010, 0.125 ± 0.020, and 0.104 ± 0.040, which revealed a non-colocalization relationship (Figure 2.7N); however, at 5 min after injection, these values were 0.445 ± 0.053, 0.589 ± 0.061, and 0.472 ± 0.065 (Figure 2.7O) suggesting partial colocalization of PLGA vehicles and cargoes Rho123. Values for TOS_h, PCC, and SRCC between Cy5.5 and Hoechst were -0.656 ± 0.094, -0.109 ± 0.015, and -0.290 ± 0.056 at 2 h, and -0.846 ± 0.050, -0.130 ± 0.024, -0.328 ± 0.055 at 5 min also confirming the antilocalization of PLGA vehicles and cell nuclei.

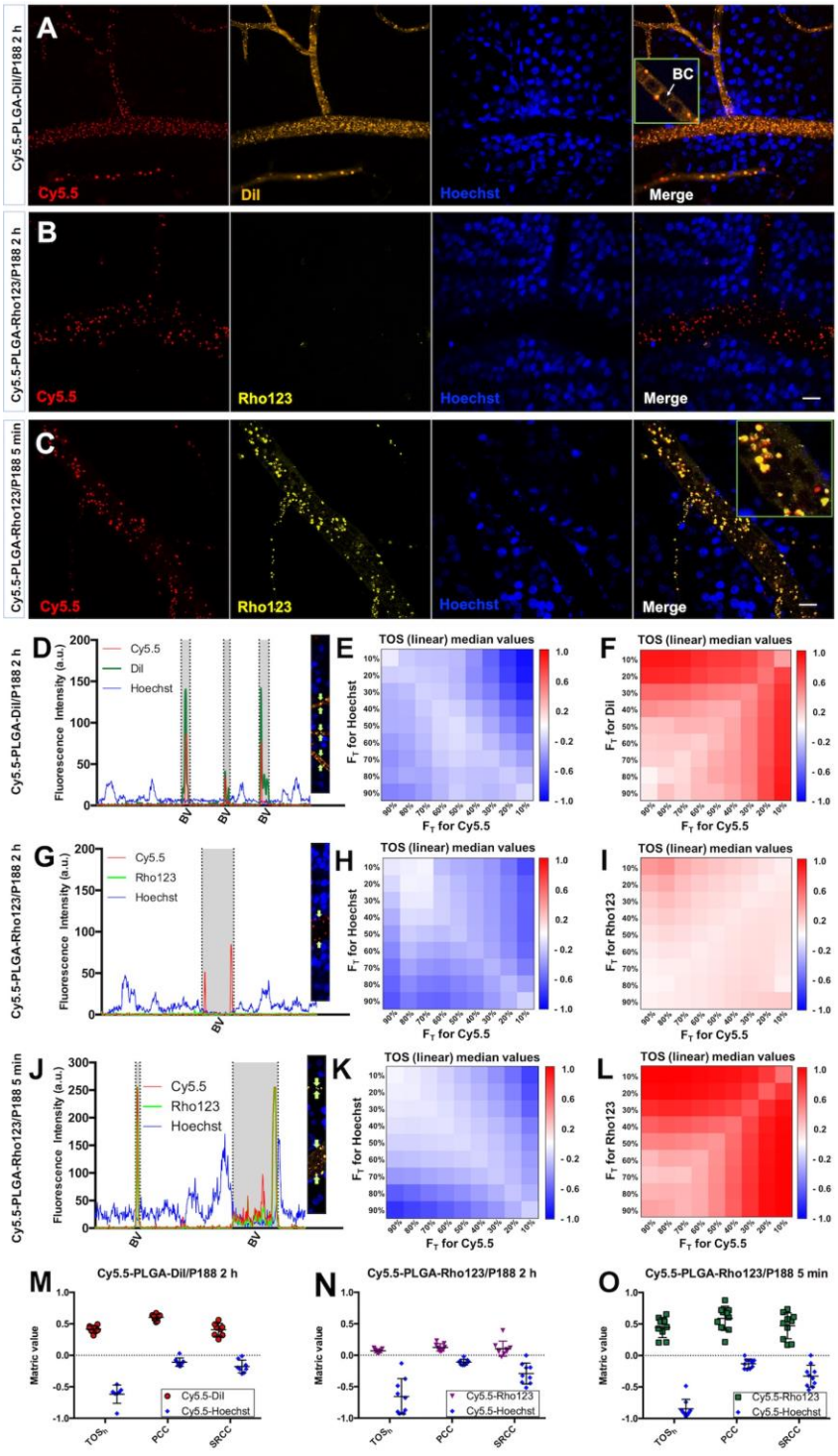

Figure 2.7 Localization of PLGA NPs (carriers) covalently linked with Cy5.5 and cargoes DiI or Rho123 in blood vessels in retinal flat mounts.

This graph shows the signals of DiI and Cy5.5 in the branches after intravenous injection of Cy5.5-PLGA-DiI/P188 NPs at 2 h (A), Cy5.5-PLGA-Rho123/P188 NPs at 2 h (B), and Cy5.5-PLGA-Rho123/ P188 NPs at 5 min (C). Scale bar 20 μm. A profile of fluorescence

intensity peaks from Cy5.5-PLGA, cargoes DiI, and Hoechst in the retinal flat mount (D), representative TOS matrix analysis for Cy5.5 and Hoechst at different thresholds (E) and representative TOS matrix analysis for Cy5.5 and DiI at different thresholds (F) in Cy5.5-PLGA-DiI/P188 2 h group. Similarly, a profile of fluorescence intensity peaks in the retinal flat mount for Cy5.5-PLGA, cargoes Rho123 and Hoechst (G), representative TOS matrix analysis for Cy5.5 and Hoechst at different threshold (H) and representative TOS matrix analysis for Cy5.5 and Rho123 at different threshold (I) in Cy5.5-PLGA-Rho123/P188 2 h group. A profile of fluorescence intensity peaks from Cy5.5-PLGA, Rho123, and Hoechst in the retinal flat mount (J), representative TOS matrix analysis for Cy5.5 and Hoechst at different threshold (K) and Rho123 at different threshold (L) in Cy5.5-PLGA-Rho123/P188 5 min group. TOS_h, PCC, SRCC values are evaluated from 8 blood vessels in the Cy5.5-PLGA-DiI/P188 2 h group (M), 9 blood vessels in the Cy5.5-PLGA-Rho123/P188 2 h group (N), and 10 blood vessels in the Cy5.5-PLGA-Rho123/P188 5 min group (O). Error bars represent mean ± SEM. BV, blood vessels. BC, blood cells. FT=the top percentage of pixels at different threshold in the channel. TOS_h=Threshold overlap score at highest intensity. PCC=Pearson correlation coefficient. SRCC=Spearman's rank correlation coefficient. Values, -1=complete antilocalization; 0= non-colocalization; 1=complete colocalization.

2.4 Discussion of Study I

PLGA NPs have gained a lot of attention as promising drug delivery systems and they are excellent candidates for the delivery of pharmacological treatment strategies. However, knowledge about the delivery system efficacy under real-life conditions is mandatory. In order to understand the kinetic profiles of nanoparticle systems in the retina, PLGA NPs were loaded with lipophilic DiI or hydrophilic Rho123. These dyes are widely used as fluorescent markers for PLGA NPs in different *in vitro* and *in vivo* experiments to estimate the biodistribution or cellular trafficking (Nakano et al., 2007; Chang et al., 2009; Simon and Sabliov, 2014). And they can be studied *in vivo* with real-time monitoring of the fluorescence signal in the retina using the ICON technique, the results of which can be confirmed by microscopy of flat mounted retina explants.

Importantly, to understand mechanisms of action, it is necessary to discern the cargo (here: the fluorescent dyes) and the carrier, i.e. the PLGA NP, and evaluate the cargoes which are not chemically linked to the nanocarrier so to estimate stability of the carrier-cargo system in the blood circulation *in vivo*. Therefore, to be able to differentiate between cargo and carrier, PLGA NPs were covalently linked with Cy5.5 to study the general principles of how nanoparticulate carrier-cargo-systems behave in the retinal blood circulation using the method of *in vivo* and *ex vivo* neuroimaging of the retina.

2.4.1 Different kinetic profiles of cargoes in blood vessels of the retina between hydrophilic Rho123 and lipophilic DiI (free or loaded in PLGA NPs)

Using the retinal model enabled us to compare *in vivo* real-time kinetic profiles of fluorescence dye in free form with that being loaded in PLGA NPs in the blood circulation of the retina. In this manner, a clear difference in the kinetics of free Rho and DiI was observed. Within 15 min after injection, Rho123 signal disappeared. The free DiI, however, showed a delayed staining phenomenon: fluorescence intensity increased within the first 15 min, and remained on this level for more than 1 h (Figure 2.4C). This effect could result from the physical property of DiI, which has a mild fluorescence in aqueous suspension but becomes quite bright once bound to cell membrane (http://products.invitrogen.com/ivgn/product/D282), reflecting binding of DiI to the vessel wall. In the case of the PLGA-DiI NPs, at the beginning, the bright signal of DiI loaded in PLGA NPs circulating in the vessels can be seen. Further, some amount of the dye was released from the NPs and stained the blood vessel wall, but most of the dye remained bound to the NPs and was eliminated from the blood flow. According to *in vitro* release profile (Table 2.2), only a small release during a rather long time (17.3 ± 1.4% and 13.2 ± 0.3% in 7 days) was found from PLGA-DiI NPs and Cy5.5-PLGA-DiI NPs. Given the high colocalization between the PLGA and cargo DiI at 2 h in retinal blood vessel (Figure 2.7F), it can be assumed that PLGA-DiI NPs or Cy5.5-PLGA-DiI NPs are stable during the experiment. When Rho123 was loaded in NPs, it showed similar kinetic as free Rho123, i.e., within 15 min, the Rho123 signal

disappeared from the blood vessels. At the same time Rho123 traces were found in the urine (Figure S1), and the Rho123 signal was virtually absent in the whole mount retina. When taken together, these findings can suggest a fast release of this hydrophilic dye from the NPs and further elimination from the blood via the kidney, which is consistent with the results reported by others (Mao et al., 2007; Voigt et al., 2014). The DiI signal from PLGA-DiI NPs had kinetic which were clearly distinct from free DiI. This fluorescence intensity decayed exponentially, but unlike the Rho123, it could be detected even after 2 h in the retina vessels. In general, the decrease of the signal from the cargo, loaded in NPs, can be due to elimination of NPs from blood flow or release of the cargo from NPs. The persisting DiI signal can be explained by a combination of fluorescence from the NPs and DiI released and bound to the vessel wall. In summary, it is not sufficient to limit the characterization of PLGA based drug delivery systems to the particles themselves, such as particle size, particle shape, and surface properties, but attention should also be paid to the properties of the individual cargo and the *in vivo* (blood circulation) environment.

2.4.2 Nano-carriers and cargoes have individual kinetic profiles

In the literature, the life cycle of NPs injected intravenously for drug delivery are in general described as follows: NPs encounter the target cell from blood circulation, its ligands or surfactant interact with the receptor of target cells, leading eventually to firm particle arrest. Next, the NPs are internalized into the target cells, and finally the drug is released from the NPs within the target cell (Singh et al., 2009). In this model, successful drug delivery is provided by tight integration of the carrier and cargo during *in vivo* blood circulation for the whole time. However, by covalently linking Cy5.5 to the polymer PLGA in this study, the *in vivo* real-time biodistribution kinetics at 15 min showed that the normalized fluorescence of Rho123 dramatically dropped to approximately 10% from maximum, conversely, normalized fluorescence of PLGA carrier decreased only by 30% (Figure 2.6B). This result indicates that at a later time point, i.e. >15 min, the Rho123 has diffused out of the particles and was eliminated

from the circulation, while the PLGA carrier continued circulation in the *in vivo* retinal blood vessels. This was confirmed by the *ex vivo* colocalization study showing absence of signal overlapping and negligible correlation between Rho123 and Cy5.5-PLGA at 2 h (Figure 2.7, TOS_h, PCC, and SRCC were 0.069, 0.125, and 0.104, respectively). Since Figure 2.6 C and J-L showed at 5 min time point post injection that the signal from cargo Rho123 is well colocalized with signal from Cy5.5 covalently linked carrier PLGA NPs, it can be assumed that the injected nanoparticles are stable at the beginning of the real-time monitoring. Though *in vivo* experiments with Cy5.5-PLGA-DiI NPs demonstrated a relatively strong signal at 90 min from both DiI and Cy5.5-PLGA, *ex vivo* colocalization measurement revealed the separation of the DiI signal and its PLGA carrier (Cy5.5), although to a lesser extent, (Figure 2.7, coefficient TOS_h = 0.412, PCC = 0.603, and SRCC = 0.407, respectively). Based on this observation, the integrity of nanoparticulate carrier-cargo systems and the efficacy of carrier-mediated delivery during *in vivo* circulation in the retina should be determined for each individual nano-carrier system when the cargoes are not covalently linked to the carriers.

2.4.3 Complex biological circulation in the retina *in vivo* changes nano-cargo-carrier system's behavior as compared to *in vitro*.

Blood flow is a complex biological system, with a number of parameters, which cannot be fully reproduced *in vitro*. Biological environments can greatly influence agglomeration, phase transformations, dissolution, degradation, protein adsorption, and surface reactivity of NPs, concomitantly, physicochemical properties of NPs change dynamically *in vivo* which makes the metabolism of NPs complex and difficult to predict (Wang et al, 2013). As the data of *in vitro* NPs characterization showed, approximately 50% of Rho123 and 90% of DiI is retained in the NPs after 24 h. Therefore, it could be expected that during the ICON experiment substantial fraction of the dye would be stored within NPs. However, both real-time kinetic profiles of PLGA NPs (Figure 2.6) and non-colocalization relationship between PLGA and Rho123 in Figure 2.7 present the merely negligible Rho123 contained within NPs in the blood

circulation of retina at 2 h. As mentioned above, it can be hypothesized that the fast disappearance of the Rho123 signal from the blood vessels is due to a faster release of this hydrophilic dye from the NPs and further elimination from blood circulation in the retina. In addition, the colocalization measurement suggests, that large fractions of DiI is also released from NPs (Figure 2.7). Presumably, multiple factors such as blood pressure, blood constituents (albumin, fibrinogen, immunoglobulin-G, etc.) and diverse fluid-particle interaction force (buoyancy force, local fluid acceleration force, etc.) (Green et al., 1999; Wajer et al., 2000; Jamshidi and Mazzei, 2018) are possible causes of faster cargo release from NPs and thus contribute to the difference between the *in vitro* and *in vivo* results.

2.5 Conclusion

It can be concluded that PLGA NPs' *in vivo* kinetic as imaged in the retina is a complicated process influenced by the chemical/physical properties of the blood and the individual properties of loaded compounds, which can significantly change the properties of PLGA NPs. Thus, developing efficient carrier-cargo systems requires careful design and individual examination of PLGA delivery systems.

In addition, real-time *in vivo* experiments, where the multiple factors of the biological milieu can interact and influence, provide valuable information regarding kinetics and distribution of NPs in the retina, which cannot be provided by *in vitro* assays. Although I have not yet been able to predict all the behaviors of different cargoes in PLGA NPs, these observations contribute to a better understanding of the relationship between design of nanoparticulate carrier-cargo systems and their kinetics in the blood circulation of retina. In any event, it seems unlikely that a single, universal nanoparticle formulation can be identified that is both safe and effective for the delivery of different compounds.

3. Study II: Exploring the systemic delivery of a poorly water-soluble model drug to the healthy or injured retina using PLGA nanoparticles[2]

3.1 Introduction to Study II

For many brain and eye diseases, only few causal drug treatments are available. Hence, there is a great need to discover new drugs alongside with the means to facilitate their delivery. Currently, the use of combinatorial chemistry and high throughput screening (HTS) allows identification of the new pharmaceutical compounds easier and faster than ever. However, formulation difficulties of drugs encountered in conventional approaches are among the major challenges in current drug development (Lipinski et al., 2000 and 2002). Especially, the delivery of poorly water-soluble compounds to target tissues is still a major challenge, as organic solvents are often associated with side effects (Broadwell et al., 1982; Galvao et al., 2014). An attractive strategy to broaden the application range of such compounds is to use nanoparticles (NPs) as a drug delivery method (Mersko-Liversidge and Liversidge, 2008). Over the decades many types of NPs have been developed, one of which is the highly biocompatible poly(lactic-co-glycolic acid) (PLGA) nanoformulation. The PLGA NPs have been widely studied and provide a successful approach for delivering drugs and various macromolecules such as proteins, nucleic acids and peptides (Makadia and Siegel, 2011; Danhier et al., 2012). Moreover, some PLGA-based applications have been approved already by the FDA for medical use (Qi et al., 2013; Wang et al., 2016; Bobo et al., 2016).

2. This work was published: Zhang, E., Osipova, N., Sokolov, M., Maksimenko, O., Semyonkin, A., Wang, M., Grigartzik, L., Gelperina, S., Sabel, B.A., Henrich-Noack, P., (2021). Exploring the systemic delivery of a poorly water-soluble model drug to the retina using PLGA nanoparticles. Eur. J. Pharm. Sci. 164, 105905. DOI: 10.1016/j.ejps.2021.105905

One potential application of PLGA NPs is the treatment of eye diseases. The loss or impairment of vision significantly reduces the quality of life, and some diseases, such as glaucoma, retinal ischemia, or mechanical optic nerve trauma, lead to impaired blood flow and vascular dysregulation (Flammer and Konieczka, 2017), and subsequently to insufficient nutrient and oxygen supply (Bien et al., 1999; Osborne et al., 2004; Mozaffarieh et al., 2008; Karande et al., 2020). Direct or indirect optic nerve injury also induces a decline of trophic factor concentration, some of which can be caused by an impaired retrograde axonal transport to the retinal ganglion cells (RGCs) from the target neurons in the visual thalamus (Cohen et al., 1994; Kostyk et al., 1994; Nickells, 1996; Chen and Weber, 2001; Weber et al., 2008). In addition, oxidative stress or increased glutamatergic stimulation could play a role in RGCs' death (Eltzschig and Eckle, 2011; Andreeva et al., 2015). These and other factors can contribute to RGCs pathology, degeneration and retinal function impairment. To protect RGCs, experimental drugs are being studied, and methods are needed to be explored, so that they can reach the posterior eye segment. However, when such neuroprotective drugs are applied systemically, the inner blood-retinal barrier (BRB) will be an obstacle. Its normal function is to protect neuronal cells and to regulate the microenvironment of the retina, but - at the same time - the BRB is also a barrier for most drugs or NP carrier systems which are unable to cross this barrier (Cunha-Vaz, 2004; Diebold and Calonge, 2010; Tomi and Hosoya, 2010; Hosoya et al., 2011; Kubo et al., 2014).

To overcome these drug delivery problems to the retina, pharmaceutical formulations will be needed. To better understand the complex spatial-temporal pattern of the release and the nano-carrier and cargo distribution in the intricate *in vivo* system, I explored a PLGA NPs based formulation of the model drug coumarin 6 (Cou6) for intravenous injection. Cou6 is a highly lipophilic fluorescent probe, which can be easily detected in the tissue and cells (Inokuchi et al., 2010; Rivolta et al., 2011). After intravenous injection of these Cou6 loaded NPs, the experiments were done to monitor Cou6 fate in real-time using *in vivo* Confocal Neuroimaging (ICON) which permitted non-invasive visualization of the retina in anesthetized animals (Sabel et al., 1997; Prilloff

et al., 2010; Zhang et al., 2020). To be able to distinguish the distribution kinetics of the Cou6 as a cargo and the NP as a carrier, PLGA NPs were then covalently linked with Cy5.5. Furthermore, to study the kinetics under pathological conditions, a rat optic nerve crush (ONC) model was used. ONC is a well-established experimental model to study traumatic optic nerve injury and to mimic the neuropathology of glaucoma, which is characterized by progressive optic nerve degeneration and loss of retinal ganglion cells (Tang et al., 2011), and which is associated with inner blood-retina barrier (BRB) breakdown (Cunha-Vaz; 1976). Moreover, we also wanted to evaluate if this optic nerve injury-induced retinal ganglion cell degeneration would have secondary effects on the blood compartment and the BRB. For example, Sato et al. found that the concentrations of 30 metabolites were changed after ONC in mice (Sato et al., 2018). In addition, during the traumatic and degenerative central nervous system (CNS) diseases the immune response can be dominated by resident and blood-borne macrophages (Cui et al., 2009; Schroeter and Jander, 2005). Joly et al. found that blood-borne macrophages can enter the eye through the optic nerve and ciliary body and migrate into the injured retinal area (Joly et al., 2009). These *in vivo* results were then compared to observations in flat mounted retinae to localize the Cou6 model drug and PLGA NPs on a cellular level.

The combined *ex vivo* and *in vivo* approach allowed us to systematically characterize the distribution kinetics of a poorly water-soluble model drug as a cargo and NPs in both healthy and damaged retina. To the best of our knowledge, it is the first time to directly visualize the kinetics of poorly water-soluble substances in the normal and damaged retina in real-time and propose that this kind of experimental approach can significantly increases our knowledge on systemic delivery of poorly water-soluble drugs via NPs across the inner BRB as a potential treatment of retinal diseases.

3.2 Materials and methods of Study II

3.2.1 Chemicals

Kolliphor P188®, poloxamer 188	BASF, Germany
Ketamine (100 mg/ml)	Medistar Arzneimittelvertrieb GmbH, Ascheberg, Germany
Medetomidine hydrochloride (1 mg/ml)	ORION Pharma GmbH, Hamburg, Germany.
Neosynephrine-POS 5%	Ursapharm GmbH, Saarbrücken, Germany
Vidisic® optical gel	Bausch & Lomb, Berlin, Germany
Saline (0.9%)	Fresenius Kabi Deutschland GmbH, Bad Homburg, Germany
Fluorescent Microspheres Red	Invitrogen detection technologies, Germany
Carprosol	CP-Pharma Handelsgesellschaft GmbH, Burgdorf, Germany
Liquifilm® eye drops	Allergan GmbH, Frankfurt am Main, Germany
Floxal®	Baush&Lomb, Germany
Hoechst 33342	Cayman Chemicals, Hamburg, Germany
Coumarin 6	Sigma-Aldrich, USA
other chemicals	Sigma-Aldrich

3.2.2 Poorly water-soluble PLGA NPs

The particles were provided by team of Dr. Svetlana Gelperina (D. Mendeleev University of Chemical Technology of Russia, Moscow, Russia). See publication (Zhang et al., 2021). Briefly, The PLGA-Cou6 NPs were produced by a high-pressure o/w emulsion solvent evaporation technique. Cy5.5-PLGA was produced by covalently linking Cy5.5 to the PLGA (Cy5.5-PLGA) via a carbodiimide coupling reaction

(Malinovskaya et al., 2017). The absence of free dye was verified by TLC on silica gel-coated plates.

Table 3.1 Physicochemical characteristics of PLGA-Cou6 NPs and Cy5.5-PLGA-Cou6 NPs

sample	Content of dye, μg/mg PLGA	EE	Before incubation in 1% P188			After incubation in 1% P188		
			Average size, nm	PDI	ZP, mV	Average size, nm	PDI	ZP, mV
PLGA-Cou6	22.0	92.5	128.6 ± 3.1	0.227 ± 0.075	30.7 ± 9.6	143.1 ± 4.1	0.308 ± 0.066	11.0 ± 0.5
Cy5.5-PLGA-Cou6	Cou6: 16.5 Cy5.5: 0.7	90.0	129.2 ± 2.7	0.168 ± 0.025	32.4 ± 3.5	134.2 ± 0.9	0.166 ± 0.029	12.7 ± 1.7

ZP: zeta potential; PDI: polydispersity index; EE: encapsulation efficiency. n=3, mean ± SD.

Evaluation of Cou6 release from PLGA-Cou6 NPs in vitro (were assisted by team of Dr. Svetlana Gelperina, D. Mendeleev University of Chemical Technology of Russia, Moscow, Russia)

The release of Cou6 from PLGA-Cou6 NPs was evaluated in 0.15 M PBS (pH 7.4) with the addition of 1% human serum albumin (HSA) for solubilization of Cou6 which was unencapsulated or released into an acceptor medium. The freeze-dried PLGA-Cou6 NPs were resuspended in the release media (25 ml), so that the total concentration for Cou6 was 16-17 μg/ml, and for the NPs – 0.73-0.77 mg/ml. Then the resulting suspension was incubated at 37 ºC under continuous shaking (orbital shaker-incubator ES-20, Biosan, Latvia). At chosen intervals, 1.0 ml aliquots of the suspensions were sampled, and the NPs were separated by centrifugation at 15000 g for 30 min at 18 ºC (Eppendorf, Germany). The amount of dye bound to NPs was determined after dissolution of the precipitate in DMSO spectrophotometrically. The experiment was performed in triplicates. The percentage of released/free dye was calculated by the

difference between the total content of the dye in the medium and that loaded in NPs related to the total content of the dye.

3.2.3 Animals and anesthesia

Adult male Lister hooded rats (Crl: LIS strain; Charles River), weighing 374 ± 39 g were kept on a 12 h light/12 h dark cycle at ambient temperature of 22 °C with humidity of 50-60%, and food and water ad libitum. Animals were handled for at least one week before experiment. The food was withheld before induction of narcosis. All manipulations on animals were performed under anesthesia with an intraperitoneal injection of ketamine and medetomidine (75 mg/kg and 0.5 mg/kg, respectively). All animals were treated in accordance with the requirement of the German National Act on the use of experimental animals (Ethic committee Referat Verbraucherschutz, Veterinärangelegenheiten; Landesverwaltungsamt Sachsen-Anhalt, Halle).

3.2.4 Retrograde labeling of the optic ganglion cells in the retina

Retrograde labeling was adapted as previous studies (Prilloff et al., 2007; Prilloff et al., 2010b; Henrich-Noack et al., 2013). The rats were anesthetized and placed on the stereotaxic apparatus after the fur was shaved from the head. The operation area was cleaned with 70% ethanol and locally anesthetized with proparacaine-POS 0.5 %. Thereafter, the skull was exposed with a midline incision, and for intracerebral injection, two small holes were drilled at 6.9 mm posterior to the bregma, 1.2 mm lateral from midline suture. Subsequently, 2 µl of Fluorescent Microspheres Red were gradually injected into the superior colliculus, 4.0, 3.5, 3.0 and 2.5 mm (each for 0.5 µl) below dura, using a 10 µl Hamilton syringe, over the course of 3 min on each side. The holes in the skull were closed by bone wax, and Floxal® was applied on the wound area before suturing the incision. Before the surgery, Carprosol was injected subcutaneously at a dose of 4 mg/kg. Vidisic® eye gel was applied to protect the eye from drying out, and eye patches were used to protect eyes from light during the whole procedure.

3.2.5 Optic nerve crush (ONC) model

Retrograde labeling was adapted as previous studies (Prilloff et al., 2007; Prilloff et al., 2010b; Henrich-Noack et al., 2013). The proparacaine-POS 0.5 % ophthalmic drops were applied to the surgical eye of anesthetized rats, while Liquifilm® eye drops were applied to another eye to prevent corneas from drying out during the operation. A small incision was made in the superior conjunctiva to allow gently outward retraction of the globe with fine forceps. The optic nerve was exposed and crushed at 2 mm away from eyeball with self-closing forceps for 30 s. Floxal® was used on the wound area to prevent infection.

3.2.6 *In vivo* real-time monitoring PLGA-Cou6 NPs or Cy5.5-PLGA-Cou6 NPs in retina

The distribution of PLGA-Cou6 NPs or Cy5.5-PLGA-Cou6 NPs were monitored by the *in vivo* confocal neuroimaging (ICON) system as described elsewhere (Sabel et al., 1997; Prilloff et al., 2010; Zhang et al., 2020). Shortly, a cannula was inserted into the tail vein of the anesthetized animals. Neosynephrine-POS 5% was used to relax the iris and Vidisic® eye gel was applied to protect the eye from drying out. Afterwards, the rats were fixed on the table of an ICON system with the eye positioned underneath the microscope objective. A contact lens was placed on the eye of interest. NPs in lyophilized form were dispersed in 0.5 ml sterile 1% poloxamer 188 (P188) solution, vortexed gently and left for 30 min at ambient temperature. 0.5 ml of suspension of PLGA-Cou6 NPs (Cou6: 0.74 mg/kg) were administrated intravenously via tail vein to the control group (rats without optic nerve crush) and ONC-1h (rats post optic nerve crush by hour 1) to check the influence of acute optic nerve injury on the kinetics of PLGA-Cou6 NPs. In addition, as shown in the previous study in the retinal blood circulation (Zhang et al., 2020), detection of the fluorescence signal from cargo did not reflect well the NPs location per se but rather the released dye. To be able to distinguish between the released Cou6 and the PLGA NPs, PLGA covalently linked with Cy5.5 (Cy5.5-PLGA) NPs were used, and the kinetics of Cy5.5-PLGA-Cou6 NPs (Cou6: 0.13

mg/kg) in the retina were investigated not only in the control group, but also in the ONC-1h group and the ONC-7d group (rats post optic nerve crush by day 7) as well. The images were captured at different time points within 90 min post injection. The image taken before i.v. injection represented the baseline (in text referred as time point 0 min). During the whole *in vivo* imaging process, the rats were kept on the heating plate.

3.2.7 Microscopy of PLGA-Cou6 NPs or Cy5.5-PLGA-Cou6 NPs in retinal flat mount

Animals were euthanized by triple overdose of narcosis inducing drugs. Eyes were immediately enucleated and placed in the HEPES buffered solution (135 mM NaCl, 5 mM NaOH, 2.5 mM KCl, 7 mM $MgCl_2$, 10 mM HEPES, 10 mM glucose; pH 7.4). The anterior segment of eye and vitreous were removed, the retina was then carefully separated, and mounted on modified culture plate with the ganglion cell layer (GCL) facing up. For nuclei staining, the whole mounts were then incubated with 0.1 mg/ml Hoechst 33342 (Hoechst) in HEPES solution for 20 min. 4% paraformaldehyde solution was dropped on the flat retina mount, left for 20 minutes and gently rinsed afterwards with HEPES solution. The eye which received no crush was used as the control in retinal flat mount experiment.

3.2.8 Tissue biodistribution of Cou6 encapsulated in PLGA NPs

Post intravenous injection of PLGA-Cou6 NPs at 2 h, rats were then sacrificed, and the heart, lung, liver, spleen, kidney, and brain were dissected and washed with saline for 3 times. Representative tissue samples were diluted 5-fold with an ice-cold saline solution (1 g tissue in 5 mL saline), homogenized by a homogenizer (Leuven, Belgium) and further dispersed by ultrasonic for 15 min. Tissue homogenates were centrifuged (5000 r/min, 10 min, 4 °C), and the 1 mL supernatant was diluted with 2-fold methanol for the second centrifugation to extract fluorescent dye from homogenate (8000 r/min, 10 min, 4 °C). The final 2 ml of homogenate extraction were used for fluorescent

detection. For the serum collection, blood was drawn from the abdominal aorta before sacrifice and centrifuged at 4 °C, 8000 r/min for 10 min. The resulting 500 µl sample was analyzed by fluorescence spectrophotometer (Agilent Technologies, Santa Clara, CA, USA).

3.2.9 Statistical analysis

The fluorescence signals from ICON in retina were quantified by Image J (US National institutes of Health, Bethesda, USA). By quantification, it is referred to as semi-quantification in the latter description. To reduce the influence from the Cou6 fluorescence in the neighboring retinal tissue on the retinal blood vessel, gamma correction (Song et al., 2008; Psiuk-Maksymowicz et al., 2014; Almada, et al., 2019) was applied before reading the Cou6 fluorescence in *in vivo* imaging. In the real-time kinetic study, the signal value at given point was normalized to the fluorescence in blood vessel post i.v. injection of NPs at 1 min. The normalized signal values in the retinal blood vessel were fitted with built-in mono or bi-exponential function by MATLAB (MathWorks, Inc., Natick, MA, USA). The time points when the normalized fluorescence declined to half value from maximum (i.e. 0.5) were evaluated based on the fitted curve. Independent sample median test or one-way ANOVA was used to compare the difference among multiple groups by SPSS (IBM Corporation, NY). A value of $P < 0.05$ was considered statistically significant. The colocalization of fluorescence signals was evaluated by estimating overlap score at different thresholds (TOS) with the EzColocalization ImageJ plugin (Stauffer et al., 2018). Briefly, the thresholds were chosen stepwise as the percentile (FT) of pixels for signal intensity to systematically measure colocalization, and a threshold overlap score was calculated and defined within a range between -1 and 1, (-1, antilocalization, 0 = no colocalization; 1 = full colocalization). Plots and charts were made by Graphpad Prism or Excel.

3.3 Results of Study II

3.3.1 Nanoparticle characterization

The physicochemical parameters of the PLGA-Cou6 NPs and Cy5.5-PLGA-Cou6 NPs are shown in Table 3.1. Both NP types had a similar hydrodynamic diameter of approximately 130 nm and exhibited high encapsulation efficiency of Cou 6 reaching circa 90%. Due to surface modification with PDMAEMA, the NPs had a positive surface charge of approximately +30 mV. After coating with P188, a slight increase in size of NPs (5-14 nm) and reduction of the zeta-potential (Table 3.1) indicated indirectly the adsorption of P188 onto the surface of nanoparticles. It was previously reported that the adsorbed polymer macromolecules of poloxamer are responsible for the decrease of the zeta potential connected with the shift of the slipping plane from the solid surface (Ostolska and Wiśniewska, 2014). Additionally, the influence of the P188 coating on the physicochemical parameters of the PLGA-NPs was also observed in other studies, where this reflected an increase of their hydrodynamic diameters and some alteration of the zeta-potential (where the extent of these changes depended on the NP composition and experimental settings) (Santander-Ortega et al., 2007; Jain et al., 2013). To prevent sedimentation of poorly soluble Cou6 in aqueous media, the *in vitro* release assay of Cou6 from the PLGA-Cou6 NPs was performed in 0.15 M PBS (pH 7.4) with the addition of 1% HSA, since it is the most abundant plasma protein in the blood, which may also act as a solubilizer (Albumedix Ltd., 2020). Approximately 36.2% Cou6 quickly diffused from PLGA NPs into the medium during the first 2 h, but no obvious additional release was observed up to 24 h (Figure 3.1A). In addition, an incubation of the PLGA-Cou6 NPs coated with P188 in PBS for up to 90 min did not have obvious influence on their size (Figure 3.1B).

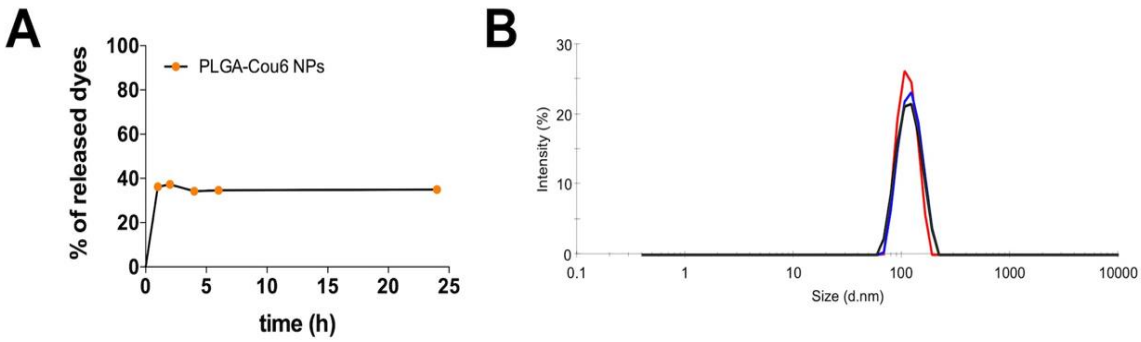

Figure 3.1 Nanoparticle characterization.

(A) The release profile of Cou6 from PLGA-Cou6 NPs in 1% HSA in 0.15 M PBS (pH 7.4). (B) Examples of particle size distribution of PLGA-Cou6 NPs coated with P188 in PBS after 10 min, 30 min, 60 min, and 90 min, respectively. Blue line, incubation for 10 min; red line, incubation for 30 min; black line, incubation for 60 min; green line, incubation for 90 min.

3.3.2 *In vivo* real-time monitoring the distribution of PLGA-Cou6 NPs or Cy5.5-PLGA-Cou6 NPs in the healthy or optic nerve injured retina

After i.v. injection of PLGA-Cou6 NPs, the Cou6 fluorescence signal reached its maximum at the beginning of the first minute in the retinal blood vessels, then the bright Cou6 signal on the blood vessel wall was observed at 3 min in the control group (Figure 3.2A), as well as in the group with ONC by hour 1 (Figure 3.2B). The results showed that at the subsequent time span of 15-90 min, the Cou6 signal was mainly detected in the retina tissue in both groups. The kinetics of Cou6 signal in the retinal blood vessels and that in the tissue in each group were also compared by quantifying the observed signals (Figure 3.2C and 3.2D). As shown in Figure 3.2C, the signal of Cou6 in the control group decreased dramatically within the first 5 min in the retinal blood vessels; conversely, in the retinal tissue, the signal gradually increased in this time span, continued to rise until 30 min post injection, and maintained the high level within the observation time from 30 min to 90 min. In the group post ONC by hour 1, similar kinetic profiles were found in the two compartments as they are in the control group (Figure 3.2D). The kinetic profiles in the blood vessels and in the retinal tissue in both

groups suggest that at least a fraction of the fluorescent probe Cou6 as a lipophilic model drug crossed the inner BRB.

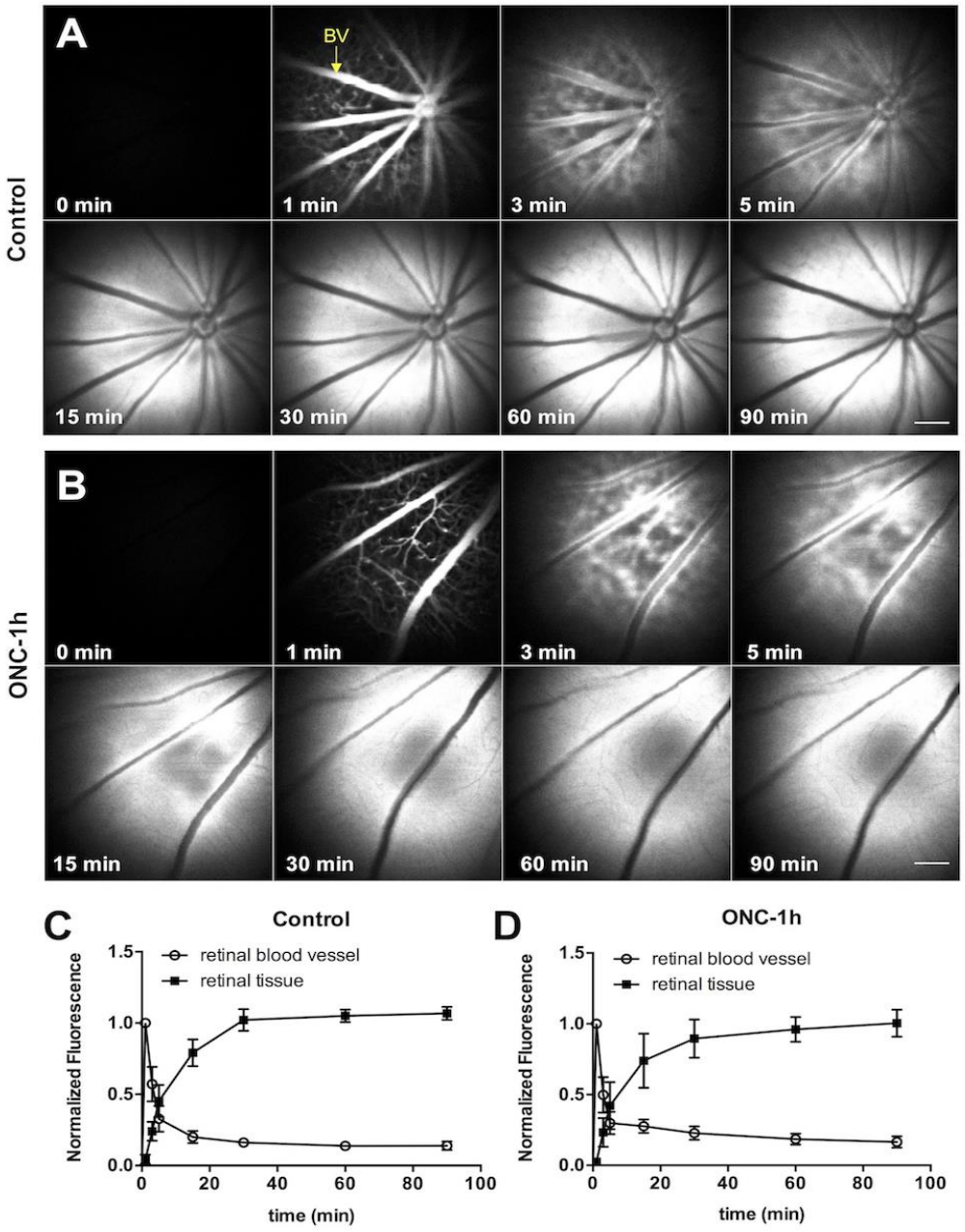

Figure 3.2 *In vivo* retina imaging of Cou6 in the healthy retina and acute optic nerve injured retina.

(A-B) After i.v. injection of the PLGA-Cou6 NPs coated with P188, the signal of Cou6 was captured in control group and ONC-1h group. (C-D) kinetics of Cou6 signal in retinal blood vessels and retinal tissue in each group are shown, respectively. n =5-6 (mean ±

SEM). The Cou6 signal was captured before injection (0 min) and until 90 min at defined time points by the ICON technique. Scale bar 400 μm. BV: blood vessels. ONC, optic nerve crush. NPs were coated with P188.

Subsequently, whilst the spatial and temporal distribution of Cy5.5-PLGA NPs and the cargo Cou6 in control group (Figure 3.3A) and post ONC by 1 h (Figure 3.3B) were observed until 90 min as well, this distribution was further detected in rats 7 days post-ONC (Figure 3.3C). As shown in Figure 3.3A-3.3C, the Cou6 signal also declined in the retina blood vessels vigorously, while it increased in the retinal tissue gradually in all groups. The observed signals were also quantified. As shown in Figure 3.3D, the kinetic profile in the retinal blood vessels post i.v. injection of Cy5.5-PLGA-Cou6 NPs showed that the Cou6 signal on average decreased considerably fast: the time points when the normalized Cou6 fluorescence declined to 0.5 in control group, ONC-1h group and ONC-7d group were at 4.7 min, 3.8 min, and 3.1 min, respectively. The parallel increase of the signal in the retina tissue was observed until the end of 90 min in all groups, and there was no obvious difference between these groups (Figure 3.3E). Surprisingly, the Cy5.5-PLGA signal in retinal blood vessels slowly decreased until the end of the experiment in both control group and ONC group by hour 1; however, this decline was faster in the ONC group by day 7 compared to the former two groups (Figure 3.3F). The time points when the normalized Cy5.5 fluorescence declined to 0.5 in control group, ONC-1h group and ONC-7d group, were at 81.5 min, 75.2 min, and 28.9 min, respectively. The Cy5.5-PLGA signal in the retina tissue remained at a low level during the whole experiment; no obvious increment was found in all three groups (Figure 3.3G).

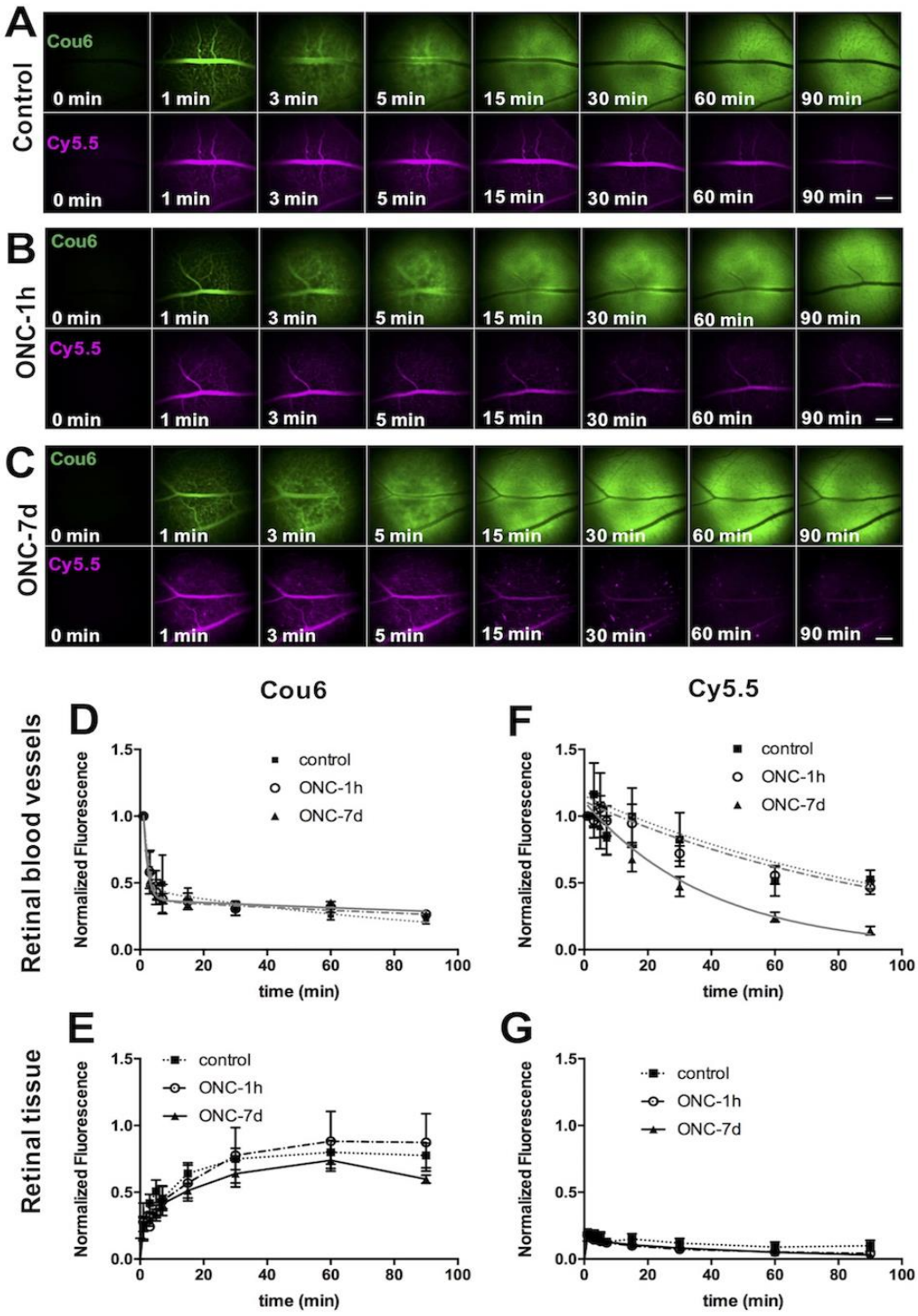

Figure 3.3 *In vivo* retina imaging of Cy5.5-PLGA-Cou6 NPs in the retina of healthy rats and rats with ONC.

NPs were coated with P188. (A-C) Observation of Cy5.5 and Cou6 signal in control group, group post ONC by 1 h, and group post ONC by day 7. Green: Cou6. Magenta: Cy5.5. Images were captured before injection (0 min) and until 90 min at defined time points by

ICON technique. (D-E) kinetics of Cou6 signals in the retinal blood vessels and those in retina tissue from all the groups. (F-G) kinetics of Cy5.5 covalently labeled PLGA NPs signals in the retinal blood vessels and those in the retina tissue from all the groups. n = 3-7 (mean ± SEM). Corresponding fitting curve of kinetics in retinal blood vessel in D (biexponential) and F (monoexponential) is shown in gray. ONC, optic nerve crush.

3.3.3 *Ex vivo* imaging of poorly water-soluble model drug Cou6 in retinal flat mount

After the *in vivo* real-time signal monitoring of Cy5.5-PLGA-Cou6 NPs in the retina (depicted in Figure 3.4A), the flat mount was further prepared to localize both Cy5.5 covalently linked PLGA NPs and poorly water-soluble model drug Cou6 on the cellular level. Figure 3.4B displayed that the Cou6 signal was mainly concentrated in the retinal tissue and it had relatively higher fluorescence intensity on the axon fibers. Microscopy under high magnification exhibited that the Cy5.5-PLGA NPs were mainly confined within the retinal blood vessels, whereas the fluorescent probe Cou6 was well defined around the cells and retinal blood vessel wall (Figure 3.4C). To further quantify the disposition of the Cou6, the colocalization was evaluated by overlap score at different threshold (TOS). TOS metric matrix in Figure 3.4D showed that the most of scores at different intensities were negative indicating the antilocalization between the Cou6 and Cy5.5-PLGA NPs post i.v. injection of Cy5.5-PLGA-Cou6 NPs. Likewise, the negative values of TOS metric presented in Figure 3.4E also showed that most of Cou6 signals were antilocalized with nuclei, indicating that the poorly water-soluble model drug Cou6 did not enter the nuclei. The TOS value at highest intensity representing the correlation of on-target signals, were -0.584 (between Cy5.5 and Cou6) and -0.852 (between Cou6 and Hoechst), respectively. These outcomes implied that Cou6 diffused out of PLGA NPs during the retinal blood circulation and successfully crossed the inner BRB.

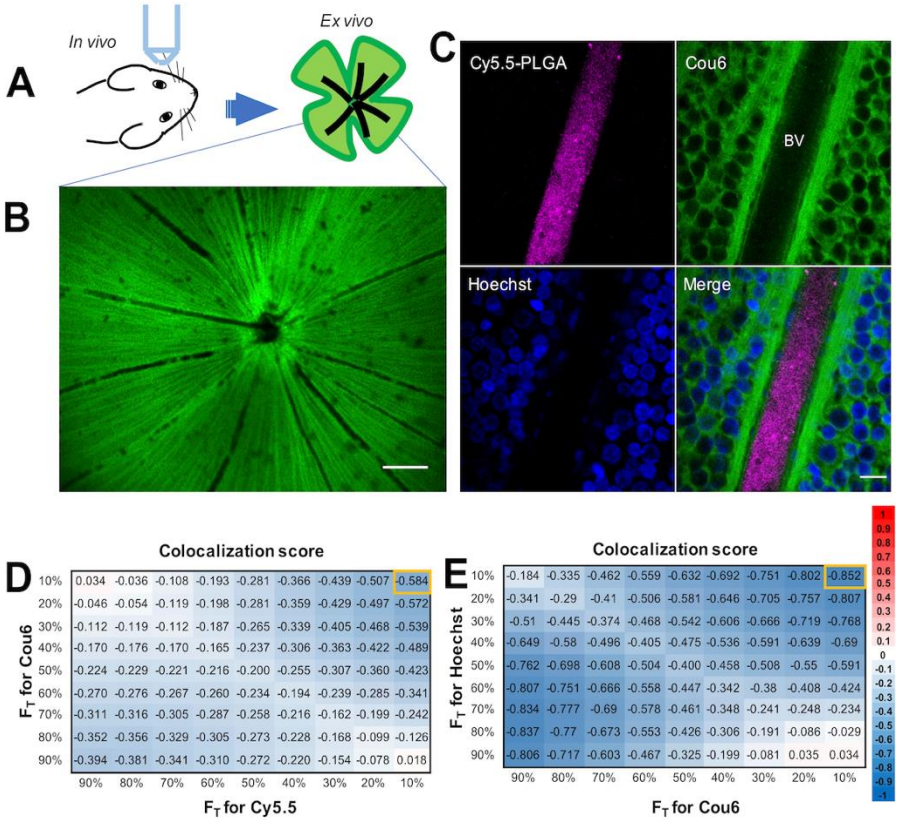

Figure 3.4 *Ex vivo* imaging of Cy5.5-PLGA NPs and Cou6 fluorescence in retinal flat mount.

(A) Schematic illustration of study design. (B) The Cou6 signal was mainly distributed in the retina tissue beyond the retinal blood vessels. (C) Localization of PLGA NPs covalently linked with Cy5.5 and cargo Cou6 in retinal flat mounts. (D-E) Colocalization between Cy5.5 and Cou6, and colocalization between Cou6 and Hoechst at different thresholds by TOS matrix analysis. F_T = the percentage of pixels at different thresholds in the channel. Yellow rectangle: overlap score at each highest intensity. Values, -1 = complete antilocalization; 0 = non-colocalization; 1 = complete colocalization. Images were taken with 5 × magnification (B) and 50 × magnification (C). Scale bar: 400 μm (B), 20 μm (C). NPs were coated with P188.

I next tested whether the fluorescent probe Cou6 as poorly water-soluble model drug released out of the PLGA NPs entered the RGCs. To this end, RGCs were retrogradely labeled by intracerebral injection of Fluorescent Microspheres Red into superior

colliculus (as depicted in Figure 3.5A) 7 days before i.v. injection of PLGA-Cou6 NPs and retinal flat mount preparation. Figure 3.5B demonstrated the successfully labeled RGCs illustrated as bright spots in the retina of anaesthetized rats under the ICON system. The image at high magnification showed that this fluorescent marker was mainly distributed in the cytoplasm of RGCs, but not in cell nuclei (Figure 3.5D). Microscopy of retinal flat mount displayed a slight Cou6 signal in the cytoplasm as observed following Fluorescent Microspheres Red retrograde labelling (Figure 3.5C and 3.5E). Plot profile of Cou6 signal in the GCL further confirmed that the signal was weak in the cytoplasm by comparison to the staining signal in the extracellular space (Figure 3.5F). The result of the colocalization between the RGCs labeling and Cou6 signal by TOS metric (Figure 3.5G) suggested that the Cou6 signal partially correlated with RGCs labeling at relative low thresholds. However, the most on-target signal at the highest threshold from each of them exhibited the negative score with -0.399 on average. This confirms the observation of low Cou6 accumulation in the cytoplasm and high enrichment in the extracellular space as demonstrated in Figure 3.5C and 3.5E. Furthermore, the negative values of metric (Figure 3.5H) were consistent with the observation in Figure 3.5C and 3.5D that the retrograde labeling markers were located in the cytoplasm of RGCs without labelling in the nuclei. It could be possible that poorly water-soluble model drug Cou6 is released from PLGA NPs, crossed the retinal blood vessels and had distributed in the parenchyma and, to limited extent, entered the GCL cells.

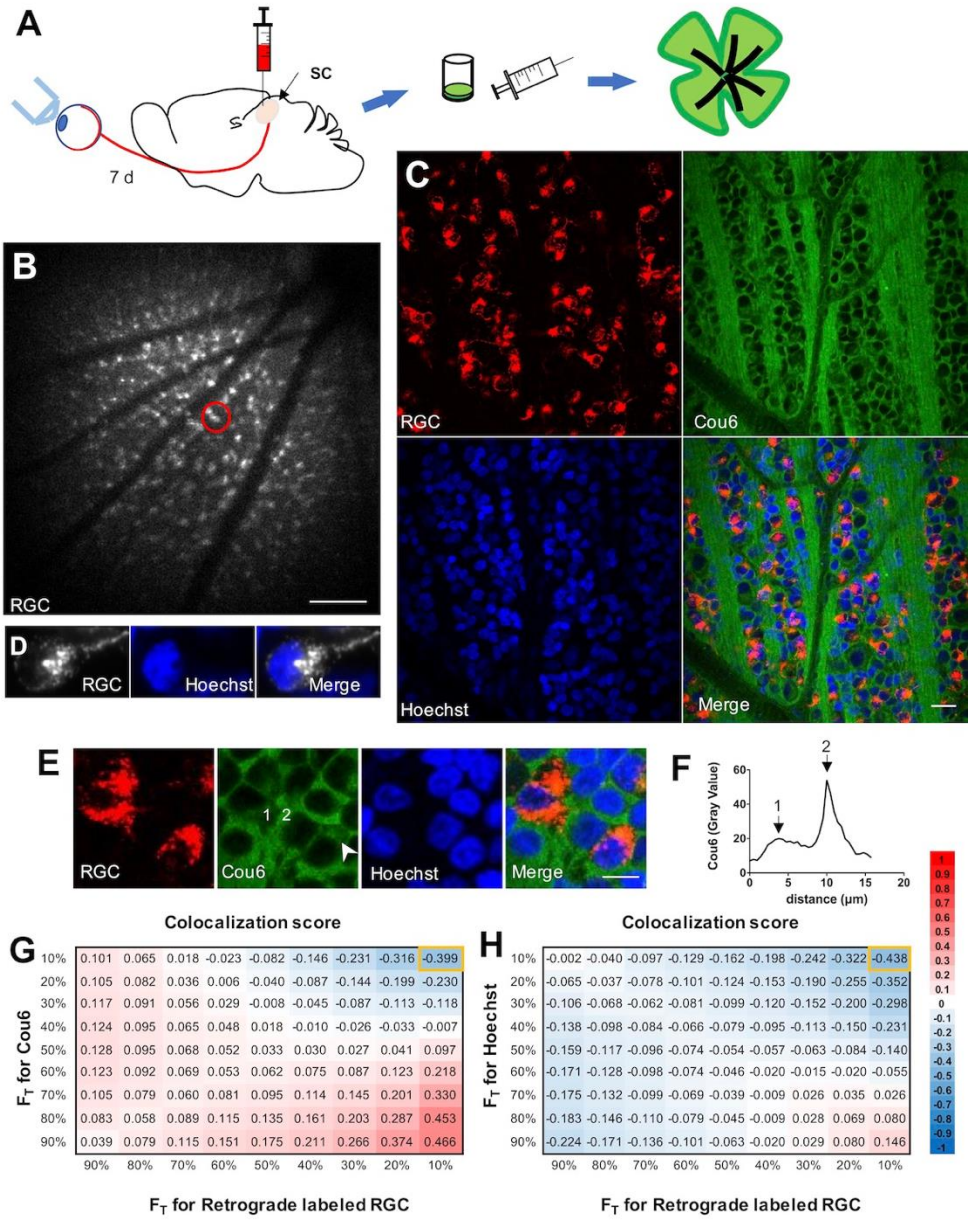

Figure 3.5 *Ex vivo* identification of released Cou6 distribution relative to RGCs in retina.

(A) Schematic illustration of study design that RGCs were retrogradely labeled 7 days in advance by intracranial injection of Fluorescent Microspheres Red into SC and the retinal flat mount were prepared post i.v. injection of PLGA-Cou6 NPs. NPs were coated with P188. (B) The retrograde labeled RGCs were observed in the eye of anesthetized rat by ICON technique. (C) Microscopy of Cou6 and RGCs signal in the retinal flat mount under 50× magnification. (D) Magnification of retrogradely labeled RGCs and nuclei stained by

Hoechst. (E) Magnification of distribution of Cou6 relative to RGCs in the retinal flat mount. Scale bar: 400 μm (B), 20 μm (C) and 10 μm (E). (F) Uneven Cou6 signal distribution in retina parenchyma. Arrows point to corresponding 1 and 2 in E. (G and H) Colocalization score between retrograde labeled RGCs and Cou6, and between retrograde labeled RGCs and Hoechst at different thresholds by TOS matrix analysis. RGC: retinal ganglion cell. SC: superior colliculus. Red circle in B: retrogradely labeled RGCs under ICON system. F_T=the percentage of pixels at different thresholds in the channel. Yellow rectangle: overlap score at highest intensity. Values, -1=complete antilocalization; 0= non-colocalization; 1=complete colocalization. NPs were coated with P188.

3.3.4 Distribution of poorly water-soluble model drug Cou6 in optic nerve injured retina

Compared to the retrograde labeled RGCs in control eyes (Figure 3.6A and 3.6C), several abnormal cells, well separated from each other, were observed in the eyes post optic nerve crush by day 7 (Figure 3.6B and 3.6C). To test whether the distribution area of Cou6 in the parenchyma of the GCL was statistically affected by optic nerve injury or not, the Cou6 signal projected in the 85 × 85 pixels selected area (Figure 3.6E) were analyzed, referring to a previous study (Nunan et al., 2015). It turned out that there was no significant difference between the distribution area of Cou6 in the retina parenchyma when comparing controls with ONC by hour 1 (Figure 3.6F). However, an obvious difference of that area was observed in the ONC group on postoperative day 7 (Figure 3.6F). Meanwhile, signal intensity in a few areas of GCL were altered under the influence of optic nerve injury: as shown in Figure 3.6D, a less intense fluorescence field on axon fibers on seventh day post crush appeared (arrow), compared to the other field in the same retinal flat mount or the axon fibers in other two groups. Subsequently, the Cou6 signal cross through the axon fibers in each group was analyzed and no significant difference of Cou6 signal of fibers between control group and group at first postoperative hour was found, but the signal at some points on the fibers in the group post injury on day 7 was reduced significantly (Figure 3.6G).

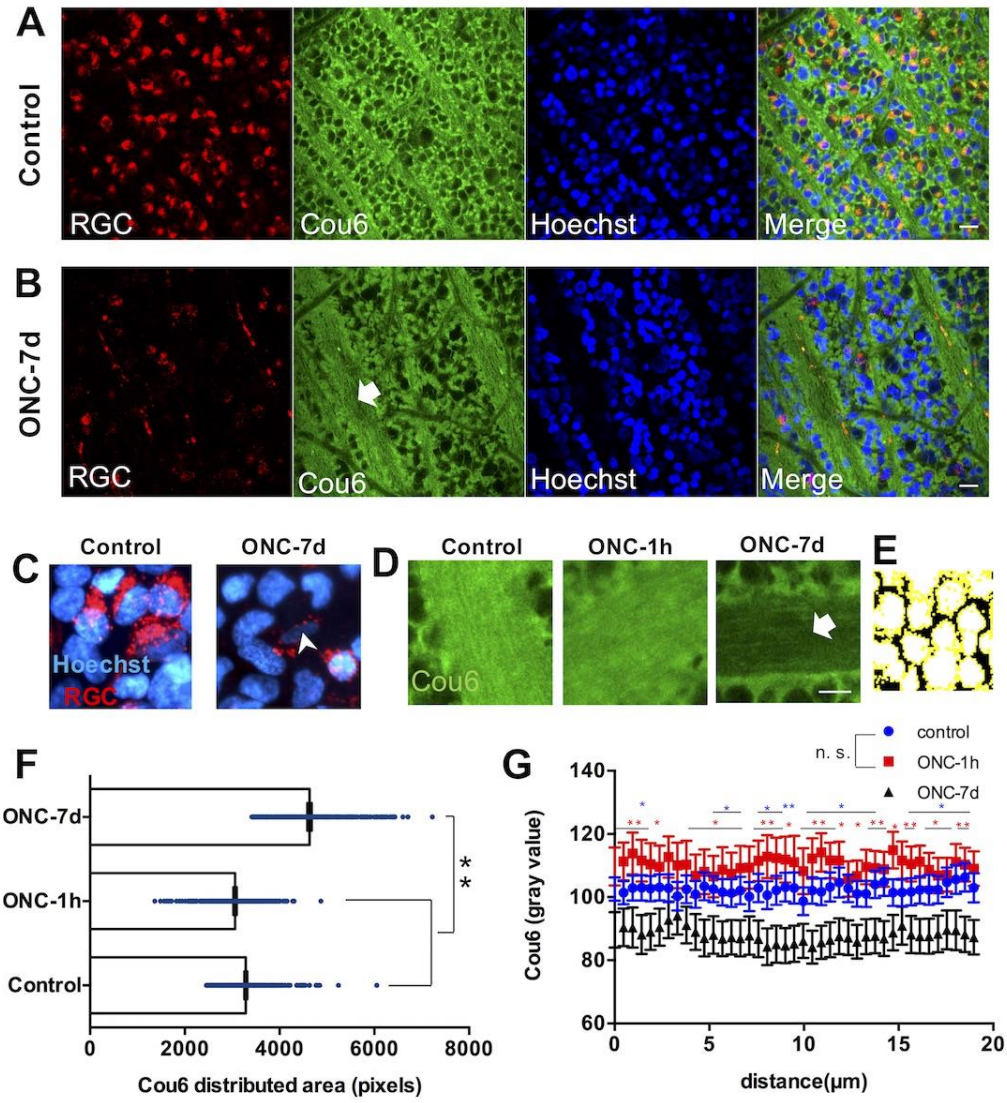

Figure 3.6 *Ex vivo* evaluating distribution of released Cou6 in GCL post ONC.

(A and B) The retrogradely labeled RGCs and Cou6 signal distribution in control eye and eye post ONC by day 7. (C) The representative morphology of RGCs in each group. (D) Representative Cou6 distribution on the axon fibers in control group, group post ONC by hour 1 and group post ONC by day 7. (E) Selection of Cou6 distribution in GCL in every 85 × 85 pixels. (F) The comparison of Cou6 distribution in GCL in every 85 × 85 pixels area of control group, group post ONC by hour 1 and group post ONC by day 7. ** P < 0.01, independent sample median test, n= 300, 263, and 300 areas (85 × 85 pixels). (G) The comparison of Cou6 on the axon fibers in each group (n = 31, 47, 56, error bars represent mean ± SEM, * P < 0.05, ** P < 0.01, n.s. no significant difference, one way-

ANOVA). Arrow in B and D, less Cou6 staining axon fibers post ONC by day 7. Scale bar: 20 μm (A and B), 10 μm (D). ONC, optic nerve crush.

3.3.5 Cy5.5-PLGA NPs in the healthy or optic nerve injured retinal blood vessels

PLGA NPs were well detectable in the relatively big retinal blood vessels in control eye for 2 hours (Figure 3.7A), while the NPs in the group by day 7 post ONC were hardly visible (Figure 3.7C). Plot profiles of these signals in the big retinal blood vessels confirmed the observation from the images that the NPs exhibited a high signal in control eye (Figure 3.7B), whereas in the vessels of group with ONC by day 7 (Figure 3.7D), the signals were extremely weak. A similar phenomenon was also observed in the relatively small blood vessels (Figure 3.7E and 3.7F). Plot profiles in Figure 3.7G displayed the Cy5.5-PLGA NPs restricted in the small blood vessels in control eye. Although the signal of Cy5.5-PLGA declined in the retinal blood vessels, no significant increase outside of the vessels in the retina tissue was detected (Figure 3.7H). Presumably, the inner BRB was not so much damaged post ONC by day 7, at least, no significant leakage of the inner BRB resulting in the increase of the Cy5.5-PLGA NPs outside retinal blood vessels was observed.

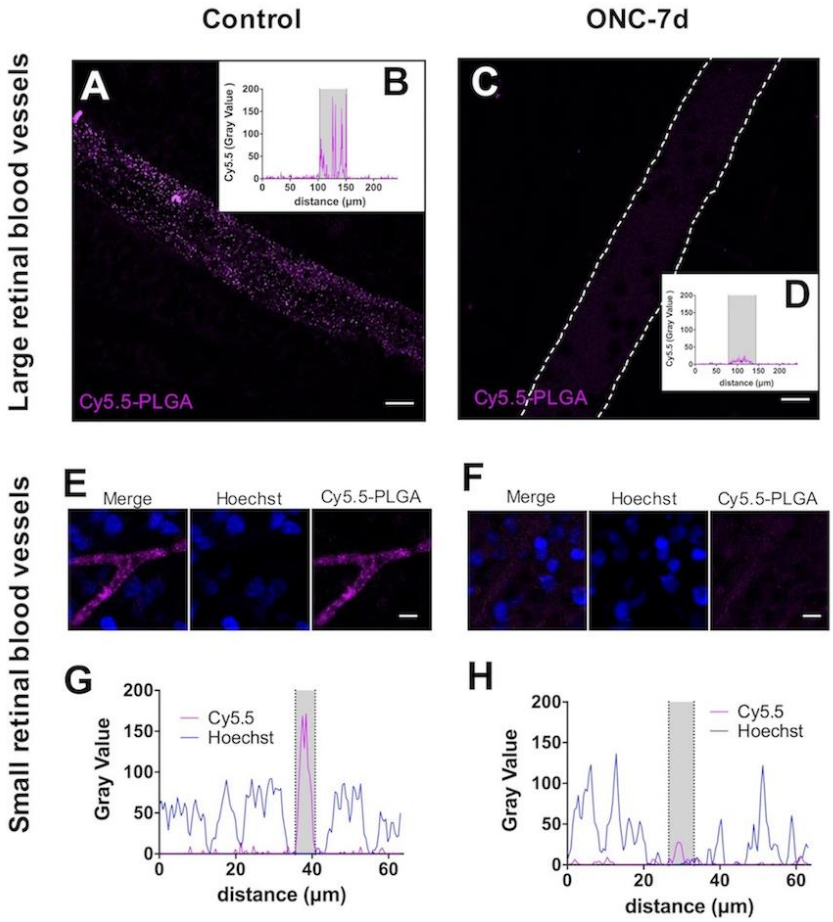

Figure 3.7 Evaluation of Cy5.5-PLGA NPs in large and small retinal blood vessels.

(A and B) The distribution of Cy5.5-PLGA NPs in the big retinal blood vessels (about 40-50 μm, diameter) in control eye and corresponding profile of fluorescence intensity peaks from Cy5.5-PLGA NPs. (C and D) The distribution of Cy5.5-PLGA NPs in the big retinal blood vessels in the eye post ONC by day 7 and corresponding profile of fluorescence intensity peaks from Cy5.5-PLGA NPs. (E and F) The distribution of Cy5.5-PLGA NPs in the small retinal blood vessels (less than 10 μm, diameter) in control eye and eye post ONC by day 7. (G and H) Corresponding profile of fluorescence intensity peaks from Cy5.5-PLGA and Hoechst in control eye and eye post ONC by day 7. Scale bar: 20 μm (A and C), 10 μm (E and F). Gray background in B, D, G, and H: retinal blood vessel. ONC, optic nerve crush.

3.4. Discussion of Study II

With the current experiments, two significant problems were addressed, concerning the drug treatment of retinal diseases and drug development in the pharmaceutical industry in general: (i) exploring the distribution of PLGA NPs which served as a carrier and a poorly water-soluble substance as cargo with *in vivo* and *ex vivo* fluorescent imaging in retina; (ii) whether pathophysiological conditions influence the distribution of the nano-carrier and its cargo. To this end, Cou6 was used as a poorly water-soluble model drug and its fluorescence was monitored to investigate the distribution in the retinal blood vessels and retinal tissue. Furthermore, to distinguish the kinetics of the PLGA NPs from the cargo, the PLGA polymer was covalently labeled with the fluorescent dye Cy5.5. In this way, whether the Cou6 cargo and the NPs-carrier were conjoined or whether the Cou6 was released from the carrier during the retinal blood circulation could be detected, as in the latter case their fluorescent signals would not overlap anymore.

One reason to investigate the opportunities of PLGA NPs as drug carriers was that this delivery system was already approved by the FDA for medical application (Danhier et al., 2012). Moreover, the previous work demonstrated that our PLGA NPs production protocol provides suitable NPs with uniform size distribution and long shelf life (Zhang et al., 2020). The NPs were stable upon lyophilization, and the reconstituted nanosuspension maintained colloidal stability. This demonstrated that such NPs formulation could be successfully used for i.v. administration of poorly water-soluble compounds. In the current work, the NPs' distribution in the rat retina was visualized by the ICON system. The advantages of observing the retina are that - being tissue of the CNS – its vessels have characteristics largely similar to the BBB and that although being part of the CNS (O'Brown et al., 2018), it is available for non-invasive *in vivo* microscopic imaging. Comparing the fluorescence of Cou6 in vessels and in retina tissue (Figure 3.2), a fast decrease of the signal in vessels and a sustained increase over the time of the experiment (90 min) in the retina tissue, was observed. This

demonstrated that the model drug Cou6 probably reached the retina parenchyma. However, these results did not provide yet an insight into the mechanism, i.e. whether Cou6 remained encapsulated or whether it was released from PLGA NPs during the retinal blood circulation when being detected in the tissue.

To distinguish if Cou6 was encapsulated in, or released from, PLGA NPs, the kinetic of Cou6 was compared with the Cy5.5 signal; it was found that there was a clear difference in the dynamics of these two signals. While the Cou6 signal increased in the tissue, the Cy5.5 fluorescence was mainly retained in the blood vessels and was not significantly detectable in retina tissue, which was validated both *in vivo* and in whole mount retinae (Figure 3.3 and Figure 3.4). In addition, the colocalization analysis of PLGA NPs in the retinal flat mount also indicated that Cou6 had diffused out of the PLGA NPs in the retinal blood circulation (Figure 3.4D).

The ideal scenario that one nanoparticle composition can be found, which could carry the different encapsulated cargos across the BRB or BBB as integrity, seems unrealistic at this time. The circumstances and factors influencing drug delivery are still too complicated to make this applicable in real life conditions. A study by Voigt et al. (Voigt et al., 2014), suggests that particle surface - rather than size or surface charge - is the key factor determining BBB passage. This conclusion was made using the poly(butyl cyanoacrylate) (PBCA) NPs when evaluating various parameters and a number of ionic and non-ionic surfactants for the NPs' coating. There, NPs coating with non-ionic surfactants polysorbate 80 and P188 produced the most effective penetration into the rat retina (Voigt et al., 2014). However, in further study, when designing more variations of PBCA nanocarriers, it was showed that not only surfactants but, indeed, also size and surface charge determine their ability to cross the blood-retina barrier (BRB) (You et al., 2018). What's more, even minor changes in these parameters substantially influenced particles' biological distribution *in vivo* (You et al., 2018). In a parallel study, the successful brain delivery of doxorubicin by PLGA NPs coated with P188 was demonstrated (Maksimenko et al., 2019). These NPs could

penetrate into the intracranial rat glioblastoma and delivered doxorubicin to the tumor (observed by fluorescent microscopy in brain sections) producing a considerable anti-tumor effect (Maksimenko et al., 2019). Together with the previous results obtained in the same tumor model (Gelperina et al., 2010; Wohlfart et al., 2011), these data indicated that the surfactant significantly facilitated delivery of doxorubicin into the brain of glioblastoma-bearing animals, whereas the particle size appeared to be less important. However, the results of the present study using PLGA NPs labeled with covalently bound Cy5.5 suggest that PLGA-NPs remained mainly in the blood vessels and did not prominently cross the BRB (Figure 3.3, 3.4 and 3.7). This observation correlates with the data of Khalin et al. who observed by fluorescence microscopy a similar continuous retention of the P188-coated poly(methyl methacrylate)-sulfonate NPs in the murine cerebral vessels whereas non-coated NPs were rapidly eliminated from the circulation (Khalin et al., 2020). This phenomenon can be attributed to the affinity of the P188-coated NPs to the endothelial cell membranes. Indeed, in a previous study coating of the PLGA NPs with P188 improved their internalization in the U87 cells via clathrin-dependent endocytosis (Malinovskaya et al., 2017).

Therefore, it seems the search for a “magic bullet”, a “one fits all” nano-carrier recipe does not look promising. Of course, efficacy of drug delivery depends on multiple factors as defined by a predetermined formula for coating of the NPs with surfactants along with the selection of the proper physicochemical parameters (e.g. NPs size and charge). However, the results of the present study provide another possibility, i.e. that such penetration is a complex event where the required parameters may not be translatable from one nanosystem to another and from one model system to another. In this respect, it can be assumed that the seeming contradiction with the aforementioned data (Maksimenko et al., 2019) regarding the P188-coated Dox-PLGA NPs observed in the brain tumor could be explained by their facilitated penetration across the BBB impairment which is typical for tumors.

Hypothetically, the fact that a significant signal of PLGA NPs in the retinal tissue was not detected, could be result from very fast nanoparticle degradation or accumulation of NPs in other organs and tissues. But the data do not support these hypotheses: more than 90 min post injection they are still clearly detectable inside vessels (Figure 3.3 and Figure 3.4). This finding suggested that Cou6 was quickly released from NPs and crossed the BRB, while the Cy5.5-PLGA was largely remaining in the blood. It can be assumed that, after being released, the Cou6's passage across the BRB is based on its physicochemical characteristics; Cou6-like highly lipophilic compounds are capable to easily permeate through biological barriers such as BRB and BBB. These barriers represent very comprehensive structures (Engelhardt and Coisne, 2011) and for each drug, a combination of physicochemical properties determines its potential to cross such physiological borders. For example, when the polar surface area (PSA) of a molecule decreased to < 60-90 $Å^2$, the barrier penetration can be expected (Kelder et al., 1999; Pajouhesh and Lenz, 2005). In this case, Cou6 has a topological polar surface area (TPSA), practically identical with the PSA with correlation coefficients of 0.99 (Ertl et al., 2000), around 70.7 $Å^2$ (PubChem Database, 2020), suggesting the ability of Cou6 to cross the BBB and BRB. Meanwhile, in general, the compounds should follow the Lipinski's rule to be able to permeate the membrane barriers (Lipinski et al., 1997). The corresponding properties mentioned in this rule for Cou6 are (i) 0 hydrogen bound donors, (ii) 5 hydrogen bound acceptors, (iii) molecular weight with 350.4 g/mol, and (iv) XLogP with 4.9 (PubChem Database, 2020), which fit perfectly in the range required for blood-brain barrier permeation.

In addition, it can also be hypothesized that the massive extravascular penetration of Cou6 across the BRB into the retina was assisted by the NPs that were associated with the vessel walls and thus could facilitate the dye entry into the endothelial cells in a kind of "kiss and run" fashion (Hofmann et al., 2014) i.e. similar to the concept which is established in physiology: it describes the process of vesicles docking transiently to the membrane, releasing its neurotransmitter and afterwards being detached (Fesce et al., 1994). This metaphorical analogy was used, and mechanism was studied already by

Hofmann et al. (Hofmann et al., 2014). In their study, it was found that poly-L-lactide based NPs can deliver a hydrophobic cargo within minutes and without entering the cell in a short contact way resulting in no necessity of NPs uptake (Hofmann et al., 2014). Correspondingly, it can be assumed that the NPs may enhance the retention of model drug on the endothelial cells and thereby promote further distribution of the model drug in the tissue. In any case, the results demonstrate that the nanoparticle penetration across barriers is not always a prerequisite for effective drug delivery: if the properties of the NPs allow for their continuous interaction (adhesion or internalization) with the endothelial cells forming the barrier, then the released drug is given the opportunity to successfully distribute into the tissue behind this barrier.

Also, under the current condition due to technique limitation, the level of the signal in the aqueous humor cannot be precisely evaluated. However, in this *in vivo* imaging study, from the preliminary 3D reconstruction of the Cou6 signal (Figure S2), it is highly likely that the Cou6 is mainly distributed in the retina. In addition, even though blood-aqueous humor barrier (BAB) is in general more permeable than blood-retina barrier (BRB), the specifics may depend on the compound used. For example, Toda et al. found that the permeability of low lipophilic compounds across the BAB is higher than across the BRB. Vice versa, however, the permeability of high lipophilic compounds across the BRB is higher than across the BAB (Toda et al, 2011). In this study, it was assumed that high lipophilic compound may not distribute in aqueous humor or be drained fast by aqueous flow (Toda et al, 2011). However, it does not rule out the possibility that there may be some signals in the anterior eye chamber.

Another interesting result of the experiments is the specific distribution of Cou6 in the retina parenchyma. Although the model drug penetrated fast and massively across the BRB, the same did not seem to be true for cellular membranes. There was no overlap regarding the staining of the nucleus and the Cou6 fluorescence, and the TOS matrix analysis also revealed minor overlapping regarding the signals from the retrograde RGC soma labelling and the fluorescent model drug (Figure 3.4 and Figure 3.5). The

spatial distribution rather suggested that there was no massive Cou6 labelling of the cell soma, and that Cou6 was rather associated with compounds of the extracellular space and axonal bundles. On day 7 post ONC, the spatial distribution of the Cou6 signal is increased (Figure 3.6) and at the same time the axon fiber staining is reduced, which may represent degeneration and reorganization processes of the tissue after neuronal death. Morphological distinction in the GCL appeared by day 7 post ONC also suggested the loss of connections between neighboring cells (Figure 3.6C). Therefore, development of the systems for drug delivery to the brain or retina requires consideration of not only the obstacles created by the barriers, such as the BRB or BBB, but also of the drug distribution in the parenchyma. Substances may, in fact, not accumulate in the sub-cellular target structure in which case there is no or only a diminished pharmacological effect.

To check if the kinetic of Cou6 or PLGA NPs is dependent on pathological condition, the ONC model was used as a pathology model. While one hour after optic nerve injury there were no detectable changes in permeability, a much faster decline of Cy5.5 fluorescence on day 7 post ONC in the retinal blood vessel was noted, even though Cou6 signal kinetic was similar to controls. This was rather surprising to us. The baseline fluorescence of retina post optic nerve crush group by day 7 under the Cy5.5 measurement were slightly declined (Figure S3), which may result from increased number of infiltrated cells in the vitreous and anterior chamber under pathological conditions (Kiseleva et al., 2019), and this may somehow influence the opacity resulting in different level of measured fluorescence signal as shown with *in vivo* imaging. Another possible explanation of reduced baseline fluorescence may be that other endogenous fluorophores in the retina, like NADPH or FAD (Dysli et al., 2017) may have partially disappeared when significant cell death has occurred 7 days after the lesion. In our opinion, however, the influence of changes in autofluorescence may be relatively small on the kinetic study, since the normalized signals were used in order to reduce the individual difference. Here are some possible explanations for the effect of ONC on NP clearing. According to Kiernan (Kiernan, 1985), the signal of a

fluorescent tracer was detected in the connective tissue of the orbit and the connective tissue trabeculae of the optic nerve, rather than in the retinal tissue. Therefore, it is possible that in this study abnormal permeability of these tissues after ONC caused the quicker clearance of NPs from retinal blood vessels. Another explanation could be that 7 days post ONC the NPs are degraded or removed faster from blood circulation. Indeed, after ONC an immune response is triggered within several days after the injury (Benhar et al., 2016), and it is possible that the emerging phagocytic cells (e.g. circulating monocytes) clear the NPs while reacting to cell death after optic nerve injury. In addition, there may be abnormal enzyme activity in the blood circulation after ONC which could accelerate the degradation of PLGA NPs. However, these are currently only working hypothesis and will need further investigations.

Moreover, both systemic route and intravitreal route are widely used for the treatment of eye diseases at the posterior eye segments. However, each of these two routes have pros and cons. For example, intravitreal injection can provide high concentrations of drugs in the vitreous and retina. Nevertheless, repetitive injections sometimes can cause adverse side effect for eye health (Raghava et al., 2004; Bisht et al., 2018). Systemic delivery can be repetitively administrated, but higher doses are needed, and side effects can affect other organs after accumulation of drugs in the liver and spleen (Figure 3.8). Therefore, carefully choosing the administration routes and balancing their pros and cons should be considered, based on the properties of drugs or drug delivery system.

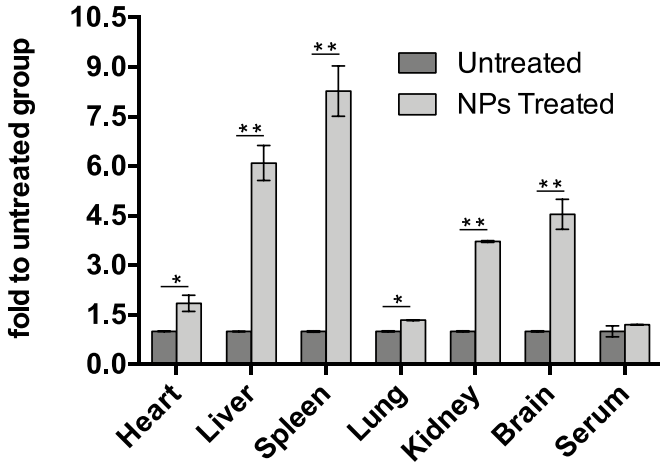

Figure 3.8 Determination of tissue biodistribution of Cou6 as cargoes encapsulated in PLGA NPs in *i.v.* injected rats.

The Cou6 fluorescence in heart, lung, liver, spleen, kidney, and brain post intravenous injection of PLGA-Cou6 NPs at 2 h were compared with that of untreated rats. (t-test, **P* < 0.05, ***P* < 0.01).

Based on these considerations, it can be concluded that PLGA NPs are useful to deliver poorly water-soluble compounds with potential pharmaceutical efficacy by intravenous injection which makes them attractive candidates for further drug development. They might help overcome the limitation of traditional formulation methods. But PLGA NPs are no magic bullet for drug delivery but need individual formulation tailored to the properties of the respective compounds.

3.5 Conclusion of Study II

PLGA NPs offer a "second opportunity" for the delivery of poorly water-soluble drugs *in vivo*. Instead of being discarded from further drug development due to the hydrophobic nature of such compounds, NPs could provide a suitable and systemically injectable delivery system. Moreover, the combination of two data sets, *in vivo* real-time monitoring and *ex vivo* microscopy of retina suggest that poorly water-soluble Cou6-like compounds could readily traverse the inner blood-retina barrier. This, in turn,

opens new perspectives for drug development for the treatment of eye disease and other neurodegenerative disorders of the brain.

4. Study III: Effect of Lipinski rule and polar surface area on the blood-retina barrier permeability of model drugs

4.1 Introduction to Study III

Treatment of the central nervous system (CNS) is always a challenge for neuropharmaceutical research. Many visual impairments are mainly caused by diseases of retina (part of CNS) in the posterior eye segment (Thrimawithana et al., 2011). Several neurodegeneration related CNS diseases are induced by intercellular perturbations such as dysfunctional crosstalk between neurons and other cells (Garden and La Spada, 2012). However, delivering the therapeutic drugs to the CNS has been a difficult task because 98% of molecules intended for therapeutic use in CNS cannot cross the blood-brain barrier (BBB) (Pardridge, 2007). The tight junctions between the endothelial cells are important molecular structures of the BBB and inner blood-retinal barrier (BRB), which are the physical barriers that seal the vascular lumen and prevent molecules from penetrating these barriers. Biodegradable nanoparticles (NPs) have been largely developed aiming at delivering therapeutic drugs specifically to diseased tissue.

In study II regarding the delivery of poorly water-soluble model drug Cou6 to the retina by Poly(lactic-co-glycolic acid) (PLGA) nanoparticles, I demonstrated with *in vivo* imaging that Cou6 can penetrate the inner BRB after being released from PLGA NPs . In addition, analyzing the biodistribution of Cou6 in organs also confirmed that it can penetrate the BBB. By looking deeply into the physicochemical properties, I assumed that the Cou6 might represent large amounts of drugs, whose molecular descriptors are in agreement with the Lipinski rules, enabling them to pass the BBB (Lipinski et al., 1997). These molecular descriptors include (i) number of hydrogen bound donors, (ii) number of hydrogen bound acceptors, too many of which will hinder permeability across a membrane bilayer (Abraham et al., 1994), (iii) molecular weight which is a rate limiting factor for BBB permeation (Kaliszan, 1996, , Kortagere et al., 2008), (iv)

number of rotatable bounds which are a deterrent for BBB permeation (Clark, 1999), and (v) logP which is one of hydropathic descriptors (Clark, 1999, Kortagere et al., 2008). Furthermore, the topological polar surface area (TPSA) was also considered in that it is another hydropathic descriptor that spans both the hydrophilic and hydrophobic nature of the bilayers (Kortagere et al., 2008).

In order to testify the effect of abovementioned molecular descriptors on the BBB and BRB penetration of Cou6 in more detailed way, I selected 162 chemical agents with known BBB permeability from a previous study (Li et al., 2005) in addition to the Cou6, and retrieved the value of corresponding descriptors from PubChem Database produced by National Center for Biotechnology Information (https://pubchem.ncbi.nlm.nih.gov). Furthermore, to better illustrate the BBB permeability of Cou6 as poorly water-soluble chemical and to better understand the influence of unique physicochemical properties of cargoes in drug delivery systems, I also studied another chemicals DiI as well as Rho123, which were investigated in the Study I, in the same way. Subsequently, datasets were classified using statistical learning method namely support vector machine (SVM). The SVM model was introduced for drug development, such as classification of toxicity effects of bio-transformed hepatic drugs (Tharwat et al., 2017) and the case studies of drug likeness, agrochemical likeness, and enzyme inhibition predictions (Xue et al., 2004). Subsequently, to visualize the classification results and show the category of Cou6, principal component analysis (PCA) was used for data preprocessing to be the inputs of the proposed SVM classification prediction models. PCA is an effective analysis method in reducing the dimensionality and fusing of relative features by evaluation of the cumulative contribution rate of each variable (Liu et al., 2016). Finally, I also compared the results with former *in vivo* studies. By doing so, my aim was to verify if the molecular descriptors of the Lipinski rule will match the BBB or BRB permeability of drugs similar to Cou6, DiI, or Rho123, after being released from NPs, which will further influence the design of nanoparticle drug delivery systems.

4.2 Methods of Study III

4.2.1 Dataset and molecular descriptors

In this work, a total of 162 agents with known BBB permeability (82 agents) and known non-BBB permeability (80 agents) from a previous study (Li et al., 2005), in addition to Cou6, DiI or Rho123 data were used as dataset. 80% of these agents were randomly chosen to be the training set and the other agents were used as testing set for conducting the cross validation. The topological polar surface area (TPSA) of agents and the descriptors mentioned in the Lipinski rule: hydrogen bound donors (HBD), hydrogen bound acceptors (HBA), molecular weight (MW), XLogP and rotatable bonds count (RBC) were used as simple molecular descriptors. These values of chemical and physical descriptors of the molecules were obtained from PubChem Database produced by National Center for Biotechnology Information (https://pubchem.ncbi.nlm.nih.gov, Kim et al., 2019). The dataset used for statistical learning is in the supplementary table of appendix. The description of Cou6 and DiI in Lipinski rule is shown in (Table 4.1)

Table 4.1 The values of Lipinski rule's descriptors and TPSA for Cou6, DiI and Rho123

Name	MW	XLogP	HBD	HBA	RBC	TPSA
Cou6	350.4	4.9	0	5	4	70.7
DiI	933.9	19	0	5	36	80.5
Rho123	380.8	1*(logP)	3	5	3	85.4

The values of corresponding chemical and physical descriptors of the molecules (Cou6 and DiI) in the table were obtained from PubChem Database produced by National Center for Biotechnology Information, 2020 (https://pubchem.ncbi.nlm.nih.gov, Kim et al., 2019). The values of corresponding chemical and physical descriptors of the molecules Rho123 in the table were obtained from PubChem Database produced by National Center for Biotechnology Information, 2021. *, Value that is not available in PubChem Database is from reference (Duvvuri et al., 2004).

4.2.2 Data preprocessing

Data preprocessing steps were adapted from a study by Liu et al. (Liu et al., 2016). The standardization of data in preprocessing is calculated as follows:

$$Standardized\ \ value = \frac{x_i - \overline{x_i}}{S_i}$$

where x_i is the data, $\overline{x_i}$ represent the mean value and S_i is standard deviation values in x_i respectively.

To visualize the final results for the statistical learning, the principal component analysis (PCA) was used, as it is an effective statistical analysis method in multidimensional data compression and feature extraction (Baldi et al., 2000; Crivori et al., 2000; Liu et al., 2016). It can reduce the dimension of the data and preserve as much of the data's variation as possible. The final output of PCA involved the coefficient matrix, score, and eigenvalues of the covariance matrix of data. Another matrix was then ranked according to cumulative contribution rate in descending order. In this study, the threshold of the cumulative contribution rate was set to 80%, so that if the cumulative contribution rate reached 80%, the corresponding top two principal components were selected to represent the original n dimensions.

4.2.3 Statistical learning method

The support vector machine (SVM) was selected in this study, since it was shown that the SVM seems to give a slightly higher prediction accuracy than other methods for predicting both BBB permeable agents and non-BBB permeable agents (Li et al., 2005). The type of validation partition Holdout was used for final visualization of testing and training results (Azam, 2020). The SVM in MATLAB implements a classification algorithm and provides three different kernel methods: a linear kernel, a polynomial kernel and a Gaussian kernel. In this work, the Gaussian kernel was selected (https://www.mathworks.com/help/stats/fitcsvm.html).

$$G(x_j, x_k) = \exp(-\|x_j - x_k\|^2)$$

where $G(x_j, x_k)$ is element (j, k) of the Gram matrix, x_j and x_k are p-dimensional vectors representing observations j and k.

4.2.4 Prediction Accuracy

Based on the previous study (Li et al., 2005), the performance of a statistical learning method can be evaluated by the quantity of true positives (TP), true negatives (TN), false positives (FP), and false negatives (FN). The accuracy, sensitivity, and precision of the SVM model was analyzed by confusionmatStats (Cheong, 2020) with following equations:

$$Accuracy = \frac{TP + TN}{TP + FP + FN + TN}$$

$$Precision = \frac{TP}{TP + FP}$$

$$Sensitivity = \frac{TP}{TP + FN}$$

4.3 Results of Study III

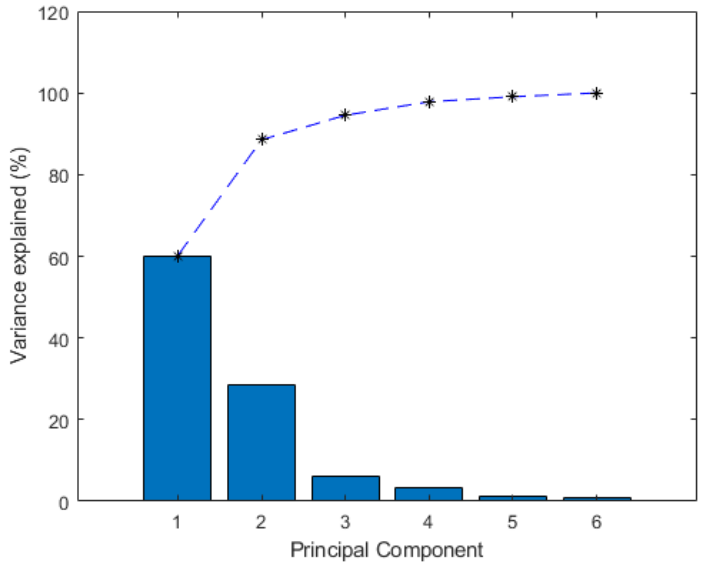

Figure 4.1 Variance extraction based on PCA.

The cumulative sum of variance versus the number of principle components was shown as curve in Figure 4.1, the threshold of the cumulative contribution rate was up to 86.58%. Therefore, the corresponding top 2 principal components were selected to represent the original 6 dimensions. The results in Table 4.2 showed the BBB permeable and BBB non-permeable prediction accuracies of proposed SVM classification with kernel function of Gaussian using PCA. It was found the overall accuracy was 80.63 % and the precision of BBB permeable agents' prediction (80.05 %) is comparable with BBB non-permeable precision with 81.85 %. In the study from Trotter et al., the BBB permeable accuracy (78.9%) is relatively higher than BBB non-permeable accuracy (60.4%) and the overall accuracy was 76% (Trotter et al., 2001). It seems the current model with Lipinski rules improved the accuracy to some extent. Furthermore, 5-fold cross validation could slightly improve the BBB permeable precision from 81.85% to 88.42% and the overall accuracy from 80.63% to the 84.20%.

Table 4.2 Predication accuracy of PCA + SVM classification

	5-fold cross validation		Hold-out	
	BBB+	BBB-	BBB+	BBB-
Accuracy (%)	84.20 (1.28)		80.63 (6.01)	
Precision (%)	80.96 (1.99)	88.42 (0.44)	80.05 (6.77)	81.85 (5.87)
Sensitivity (%)	89.99 (0.55)	78.25 (2.88)	84.13 (6.00)	76.66 (10.31)

BBB+: BBB permeable. BBB-: BBB nonpermeable. Values in parentheses are the standard deviations.

I randomly selected 80% agents as training group and 20% agents in addition to Cou6 or DiI as testing group. Both of the two groups were composed of one category of BBB permeable agents and another category of BBB non-permeable agents in the dataset. The classification visualization of the training results and the testing results for Cou6 and DiI is shown in Figure 4.2 and Figure 4.3, respectively. In line with my last *in vivo* study (Table 4.3), that the Cou6 can penetrate the BRB and BBB, it can be seen that

the Cou6 falls into the gray area (BBB permeable classification) predicted by the SVM with Gaussian kernel function (Figure 4.2). In contrast, the DiI is located out of the BBB permeable classification area (Figure 4.3). Figure 4.4 shows that the model drug Rho123 fell outside of the gray area, which is also in line with *in vivo* study (Table 4.3), therefore, this statistical learning suggested that the Lipinski rules and polar surface area can separate the BBB permeable compounds and BBB non-permeable compounds with good accuracy and can correctly classify Cou6 and DiI whose descriptors is in agreement with this rule as a BBB penetrating substance.

Figure 4.2 Visualization of SVM classification to evaluate Cou6.

Red circle: BBB-permeable agents. Green circle: non-BBB-permeable agents. Gray area: BBB-permeable area predicted by SVM model. Blue dot in testing results: Cou6 was labeled in blue in testing results.

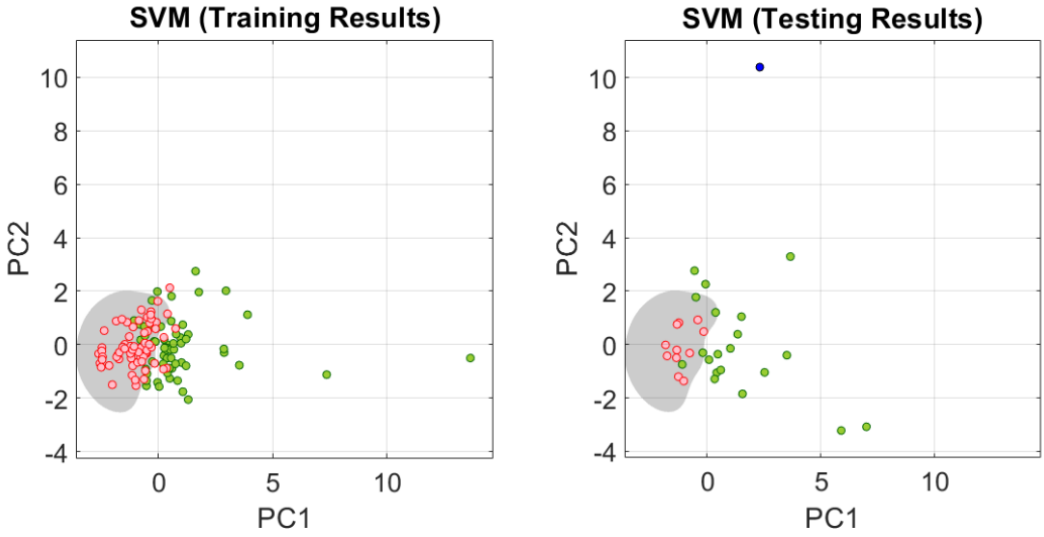

Figure 4.3 Visualization of SVM classification to evaluate DiI.

Red circle: BBB-permeable agents. Green circle: non-BBB-permeable agents. Gray area: BBB-permeable area predicted by SVM model. Blue dot in testing results: DiI was labeled in blue in testing results.

Figure 4.4 Visualization of SVM classification to evaluate Rho123.

Red circle: BBB-permeable agents. Green circle: non-BBB-permeable agents. Gray area: BBB-permeable area predicted by SVM model. Blue dot in testing results: Rho123 was labeled in blue in testing results.

Table 4.3 Comparison of *in vivo* results with classification results

	In vivo study (ICON)	Classification (SVM)
Cou6	BBB+	BBB+
DiI	BBB−	BBB−
Rho123	BBB−	BBB−

BBB+: BBB permeable. BBB-: BBB nonpermeable.

4.4 Discussion of Study III

The BBB in the brain and BRB in the retina can filter the passage of most compounds from bloodstream to tissue parenchyma by the tight junctions between the endothelial cells. A wide range of NPs have been investigated with the aim to allow a targeted administration to CNS and controlled drug delivery (Li and Sabliov, 2013). However, the interaction between the drugs released from the NPs during the blood circulation and the BBB and BRB are largely ignored. In my last two studies on the release kinetics of model drug Rho123 and DiI (Zhang et al., 2020), and poorly water-soluble model drug Cou6 in the retinal blood vessels, only Cou6 showed efficient BBB and BRB permeability after being released from PLGA NPs. This could be explained by the association of physicochemical properties of chemical agents with the BBB and BRB permeability, since such different properties can lead to the significant biological implications in the cellular uptake and biological processes, i.e. some molecules can be eliminated by active efflux transporters such as efflux transporters P-glycoprotein (Pgp) and multidrug resistance proteins (MRPs), whereas others can passively diffuse into the brain and retina by a transcellular route (Loscher and Potschka, 2005; Hitchcock and Pennington, 2006; Urquhart and Kim, 2009; Watanabe et al., 2012). Therefore, the

representative physicochemical properties of Cou6 were further analyzed to characterize the relationship of these properties with BBB and BRB permeability.

In this study, I used SVM classification method with Gaussian kernel function to distinguish the BBB permeable and BBB non-permeable chemical agents. The experiments demonstrated that overall accuracy of SVM with Hold-out is 80.63% on the 162 chemical agents and the SVM with 5-fold cross validation obtained 84.20% classification accuracy with slight improvement. This suggested that SVM with Lipinski rule's descriptors and PSA can be the suitable model to correlate the physicochemical properties of agents with BBB permeability at a comparable accuracy with respect to other classification methods using larger amount descriptors, for example, the overall accuracy of *k*-nearest neighbor with 199 descriptors is 77.0% (Li et al., 2005). The testing results of SVM in Figure 4.2 displayed that the poorly water-soluble model drug Cou6, whose value of molecular descriptor of Lipinski rules MW is 350.4, XLogP is 4.9, HBDC is 0, HBAC is 5, RBC is 4 and TPSA is 70.7, belongs to the BBB permeable category, which is consistent with the *in vivo* and *ex vivo* visual evidence of my study II, i.e the demonstration that the Cou6 can penetrate the BRB and BBB after being released from PLGA NPs. On the other hand, the DiI was not included into the BBB permeable category by the classification, which might be due to the large molecular weight and XlogP value, and 7-fold more rotatable bonds. Currently, the number of poorly water-soluble drug candidates increased sharply due to the repaid development in combinational chemistry and HTS. The low water solubility of drugs usually will result in the low bioavailability (Kumar et al., 2012). This study together with study II of my project suggests that the physicochemical properties of poorly water-soluble Cou6 like drug candidates, which are transported in nano-carrier formulations, can cross the BBB or BRB, even though they are released from the NPs in the blood circulation.

4.5 Conclusion of Study III

The present study demonstrated that SVM classification method could predict the permeability of chemical agents with relatively reliable accuracy. The molecular descriptors of potential drug candidates from Lipinski rule and PSA have a close relationship to their BBB or BRB permeability by the SVM assessment. A better understanding of the interactions between these physicochemical properties and BBB permeability will hopefully in turn lead to the efficient design of poorly water-soluble compounds delivery systems targeting the brain and retina. More representative features and more agents need to be further explored in order to improve the prediction accuracy.

5. General Discussion

5.1 Effect of blood flow on the kinetics of PLGA NPs

In the blood vessel, especially where the size of blood cells is comparable to the diameter of the capillary, the blood cells will exert a main effect on the blood flow, and subsequently on the NPs' kinetics in the blood circulation. As shown in Study I Figure 2.5C, 2.5E and 2.7A, the PLGA NPs were found between the blood cells and vessel wall in the small blood vessels after circulating for 2 h, which is consistent with the study from Fullstone et al. which showed that in case of a high percentage of RBCs, the NPs will be dispersed to the region near the blood vessel wall (Fullstone et al., 2015). This can be considered to be a beneficial effect since it will improve the retention between the NPs and endothelial cells of the blood vessel wall and provide the opportunity for PLGA NPs and/or their cargo to cross the BRB. In addition, the uneven diameter of blood vessels followed by different flow pattern might also have an effect on the distribution of NPs in the blood circulation. Taking Cy5.5-PLGA-Cou6 NPs as an example, as shown in Study II Figure 3.7, the distribution of PLGA NPs in the big retinal blood vessels (40~ 50 μm) looks like dots, which is different from the NPs in the small retinal blood vessels (<10 μm) showing relatively homogenous distribution.

The complex biological milieu of blood circulation increased the difficulty to predict the NPs' kinetics. Unlike the fluids of usual *in vitro* environment, such as PBS, the blood flow shows non-Newtonian behavior in the branches and capillaries (Ku, 1997). By comparing the *in vitro* release of DiI and Rho123 in the solution of 1% poloxamer 188 in 0.15 M PBS up to 24 h in Table 2.2 of Study I and *in vivo* kinetic of DiI and Rho123 from PLGA NPs in the Figure 2.6 and Figure 2.7, a quicker release of these model drugs from PLGA NPs in the retinal blood circulation can be found, especially Rho123, which diffused out of PLGA NPs and was eliminated within 30 min *in vivo*. Figure 3.1A in Study II also showed that 36.18% of Cou6 diffused out of PLGA NPs

in 1% HSA in 0.15 M PBS solution within 2 h, however, almost no Cou6 signal was found in PLGA NPs *in vivo* as shown in Figure 3.4.

Another important feature induced by the complex biological environment is the short life span of NPs in the blood stream, which is probably due to rapid clearing by phagocytic cells or reticuloendothelial system (RES) (Hans and Lowman, 2002). The surface modification is one way to design the NPs to avoid the capture of RES and phagocytic removal after the intravenous injection. To this end, poloxamer, polyoxyethylene-based block copolymer, has been largely used as surface modification materials for NPs. It has also low toxicity and immunogenic response (Moghimi et al., 2003; Liu et al., 2008) and can be absorbed on the particle surface by incubation due to the polarity of NPs such as PLA NPs (Redhead et al., 2001). In Study I, Figure 2.6 showed that PLGA NPs coated with poloxamer 188 and either with lipophilic model drug DiI or model drug Rho123 incorporated, are present in the retinal blood vessels up to 90 min, independent of the different diffusion rates of these model drugs out of the PLGA NPs. Although studies indicated that modification with poloxamer will increase the half lifetime of NPs (Kulkarni and Feng, 2013), it is difficult to predict whether the cargoes will be influenced in the same way, especially when the integrity of NPs and cargoes in the blood circulation and diffusion of drug out of the NPs during the circulations are considered. As it can be seen from the Study I Figure 2.4, the clearances of signal of model drug Rho123 in the blood circulation are not significantly changed in NPs which are coated with poloxamer 188 and NPs which are not.

5.2 Effect of pathological environment on the kinetics of PLGA NPs

In general, some eye diseases are related to a pathological retinal blood circulation which should be considered in the design of drug delivery systems. In the process of ischemic microangiopathies, when retinal neural tissue or endothelium are impaired, the metabolic pathways will consequently be influenced, resulting in the disturbed blood flow regulation (Pournaras, 2008). However, even though the vascular deficits have been well studied, the understanding of relationship between theses deficits and

pathophysiology of eye disease still remains quite limited (Pechauer et al., 2015). Figure 3.2 from Study II showed that PLGA NPs in the group post ONC by day 7 diminished more quickly than those in the non-ONC group and ONC-1h group. Nevertheless, by now it is still not clear if and how changed blood flow under pathological condition after optic nerve injury could influence the metabolism and circulation of these PLGA NPs. In addition, Joly et al. found that after retinae were injured by blue light, blood-borne macrophages will migrated to the site of retinal injury without breaking down BRB (Joly, 2009). It is conceivable that altered blood-borne components in the retinal blood vessel after injury might exert an influence on the circulation of PLGA NPs in the retinal blood vessels.

Another possible reason for the declined PLGA NPs signal could be the disturbance of the biological blood barrier such as inner BRB or blood-optic nerve barrier followed by the optic nerve injury. However, the optic nerve crush or transection might not directly influence the retinal blood vessels function, as the central retinal artery enters the optic nerve closely behind the optic nerve disc in rats (Kiernan, 1985) and the crush site was more than 1 mm behind the eyeball. In addition, the results in Study II also did not show an obviously increased PLGA NPs signal in the retinal tissue following the decreased PLGA NPs signal in the retinal blood vessels. Therefore, it seems unlikely that the barrier effect of retinal blood vessels on the PLGA NPs was compromised by the injury. Blood-optic nerve barrier is another subject which should be considered in optic nerve or optic nerve head vascular disorders, as in both structures tight cell junction between endothelial cells exist (Hayreh, 2011). The injured optic nerve in the mammalians has been used as model to study the Wallerian degeneration and blood-nerve barrier function (Kiernan, 1985). A study on the relationship between the barriers' function and the presence of intact axons indicate that the vascular integrity does not need the axons, but the Wallerian degeneration will influence the barrier function (Latker et al., 1991). Although the subject of the study was a peripheral nerve (a sciatic nerve), a similar effect can also occur on the blood-nerve barrier. In addition, optic

nerve crush may cause occlusion or stenosis of the posterior ciliary artery (Sugiyama et al., 1999).

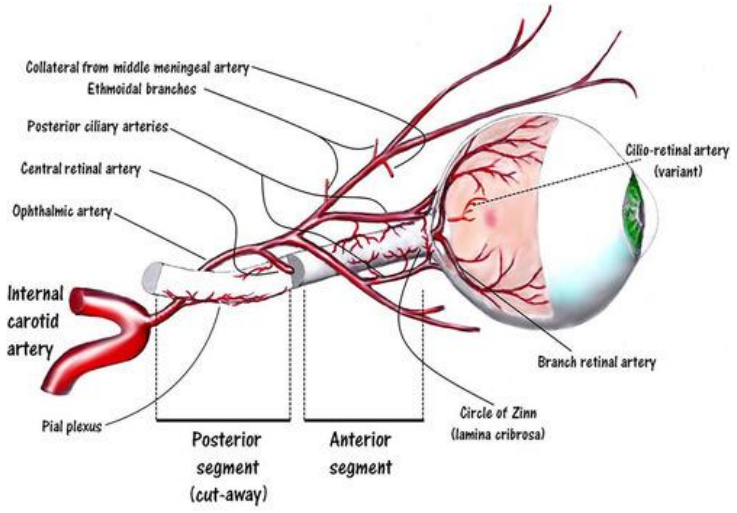

Figure 5.1 Medial to lateral view of the arterial supply to the optic nerve and retina.

Adapted from Grory et al. 2020.

In summary, the cause-effect relationships and mechanisms between the optic nerve injury and changed blood flow, altered blood components and declined number of NPs, or disturbed biological blood barrier and permeation of PLGA NPs in the retinal blood circulation still need to be elucidated *in vivo* in future studies.

5.3 Effect of physicochemical property of drug candidates on the kinetics of PLGA NPs

There is no doubt that the particle size, size distribution, surface charge, and surfactant are important factors for the NPs drug delivery system, because they influence the *in vivo* distribution, targeting delivery, accumulation, lifetime in the blood circulation, and toxicity of NPs in the body (Singh and Lillard Jr, 2009). Many studies have shown that the favorable size range for the systemic drug delivery is from 10 nm to 150 nm (Panyam and Labhasetwar, 2003; Kumar, 2012; Wang, 2008). In both Study I and Study II, all of the NPs utilized in the real-time kinetic study are around 130 nm (Table 2.1 and Table 3.1). However, the model drugs' distribution behaviors are different. As

shown in Figure 2.7, DiI was still incorporated in the PLGA NPs after the 2 h circulation and Rho123 had already been released out of the PLGA NPs and cleared. An individual behavior was also observed regarding the kinetics of PLGA NPs which encapsulated the poorly water-soluble model drug Cou6. In this case the model drug has already diffused out of the PLGA NPs, penetrated the BRB and distributed in the extracellular space and a little bit into the cytoplasm in less than 90 min (Figure 3.4). The drug release from NPs is affected by their size, as relatively large surface area of small NPs (compare to the microspheres) lead to the drug association on the NPs surface resulting in easy release from the NPs (Redhead et al., 2001). However, in case of the same range of size, the physicochemical properties of cargoes may also influence the kinetics of NPs as drug delivery system in the blood circulation. In addition, even though the PLGA NPs showed high drug loading capacity of DiI, Rho123, and Cou6 with more than 80% (Table 2.1 and Table 3.1), drug release in the blood circulation seems to be associated with entrapment efficiency according to their different physicochemical properties (molecular weight, functional groups, interaction between drugs and NPs etc.).

PLGA based nanoparticulate systems showed great potential for the retinal or brain drug delivery. Circumventing the BRB or BBB is a prerequisite for transporting drugs in order to efficiently exert therapeutic effects at the target area. To this end, most studies focused on the surface modification of NPs, for example, they are coated with surfactants (Tween 80), proteins (transferrin, ApoE), and peptides (angiopep-2), most of which are substrates of receptors presented in the brain and pass through BBB by endocytosis and transcytosis. However, the physicochemical properties of poorly-water soluble drug candidates which are associated with BBB permeability are largely ignored. Both Study I and Study II reflected that the drugs could– at least partly – be released from the PLGA NPs during the blood circulation, regardless of significant drug loading efficiency. For example, in the Study I, hydrophilic Rho123 diffused out of the PLGA NPs and cleared in the blood circulation very quickly, whereas lipophilic DiI still was to some extent incorporated in the PLGA NPs up to 2 h, and the free DiI diffused out of NPs stained the retinal blood vessel wall. In the Study II, the release of

poorly-water soluble Cou6 from PLGA NPs is even quicker than that of Rho123 in the retinal blood circulation, however, unlike the Rho123, the released Cou6 can penetrate the BRB very fast.

Therefore, in the case that the drug candidates released from NPs in the circulation per se permeate the BBB or BRB, but have extremely poor solubility in the physiological solvent such as saline or PBS for injection, improvement of solubility will be the priority in optimization of formulation in the drug design process. Moreover, optimization of drug candidates is as important as optimization of drug carriers in the drug design process and physicochemical properties of drugs should be carefully investigated. Lipinski's 'rule of five' has been used in various experiments to select the drug candidates in this respect. In the Study III, the SVM classification method was used to evaluate if the molecular descriptors described in the rule of five plus the descriptor TPSA can guide the drug candidates in free form released from the PLGA NPs. The result confirmed that Cou6 belong to the BBB permeation class. Therefore, it can be assumed that even if the drug candidates were quickly released from the PLGA NPs, they still have high chance to penetrate the BBB or BRB, if their physicochemical properties are still in conformity with this rule.

5.4 Extracellular/intercellular space as a path for retinal drug delivery

One possible way of molecular uptake is through intercellular spaces. Intraluminal injection of NPs into the intestine of anesthetized Beagle dogs found that NPs distributed in the intercellular space and in larger defects of mucosa between 10 and 15 min (Aprahamian et al., 1987). Dermal penetration of NPs (fullerene-substituted phenylalanine derivative of a nuclear localization peptide sequence) into the intercellular space of stratum granulosum in flexed skin was observed (Rouse et al., 2007). Lojk et al. demonstrated that delivery of NPs to the cancer urothelial cells and intercellular space is more than that to the normal urothelial cells, and the cell junctions are significantly less developed and intercellular space is larger in those invasive urothelial neoplasm tissue (Lojk et al., 2018). In addition, the extracellular matrix which

is composed of structural proteins and glycosaminoglycans providing the scaffold for cells and contributing to the signaling (Yue, 2014), is another interesting target for drug delivery. It is therefore necessary to know the possible and relevant interactions between extracellular matrix and NPs or their cargo (Engin, 2017). Here, the Study II reflected that although the poor water-soluble model drug Cou6 diffused out of the NPs at an early time, the signal of Cou6 was largely found in the cell surface and extracellular space of GCL and only partially in the cytoplasm of RGCs. It was also found that the extracellular space illustrated by the Cou6 in the retina of ONC-7d group was larger as compared to the other two groups, i.e. control and ONC-1h group (Figure 3.6). Extracellular or intercellular space is important for diffusion of particular substance to the cells in the retina; hence it is essential for retinal nutrition and the pathological condition might be associated with the change of the intercellular space (Cunha-Vaz, 2017). For example, some scientists found that the intercellular space was increased, the cell number was declined in the GCL and the inner nuclear layer was thinner in the diabetic rats (Li et al., 2014). In summary, extracellular or intercellular space opens a new way for the drug delivery into the CNS, and more research in this field may be beneficial for drug development.

6. General Conclusions and Outlook

PLGA NPs are a potential drug delivery system which can enclose different drugs and has good biocompatibility and biodegradability. However, the integrity of PLGA NPs with cargoes has not been studied much so far, because more attention was paid to the modification of PLGA NPs. This study showed that the lipophilic and hydrophilic model drugs are released from PLGA NPs during the circulation in the retinal blood vessels. This release also showed different kinetics of PLGA drug delivery systems under the real-life conditions, as Rho123 released more quickly than DiI from PLGA NPs, and the released Rho123 was eliminated during the circulation, but the released DiI stained the retinal blood vessel wall. Regarding the aspect of delivering poorly water-soluble model drug Cou6, PLGA NPs had the ability to convert the poorly soluble drug into deliverable and injectable drug formulation. When the poorly water-soluble model drug Cou6 released from PLGA NPs during the circulation, the special physicochemical properties enabled the model drug to permeate the inner BRB whereas PLGA NPs still circulated in the retinal blood vessels. Under the pathological condition of ONC-7d, the clearance of PLGA NPs is faster than under the normal condition. *Ex vivo* whole mount found that the model drug Cou6 mostly concentrated in the extracellular space of the retina and partially distributed in the cytoplasm. Using the SVM model and chemicals with known permeability of BBB, the results in the study III showed that the Cou6 with its simple molecular structure descriptors can penetrate the BRB and BBB.

The future studies for retinal drug delivery should also consider the following points.

(I) Although *in vivo* monitoring and *ex vivo* retinal whole mount are good methods to evaluate the nano-bio or cargo-bio interactions in the retina, a method aiming to detect these interactions between the drug candidates which doesn’t rely on fluorescence should be developed.

(II) The PLGA NPs drug delivery system should be individually tailored regarding the transportation across BBB or BRB, since the physicochemical properties of drug candidates can influence the ability to pass through the BBB or BRB, and in this case, labour intensive and costly surface modification can be diminished.

(III) How the pathological condition is related with changed blood flow is still not clear. And if this blood flow change will further impact the kinetics of PLGA NPs should be also studied in the future as well as the influence to alter the extracellular space's on the drug distribution.

(IV) In order to more efficiently screen the BBB or BRB permeable drug candidates, more accurate and effective chemical or physical features should be explored and extracted. By doing so, the accuracy of statistical learning method can be improved to a high level and drug delivery system will benefit from it.

In general, pharmaceuticals science in the area of CNS disease treatment is now developing into a field in which chemists and chemical engineers are expected to discover novel and biodegradable materials, biologists to know about the potential mechanisms, kinetics and the pathways by which they interact with body, and the computer scientists to develop the algorithms and screen the chemical features to improve the drug development efficiency.

7. References

Abraham, M.H., Chadha, S.H., Whiting, G.S., Mitchell, R.C., (1994). Hydrogen bonding. 32. An analysis of water-octanol and water-alkane partitioning and the delta log P parumeter of Seiler. J. Pharm. Sci. 83, 1085–l100.

Albumedix Ltd.. The Use of Albumin in Formulations. News-Medical. https://www.news-medical.net/whitepaper/20190117/The-Use-of-Albumin-in-Formulations.aspx (Retrieved on November 09, 2020).

Alexis, F., Pridgen, E., Molnar, L., Farokhzad, O, (2008). Factors affecting the clearance and biodistribution of polymeric nanoparticles. Mol. Pharmaceutics 5, 505–515.

Almada, P., Pereira, P.M., Culley, S., Caillol, G., Boroni-Rueda, F., Dix, C.L., Charras, G., Baum, B., Laine, R.F., Leterrier, C., Henriques, R., (2019). Automating multimodal microscopy with NanoJ-Fluidics. Nat. Commun. 10(1), 1223.

Anand-Apte, B., Hollyfield, J.G., (2010). Developmental anatomy of the retinal and choroidal vasculature. Encycl. Eye. 9–15.

Andreeva, K., Soliman, M.M., Cooper, N.G., (2015). Regulatory networks in retinal ischemia-reperfusion injury. BMC Genet. 16, 43.

Aprahamian, M., Michel, C., Humbert, W., Devissaguet, J.-P., Damgr, C., (1987). Transmucosal passage of polyalkylcyanoacrylate nanocapsules as a new drug carrier in the small intestine. Biol. Cell 61, 69-76.

Aston, R., Cullumbine, H., (1959). Studies on the nature of the joint action of ethanol and barbiturates. Toxicology 1, 65–72.

Azam, Nouman. (2020). "Matlab Master Class: Go from Begginer to expert in Matlab", online, available by https://www.udemy.com/course/matlab-essentials-for-engineering-and-science-students/

Baldi, P., Brunak, S., Chauvin, Y., Andersen, C.A., Nielsen, H., (2000). Assessing the accuracy of prediction algorithms for classification: an overview. Bioinformatics 16 (5), 412–424.

Barichello, J.M., Morishita, M., Takayama, K., Nagai, T., (1999). Encapsulation of hydrophilic and lipophilic drugs in PLGA nanoparticles by the nanoprecipitation method. Drug Dev. Ind. Pharm. 25 (4), 471–476.

Barral, J.-P., Croibier, A., (2011). 2-Circulatory physiology. Visceral Vascular Manipulations. Churchill Livingstone. 27-45.

Bata, A.M., Fondi, K., Witkowska, K.J., Werkmeister, R.M., Hommer, A., Vass, C., Resch, H., Schmidl, D., Popa-Cherecheanu, A., Chua, J., Garhöfer, G., Schmetterer, L., (2019). Optic nerve head blood flow regulation during changes in arterial blood pressure in patients with primary open-angle glaucoma. Acta Ophthalmol. 97(1), e36–e41.

Benhar, I., Reemst, K., Kalchenko, V., Schwartz, M., (2016). The retinal pigment epithelium as a gateway for monocyte trafficking into the eye. EMBO J. 35, 1219–1235.

Bien, A., Seidenbecher, T.C., Böckers, I.M., Sabel, B.A., Kreut, M.R., (1999). Apoptotic versus necrotic characteristics of retinal ganglion cell death after partial optic nerve injury. J. Neurotraum. 16 (2), 153–163.

Bisht, R., Mandal, A., Jaiswal, J.K., Rupenthal, I.D., (2018). Nanocarrier mediated retinal drug delivery: overcoming ocular barriers to treat posterior eye diseases. WIREs Nanomed. Nanobiotechnol. 10, e1473.

Booysen, L.L.I.J., Kalombo, L., Brooks, E., Hansen, R., Gilliland, J., Gruppo, V., Lungenhofer, P., Semete-Makokotlela, B., Swai, H.S., Kotze, A.F., Lenaerts, A., du Plessis, L.H., (2013). *In vivo/in vitro* pharmacokinetic and pharmacodynamic study of spray-dried poly-(dl-lactic-co-glycolic) acid nanoparticles encapsulating rifampicin and isoniazid. Int. J. Pharm. 444 (1-2), 10–17.

Bobo, D., Robinson, K.J., Islam, J., Thurecht, K.J., Corrie, S.R., (2016). Nanoparticle-based medicines: A review of FDA-approved materials and clinical trials to date. Pharm. Res. 33, 2373–2387.

Broadwell, R.D., Salcman, M., Kaplan, R.S., (1982). Morphologic effect of dimethyl sulfoxide on the blood-brain barrier. Science 217(4555), 164–166.

Budhian, A., Siegel, S.J., Winey, K.I., (2008). Controlling the *in vitro* release profiles for a system of haloperidol-loaded PLGA nanoparticles. Int. J. Pharm. 346, 151–159.

Caro, C.G., Pedley, T.J., Schroter, R.C., Seed, W.A., (1978). The Mechanics of the circulation. New York: Oxford Medical.

Castro, D.J., Saxton, R.E., Rodgerson, D.O., Fu, Y.S., Bhuta, S.M., Fetterman, H.R., Castro CST, D.J., Tartell, P.B., Ward, P.H., (1989). Rhodamine-123 as a new laser dye: *In vivo* study of dye effects on murine metabolism, histology and ultrastructure. Laryngoscope. 99 (10), 1057–1062.

Cedervall, T., Lynch, I. , Foy, M., Berggård, T., Donnelly, S.C., Cagney, G., Linse, S., Dawson, K.A., (2007a). Detailed identification of plasma proteins adsorbed on copolymer nanoparticles. Angew. Chem. Int. Ed. 46, 5754–5756.

Cedervall, T., Lynch, I., Lindman, S., Berggård, T., Thulin, E., Nilsson, H., Dawson, K.A., Linse, S., (2007b). Understanding the nanoparticle–protein corona using methods to quantify exchange rates and affinities of proteins for nanoparticles. Proc. Natl. Acad. Sci. 104, 2050–2055.

Chang, J., Jallouli, Y., Kroubi, M., Yuan, X., Feng, W., Kang, C., Pu, P., Betbeder, D., (2009). Characterization of endocytosis of transferrin-coated PLGA nanoparticles by the blood-brain barrier. Int. J. Pharm. 379, 285–292.

Chen, H., Weber, A.J., (2001). BDNF enhances retinal ganglion cell survival in cats with optic nerve damage. Invest. Ophthalmol. Vis. Sci. 42, 966–974.

Cheong, A., (2020). confusionmatStats (group, grouphat), MATLAB Central File Exchange. Retrieved August 31, 2020. (https://www.mathworks.com /matlabcentral/fileexchange/46035-confusionmatstats-group-grouphat)

Choi, J., Seo, K., Yoo, J., (2012). Recent advances in PLGA particulate systems for drug delivery. J. Pharm. Investig. 42, 155–163.

Cirovic, S., Bhola, R.M., Hose, D.R., Howard, I.C., Lawford, P.V., Marr, J.E., Parsons**,** M.A., (2006). Computer modelling study of the mechanism of optic nerve injury in blunt trauma. Br. J. Ophthalmol. 90, 778–783.

Clark, D.E., (1999). Rapid calculation of polar molecular surface area and its application to the prediction of transport phenomena. 2. Prediction of blood–brain barrier penetration. J. Pharm. Sci. 88, 815–821.

Cohen, A., Bray, G.M., Aguayo, A.J., (1994). Neurotrophin-4/5 (NT-4/5) increases adult rat retinal ganglion cell survival and neurite outgrowth *in vitro*. J. Neurobiol. 25, 953–959.

Crivori, P., Cruciani, G., Carrupt, P.A., Testa, B., (2000). Predicting blood-brain barrier permeation from three-dimensional molecular structure. J. Med. Chem. 43, (11), 2204–2216.

Cui, Q., Yin, Y., Benowitz, L.I., (2009). The role of macrophages in optic nerve regeneration. Neuroscience 158(3), 1039–1048.

Cunha-Vaz, J.G., (2004). The blood–retinal barriers system. Basic concepts and clinical evaluation. Exp. Eye Res. 78, 715–721.

Cunha-Vaz, J., (2017). The blood-retinal barrier in the management of retinal disease: EURETINA Award Lecture. Ophthalmologica 237, 1–10.

Cunha-Vaz, J.G., (1976). The blood-retinal barriers. Doc. Ophthalmol. 41(2), 287–327.

Daly, S.M., Leahy, M.J., (2013). 'Go with the flow': A review of methods and advancements in blood flow imaging. J. Biophotonics 6, 217–255.

Danesh-Meyer, H.V., Zhang, J., Acosta, M.L., Rupenthal, I.D., Green, C.R., (2015). Connexin43 in retinal injury and disease. Prog. Retin. Eye Res. 51, 41–68.

Danhier, F., Ansorena, E., Silva, J.M., Coco, R., Breton, A.L., Préat, V., (2012). PLGA-based nanoparticles: an overview of biomedical application. J. Control. Release 161 (2), 505–522.

Davis, M.E., (2008). Nanoparticle therapeutics: an emerging treatment modality for cancer. Nat. Rev. Drug Discov. 7, 771e82.

Desai, M.P., Labhasetwar, V., Walter, E., Levy., R.J., Amidon, G.L., (1997). The mechanism of uptake of biodegradable microparticles in Caco-2 cells is size dependent. Pharm. Res. 14, 1568–1573.

Díaz-Coránguez, M., Ramos, C., Antonetti, D.A., (2017). The inner blood-retinal barrier: Cellular basis and development. Vision Res. 139, 123–137.

Diebold, Y., Calonge, M., (2010). Applications of nanoparticles in ophthalmology. Prog. Retin. Eye Res. 29 (6), 596–609.

Doerge, D.R., Twaddle, N.C., Vanlandingham, M., Fisher, J.W., (2010). Pharmacokinet-ics of bisphenol A in neonatal and adult Sprague-Dawley rats. Toxicol. Appl. Pharmacol. 247 (2), 158–165.

Dowling, J.E., (1987). The retina: an approachable part of the brain. Belknap, Cambridge.

Duncan, R., (2005). Nanomedicine gets clinical. Mater. Today 8 (8), 16–17

Duvvuri, M., Gong, Y., Chatterji, D., Krise, J.P., (2004). Weak base permeability characteristics influence the intracellular sequestration site in the multidrug-resistant human leukemic cell line HL-60. J. Biol.Chem., 279, 32367–32372.

Dysli, C., Wolf, S., Berezin, M.Y., Sauer, L., Hammer, M., Zinkernagel, M.S., (2017). Fluorescence lifetime imaging ophthalmoscopy. Prog Retin. Eye Res. 60, 120–143.

Eltzschig, H.K., Eckle, T., (2011). Ischemia and reperfusion–from mechanism to translation. Nat. Med. 17, 1391–1401.

Engelhardt, B., Coisne, C., (2011). Fluids and barriers of the CNS establish immune privilege by confining immune surveillance to a two-walled castle moat surrounding the CNS castle. Fluids Barriers CNS. 8, 4.

Engin, A.B., Nikitovic, D., Neagu, M., Henrich-Noack, P., Docea, A.O., Shtilman, M.I., Golokhvast, K., Tsatsakis, A.M. (2017). Mechanistic understanding of nanoparticles' interactions with extracellular matrix: the cell and immune system. Part. Fibre. Toxicol. 14(1), 22.

Ertl, P., Rohde, B., Selzer, P., (2000). Fast calculation of molecular polar surface area as a sum of fragment-based contributions and its application to the prediction of drug transport Properties. J. Med. Chem. 43, 3714–3717.

Farshbaf, M., Davaran, S., Zarebkohan, A., Annabi, N., Akbarzadeh, A., Salehi, R., (2018). Significant role of cationic polymers in drug delivery systems. Artif. Cells Nanomed. Biotechnol. 46 (8), 1872–1891.

Fesce, R., Grohovaz, F., Valtorta, F., Meldolesi, J., (1994). Neurotransmitter release: fusion or 'kiss-and-run'? Trends Cell Biol. 4 (1), 1–4.

Fernandes, T.B., Segretti, M.C.F., Polli, M.C., and Parise-Filho, R., (2016). Analysis of the applicability and use of Lipinski's rule for central nervous system drugs. Lett. Drug Des. Discov. 13, 999.

Findl, O., Strenn, K., Woltz, M., Menapace, R., Vass, C., Eichler, H.G., and Schmetterer, L., (1997). Effects of changes in intraocular pressure on human ocular haemodynamics. Curr. Eye Res. 16, 1024–1029.

Flammer, J., Konieczka, K., (2017). The discovery of the Flammer syndrome: a historical and personal perspective. EPMA J. 8(2), 75–97.

Fonseca, C., Simoes, S., Gaspar, R., (2002). Paclitaxel-loaded PLGA nanoparticles: preparation, physicochemical characterization and *in vitro* anti-tumoral activity. J. Control. Release 83, 273–286.

Franke, H., Galla, H.-J., Beuckmann, C.T., (1999). An improved low-permeability in vitro-model of the blood–brain barrier: transport studies on retinoids, sucrose, haloperidol, caffeine and mannitol. Brain Res. 818 (1), 65–71.

Fresta, C.G., Fidilio, A., Caruso, G., Caraci, F., Giblin, F.J., Marco Leggio, G., Salomone, S., Drago, F., Bucolo, C., (2020). A new human blood–retinal barrier model based on endothelial cells, pericytes, and astrocytes. Int. J. Mol. Sci. 21, 1636.

Fujii, S., Setoguchi, C., Kawazu, K., Hosoya, K., (2014). Impact of P-glycoprotein on blood–retinal barrier permeability: Comparison of blood–aqueous humor and blood–brain barrier using *Mdr1a* knockout rats. Investig. Ophthalmol. Vis. Sci. 2014, 4650–4658.

Fullstone, G., Wood, J., Holcombe, M., Battaglia, G., (2015). Modelling the transport of nanoparticles under blood flow using an agent-based approach. Sci. Rep. 5, 10649.

Galla, H.-J., (2018). Monocultures of primary porcine brain capillary endothelial cells: Still a functional *in vitro* model for the blood-brain-barrier. J. Control. Release 285, 172–177.

Galvao, J., Davis, B., Tilley, M., Normando, E., Duchen, M.R., Cordeiro, M.F., (2014). Unexpected low-dose toxicity of the universal solvent DMSO. FASEB J. 28(3), 1317–1330.

Garcia Jr., J. P.S., Garcia, P.T., Rosen, R.B., (2002). Retinal blood flow in the normal human eye using the Canon laser blood flowmeter. Ophthalmic. Res. 4, 295–299.

Garden, G.A., La Spada, A.R., (2012). Intercellular (Mis)communication in Neurodegenerative Disease. Neuron 73, 886–901.

Geldenhuys, W.J., Mohammad, A.S., Adkins, C.E., Lockman, P.R., (2015). Molecular determinants of blood–brain barrier permeation. Ther. Deliv. 6(7), 961–971.

Gelperina, S., Maksimenko, O., Khalansky, A., Vanchugova, L., Shipulo, E., Abbasova, K., Berdiev, R., Wohlfart, S., Chepurnova, N., Kreuter, J., (2010). Drug delivery to the brain using surfactant-coated poly(lactide-co-glycolide) nanoparticles: Influence of the formulation parameters. Eur. J. Pharm. Biopharm. 74 (2), 157–163.

Gessner, A., Lieske, A., Paulke, B.R., Müller, R.H., (2002). Influence of surface charge density on protein adsorption on polymeric nanoparticles: analysis by two-dimensional electrophoresis. Eur. J. Pharm. Biopharm. 54, 165–170.

Gomez-Garcia, M.J., Doiron, A.L., Steele, R.R.M., Labouta, H.I., Vafadar, B., Shepherd, R.D., Gates, I.D., Cramb, D.T., Childs, S.J., K.D., Rinker, (2018). Nanoparticle localization in blood vessels: dependence on fluid shear stress, flow disturbances, and flow-induced changes in endothelial physiology. Nanoscale 10, 15249–15261

Green, R., Davies, M., Roberts, C., Tendler, S.B. (1999). Competitive protein adsorption as observed by surface plasmon resonance. Biomaterials 20, 385–391.

Greene, C., Campbell, M., (2016). Tight junction modulation of the blood brain barrier: CNS delivery of small molecules. Tissue Barriers 4(1), e1138017.

Grory, B.M., Lavin, P., Kirshner, H. Schrag, M, (2020). Thrombolytic therapy for acute central retinal artery occlusion. Stroke 51(2), 687–695

Grunwald, J.E., Piltz, J., Hariprasad, S.M., DuPont, J., (1998). Optic nerve and choroidal circulation in glaucoma. Invest. Ophthalmol. Vis. Sci. 39, 2329–2336.

Guy, W.M., Soparkar, C.N.S., Alford, E.L., Patrinely, J.R., Sami, M.S., Parke, R.B., (2014). Traumatic optic neuropathy and second optic nerve injuries. JAMA Ophthalmol. 132(5), 567–571.

Hans, M.L., Lowman, A.M., (2002). Biodegradable nano- particles for drug delivery and targeting. Curr. Opin. Solid State Mater. Sci. 6(4), 319–327.

Harju, M., Vesti, E., (2001). Blood flow of the optic nerve head and peripapillary retina in exfoliation syndrome with unilateral glaucoma or ocular hypertension. Graefes. Arch. Clin. Exp. Ophthalmol. 239(4), 271–277.

Hayreh, S.S., (2011). Blood-Optic Nerve Barrier. In: Ischemic Optic Neuropathies. Springer, Berlin, Heidelberg.

He, C., Hu, Y., Yin, L., Tang, C., Yin, C., (2010). Effects of particle size and surface charge on cellular uptake and biodistribution of polymeric nanoparticles. Biomaterials. 31 (13), 3657–3666.

Henrich-Noack, P., Voigt, N., Prilloff, S., Fedorov, A., Sabel, B.A., (2013). Transcorneal electrical stimulation alters morphology and survival of retinal ganglion cells after optic nerve damage. Neurosci. Lett. 543, 1–6.

Hitchcock, S.A., Pennington, L.D., (2006). Structure-brain exposure relationships. J. Med. Chem. 49(26), 7559–7583.

Hofmann, D., Messerschmidt, C., Bannwarth, M., Landfester, K., Mailander, V., (2014). Drug delivery without nanoparticle uptake: delivery by a kiss-and-run mechanism on the cell membrane. Chem. Commun. 50, 1369–1371.

Holmes, D, (2018). Reconstructing the retina. Nature. 561(7721), S2-S3.

Holmkvist, A.D., Friberg, A., Nilsson, U.J., Schouenborg, J., (2016). Hydrophobic ion pairing of a minocycline/Ca^{2+}/AOT complex for preparation of drug-loaded PLGA nanoparticles with improved sustained release. Int. J. Pharm. 499, 351–357.

Hosoya, K., Yamamoto, A., Akanuma, S., Tachikawa. M., (2010). Lipophilicity and transporter influence on blood-retinal barrier permeability: A Comparison with blood-brain barrier permeability. Pharm. Res. 27, 2715–2724.

Hosoya, K., Tomi, M., Tachikawa, M., (2011). Strategies for therapy of retinal diseases using systemic drug delivery: relevance of transporters at the blood-retinal barrier. Expert Opin. Drug Deliv. 8 (12), 1571–1587.

Hsieh, H.J., Liu, C.A., Huang, B., Tseng, A.H.H., Wang, D.L., (2014). Shear-induced endothelial mechanotransduction: the interplay between reactive oxygen species (ROS) and nitric oxide (NO) and the pathophysiological implications. J. Biomed. Sci. 21, 3.

Hurst, S., Loi, C., Brodfuehrer, J., El-Kattan, A., (2007). Impact of physiological, physicochemical and biopharmaceutical factors in absorption and metabolism mechanisms on the drug oral bioavailability of rats and humans. Expert Opin. Drug Metab. Toxicol. 3, 469–489.

http://products.invitrogen.com/ivgn/product/D282

Inokuchi, Y., Hironaka, K., Fujisawa, T., Tozuka, Y., Tsuruma, K., Shimazawa, M., Takeuchi, H., Hara, H., (2010). Physicochemical properties affecting retinal drug/Coumarin-6 delivery from nanocarrier systems via eyedrop administration. Investig. Ophthalmol. Vis. Sci. 51, 3162–3170.

Irsch, K., Guyton, D.L., (2009). Anatomy of eyes. In: Li S.Z., Jain A. (eds) Encyclopedia of Biometrics. Springer, Boston, MA.

Jain, R.A., (2000). The manufacturing techniques of various drug loaded biodegradable poly(lactide-co-glycolide) (PLGA) devices. Biomaterials 21, 2475–2490.

Jain, D., Athawale, R., Bajaj, A., Shrikhande, S., Goel, P.N., Gude., R.P., (2013). Studies on stabilization mechanism and stealth effect of poloxamer 188 onto PLGA nanoparticles. Colloids Surf. B. 109, 59–67.

Jamshidi, R., Mazzei, L., (2018). CFD modeling of fluidized beds. Reference module in Chemistry. Molecular Sciences and Chemical Engineering, 1–15.

Ji, H.M., Samper, V., Chen, Y., Heng, C.K., Lim, T.M., Yobas, L., (2008). Silicon-based microfilters for whole blood cell separation. Biomed. Microdevices 10(2), 251–7.

Joly, S., Francke, M., Ulbricht, E., Beck, S., Seeliger, M., Hirrlinger, P., Hirrlinger, J., Lang, K.S., Zinkernagel, M., Odermatt, B., Samardzija, M., Reichenbach, A., Grimm, C., Remé, C.E., (2009). Cooperative phagocytes: resident microglia and bone marrow immigrants remove dead photoreceptors in retinal lesions. Am. J. Pathol. 174 (6), 2310–2323.

Kalaria, D.R., Sharma, G., Beniwal, V., Ravi Kumar, M.N.V., (2009). Design of biodegradable nanoparticles for oral delivery of Doxorubicin: *in vivo* pharmacokinetics and toxicity studies in rats. Pharm. Res. 26 (3), 492–501.

Kaliszan, R.M.M., (1996). Brain/blood distribution described by a combination of partition coefficient and molecular mass. Int. J. Pharm. 145, 8.

Karande, S., Khalsa, A., Kelgaonkar, A., (2020). Central retinal artery occlusion: a manifestation of blunt trauma. BMJ Case Rep. 13 (8), e235632.

Kelder, J., Grootenhuis, P., Bayada, D., Delbressine, M.L., Ploemen, J., (1999). Polar molecular surface as a dominating determinant for oral absorption and brain penetration of drugs. Pharm. Res. 16 (10), 1514–1519.

Khalin, I., Heimburger, D., Melnychuk, N., Collot, M., Groschup, B., Hellal, F., Reisch, A., Plesnila, N., Klymchenko, A.S., (2020). Ultrabright fluorescent polymeric nanoparticles with a stealth pluronic shell for live tracking in the mouse brain. ACS Nano 14, 9755−9770.

Kiernan, J.A., (1985). Axonal and vascular changes following injury to the rat's optic nerve. J. Anat. 141, 139–154.

Kim, S., Chen, J., Cheng, T., Gindulyte, A., He, J., He, S., Li, Q., Shoemaker, B.A., Thiessen, P.A., Yu, B., Zaslavsky, L., Zhang, J., Bolton, E.E., 2019. PubChem 2019 update: improved access to chemical data. Nucleic Acids Res. 47(D1), D1102-D1109.

Kiseleva, T.N., Chudin, A.V., Khoroshilova-Maslova, I.P., (2019). Morphological changes in the retina under conditions of experimental in vivo regional

ischemia/reperfusion. Bull. Exp. Biol. Med. 167, 287–292.

Kontush, A., Lindahl, M., Lhomme, M., Calabresi, L., Chapman, M.J., Davidson, W.S., (2015). Structure of HDL: particle subclasses and molecular components. Handb. Exp. Pharmacol. 224, 3–51.

Kortagere, S., Chekmarev, D., Welsh, W.J., Ekins, S., (2008). New predictive models for blood–brain barrier permeability of drug-like molecules. Pharm. Res. 25(8), 1836–1845.

Kostyk, S.K., D'Amore, P.A., Herman, I.M., Wagner, J.A., (1994). Optic nerve injury alters basic fibroblast growth factor localization in the retina and optic tract. J. Neurosci. 74 (3), 1441–l 449.

Ku, D.N., (1997). Blood flow in arteries. Annu. Rev. Fluid Mech. 29, 399–434.

Kubo, Y., Tsuchiyama, A., Shimizu, Y., Akanuma, S., Hosoya, K., (2014). Involvement of carrier-mediated transport in the retinal uptake of clonidine at the inner blood-retinal barrier. Mol. Pharmaceutics 11, 3747–3753.

Kulkarni, S.A., Feng, S., (2013). Effects of particle size and surface modification on cellular uptake and biodistribution of polymeric nanoparticles for drug delivery. Pharm. Res. 30, 2512–2522.

Kumar, S., Dilbaghi, N., Saharan, R., Bhanjana, G., (2012). Nanotechnology as emerging tool for enhancing solubility of poorly water-soluble drugs. BioNanoSci. 2, 227–250.

LaNasa, P.J., Upp, E.L., (2014). 2-Basic Flow Measurement Laws. Fluid Flow Measurement (Third Edition). Butterworth-Heinemann, 19-29.

Latker, C.H., Wadhwani, K.C., Balbo, A., Rapoport, S.I., (1991). Blood-nerve barrier in the frog during wallerian degeneration: Are axons necessary for maintenance of barrier function? J. Comp. Neurol. 308, 650–664.

Li, H., Yap, C.W., Ung, C.Y., Xue, Y., Cao, Z.W., Chen, Y.Z., (2005). Effect of selection of molecular descriptors on the prediction of blood−brain barrier penetrating and nonpenetrating agents by statistical learning methods. J. Chem. Inf. Model. 45 (5), 1376–1384.

Li, X., Zhang, M., Zhou, H., (2014). The morphological features and mitochondrial oxidative stress mechanism of the retinal neurons apoptosis in early diabetic rats. J. Diabetes Res. 2014, 1–8.

Li, Y., Song, Y., Zhao, L., Gaidosh, G., Laties, A.M., Wen, R., (2008). Direct labeling and visualization of blood vessels with lipophilic carbocyanine dye DiI. Nat. Protoc. 3, 1703–1708.

Liang, H., Yang, T., Huang, C., Chen, M., Sung, H., (2005). Preparation of nanoparticles composed of poly(g-glutamic acid)-poly(lactide) block copolymers and evaluation of their uptake by HepG2 cells. J. Control. Release 105, 213–225.

Lipinski, C., Lombardo, F., Dominy, B., Feeney, P.J., (1997). Experimental and computational approaches to estimate solubility and permeability in drug discovery and development settings. Adv. Drug Deliv. Rev. 23, 3–25.

Lipinski, C.A., (2000). Drug-like properties and the causes of poor solubility and poor permeability. J. Pharm. Tox. Meth. 44, 235–249.

Lipinski, C., (2002). Poor aqueous solubility: an industry wide problem in drug discovery. Am. Pharm. Rev. 5, 82–85.

Liu, B., Hu, J., Yan, F., Turkson, R.F., Lin, F., (2016). A novel optimal support vector machine ensemble model for NOX emissions prediction of a diesel engine. Measurement 92, 183–192.

Liu, Z., Zhu, Y., Rao, R.R., Clausen, J.R., Aidun, C.K., (2018). Nanoparticle transport in cellular blood flow. Comput. Fluids 172, 609–620.

Liu, M., Li, H., Luo, G., Liu, Q., Wang, Y., (2008). Pharmacokinetics and biodistribution of surface modification polymeric nanoparticles. Arch. Pharm. Res. 31, 547–554.

Lojk, J., Bregar, V.B., Strojan, K., Hudoklin, S., Veranič, P., Pavlin, M., Kreft, M.E., (2018). Increased endocytosis of magnetic nanoparticles into cancerous urothelial cells versus normal urothelial cells. Histochem. Cell Biol. 149, 45–59.

Loscher, W., Potschka, H., (2005). Role of drug efflux transporters in the brain for drug disposition and treatment of brain diseases. Prog. Neurobiol. 76(1), 22–76.

Luo, L., Zhang, X., Hirano, Y., Tyagi, P., Barabás, P., Uehara, H., Miya, T.R., Singh, N., Archer, B., Qazi, Y., Jackman, K., Das, S.K., Olsen, T., Chennamaneni, S.R., Stagg, B.C., Ahmed, F., Emerson, L., Zygmunt, K., Whitaker, R., Mamalis, C., Huang, W., Gao, G., Srinivas, S.P., Krizaj, D., Baffi, J., Ambati, J., Kompella, U.B., Ambati, B.K., (2013). Targeted intraceptor nanoparticle therapy reduces angiogenesis and fibrosis in primate and murine macular degeneration. ACS Nano 7, 3264–3275.

Lü, J., Wang, X., Marin-Muller, C., Wang, H., Lin, P.H., Yao, Q., Chen, C., (2009). Current advances in research and clinical applications of PLGA-based nanotechnology. Expert. Rev. Mol. Diagn. 9 (4), 325–341.

Lynch, I., Salvati, A., Dawson, K., (2009). What does the cell see? Nat. Nanotechnol. 4, 546–547.

Makadia, H.K., Siegel, S.J., (2011). Poly lactic-co-glycolic acid (PLGA) as biodegradable controlled drug delivery carrier. Polymers 3 (3), 1377–1397.

Maksimenko, O., Malinovskaya, J., Shipulo, E., Osipova, N., Razzhivina, V., Arantseva, D., Yarovaya, O., Mostovaya, U., Khalansky, A., Fedoseeva, V., Alekseeva, A., Vanchugova, L., Gorshkova, M., Kovalenko, E., Balabanyan, V., Melnikov, P., Baklaushev, V., Chekhonin, V., Kreuter, J., Gelperina, S., (2019). Doxorubicin-loaded PLGA nanoparticles for the chemotherapy of glioblastoma: Towards the pharmaceutical development. Int. J. Pharm. 572, 118733.

Malam, Y., Loizidou, M., Seifalian, A.M., (2009). Liposomes and nanoparticles: nanosized vehicles for drug delivery in cancer. Trends Pharmacol. Sci. 30, 592–595

Malinovskaya, Y., Melnikov, P., Baklaushev, V., Gabashvili, A., Osipova, N., Mantrov, S., Ermolenko, Y., Maksimenko, O., Gorshkova, V., Balabanyan, M., Kreuter, J., Gelperina, S., (2017). Delivery of doxorubicin-loaded PLGA nanoparticles into U87 human glioblastoma cells. Int. J. Pharm. 524 (1-2), 77–90.

Masereeuw, R., Moons, M.M., Russel, F.G.M., (1997). Rhodamine 123 accumulates extensively in the isolated perfused rat kidney and is secreted by the organic cation system. Eur. J. Pharmacol. 321(3), 315–323.

Mao, S., Xu, J., Cai, C., Germershaus, O., Schaper, A., Kissel, T., (2007). Effect of WOW process parameters on morphology and burst release of FITC-dextran loaded PLGA microspheres. Int. J. Pharm. 334, 137–148.

Mazzeo, A., Gai, C., Trento, M., Porta, M., Beltramo, E., (2020). Effects of thiamine and fenofibrate on high glucose and hypoxia-induced damage in cell models of the inner blood-retinal barrier. Acta Diabetol. 57(12), 1423–1433.

McWhirter, J.L., Noguchi, H., Gompper, G., (2011). Deformation and clustering of red blood cells in microcapillary flows. Soft Matter 7, 10967–10977.

Mersko-Liversidge, E.M., Liversidge, G.G., (2008). Drug Nanoparticles: Formulating Poorly Water-Soluble Compounds. Toxicol. Pathol. 36, 43–48.

Morgan, J.E., Jeffery, G., Foss, A.J., (1998). Axon deviation in the human lamina cribrosa. Br. J. Ophthalmol. 82, 680–683.

Moghimi, S.M., Pavey, K.D., Hunter, A.C., (2003). Real-time evidence of surface modification at polystyrene lattices by poloxamine 908 in the presence of serum: *in vivo* conversion of macrophage-prone nanoparticles to stealth entities by poloxamine 908. FEBS Lett. 547, 177–182.

Mozaffarieh, M., Grieshaber, M.C., Flammer, J., (2008). Oxygen and blood flow: players in the pathogenesis of glaucoma. Mol. Vis. 14, 224–233.

Müller, J., Martins, A., Csábi, J., Fenyvesi, F., Könczöl, Á., Hunyadi, A., Balogh, G.T., (2017). BBB penetration-targeting physicochemical lead selection: Ecdysteroids as chemo-sensitizers against CNS tumors. Eur. J. Pharm. Sci. 96, 571–577.

Nagpal, K., Singh, S.K., Mishra, D.N., (2013). Drug targeting to brain: a systematic approach to study the factors, parameters and approaches for prediction of permeability of drugs across BBB. Expert Opin. Drug Deliv. 10(7), 927–955.

Nakano, K., Bando, Y., Tozuka, Y., Takeuchi, H., (2007). Cellular interaction of PEGylated PLGA nanospheres with macrophage J774 cells using flow cytometry. J. Pharm. Sci. 2 (6), 220–226.

Neufeld, A.H., Hernandez, M.R., Gonzalez, M., (1997). Nitric oxide synthase in the human glaucomatous optic nerve head. Arch. Ophthalmol. 115, 497–503.

Nickells, R.W., (1996). Retinal ganglion cell death in glaucoma: the how, the why, and the maybe. J. Glaucoma. 5, 345–356.

Nunan, R., Campbell, J., Mori, R., Pitulescu, M.E., Jiang, W.G., Harding, K.G., Adams, R.H., Nobes, C.D., Martin, P., (2015). Ephrin-Bs drive junctional downregulation and actin stress fiber disassembly to enable wound re-epithelialization. Cell Rep. 13, 1380–1395.

O'Brown, N.M., Pfau, S.J., Gu, C., (2018). Bridging barriers: a comparative look at the blood-brain barrier across organisms. Genes Dev. 32(7-8), 466–478.

Osborne, N.N., Casson, R.J., Wood, J.P.M., Chidlow, G., Graham, M., Melena, J., (2004). Retinal ischemia: mechanisms of damage and potential therapeutic strategies. Prog. Retin. Eye Res. 23 (1), 91–147.

Ostolska, I., Wiśniewska M., (2014). Application of the zeta-potential measurements to explanation of colloidal Cr2O3 stability mechanism in the presence of the ionic polyamino acids. Colloid Polym. Sci. 292(10), 2453–2464.

Pajouhesh, H., Lenz, G.R., (2005). Medicinal chemical properties of successful central nervous system drugs. NeuroRx. 2, 541–553.

Panyam, J., Labhasetwar, V., (2003). Biodegradable nanoparticles for drug and gene delivery to cells and tissue. Adv. Drug Deliv. Rev. 55(3), 329–347.

Pardridge W.M., (2007). Blood–brain barrier delivery. Drug Discov. Today 12(1–2), 54–61.

Pechauer, A.D., Huang, D., Jia, Y., (2015). Detecting blood flow response to stimulation of the human eye. BioMed. Res. Int. 2015, 121973

Peng, T., Six, K.M., Munson, P.L., (1970). Effects of prostaglandin E1 on the hypothalamo-hypophyseal-adrenocortical axis in rats. Endocrinology 86 (2), 202–206.

Pillunat, L.E., Anderson, D.R., Knighton, R.W., Joos, K.M., Feuer, W.J., (1997). Autoregulation of human optic nerve head circulation in response to increased intraocular pressure. Exp. Eye Res. 64, 737–744.

Pournaras, C.J., Rungger-Brändle, E., Riva, C.E., Hardarson, S.H., Stefansson, E., (2008). Regulation of retinal blood flow in health and disease. Prog. Retin. Eye Res. 27(3), 284–330.

Prilloff, S., Noblejas, M.I., Chedhomme, V., Sabel, B.A., (2007). Two faces of calcium activation after optic nerve trauma: life or death of retinal ganglion cells in vivo depends on calcium dynamics. Eur. J. Neurosci. 25(11), 3339–3346.

Prilloff, S., Fan, J., Henrich-Noack, P., Sabel, B.A., (2010a). *In vivo* confocal neuroimaging (ICON): non-invasive, functional imaging of the mammalian CNS with cellular resolution. Eur. J. Neurosci. 31 (3), 521–528.

Prilloff, S., Henrich-Noack, P., Kropf, S., Sabel, B.A., (2010b). Experience-dependent plasticity and vision restoration in rats after optic nerve crush. J. Neurotrauma 27 (12), 2295–2307.

Psiuk-Maksymowicz, K., Borys, D., Smieja, J., (2014). Magnetic resonance angiogram processing and modelling of the cerebral vascular network. Proceedings of the sixth international conference bioinformatics, biocomputational systems and biotechnologies BIOTECHNO. 59–62.

PubChem Database. National Center for Biotechnology Information. Coumarin 6, CID=100334, https://pubchem.ncbi.nlm.nih.gov/compound/coumarin-6 (accessed on July 19, 2020).

PubChem Database. National Center for Biotechnology Information. PubChem Compound Summary for CID 11968038, https://pubchem.ncbi.nlm.nih.gov/compound/Dilc18_3_-dye (accessed on August 10, 2020).

PubChem Database. National Center for Biotechnology Information. PubChem Compound Summary for CID 9929799, Rhodamine 123, https://pubchem.ncbi.nlm.nih.gov/compound/9929799 (accessed on May 12, 2021).

Qi, F., Wu, J., Fan, Q., He, F., Tian, G., Yang, T., Ma, G., Su, Z., (2013). Preparation of uniform-sized exenatide-loaded PLGA microspheres as long-effective release system with high encapsulation efficiency and bio-stability. Colloids Surf. B. 112, 492–498.

Quintanar-Guerrero, D., Allémann, E., Doelker, E., and Fessi, H., (1997). A mechanistic study of the formation of polymer nanoparticles by the emulsification-diffusion technique. Colloid Polym. Sci. 275, 640–647.

Rafiei, P., Haddadi, A., (2017). Docetaxel-loaded PLGA and PLGA-PEG nanoparticles for intravenous application: pharmacokinetics and biodistribution profile. Int. J. Nanomedicine. 12, 935–947.

Raghava, S., Hammond, M., Kompella, U.B., (2004). Periocular routes for retinal drug delivery. Expert Opin. Drug Deliv. 1(1), 99–114.

Redhead, H.M., Davis, S.S., Illum, L., (2001). Drug delivery in poly (lactide-co-glycolide) nanoparticles surface modified with poloxamer 407 and poloxamine 908: *in vitro* characterization and *in vivo* evaluation. J. Control. Release 70, 353–363.

Reese, T.S., Karnovsky M.J., (1967). Fine structural localization of a blood-brain barrier to exogenous peroxidase. J. Cell Biol. 34(1), 207–217.

Rivolta, I., Panariti, A., Lettiero, B., Sesana, S., Gasco, P., Gasco, M.R., Masserini, M., Miserochi, G., (2011). Cellular uptake of coumarin 6 as a model drug loaded in solid lipid nanoparticles. J. Physiol. Pharmacol. 62, 45–53.

Rouse, J.G., Yang, J., Ryman-Rasmussen, J.P., Barron, A.R., Monteiro-Riviere, N.A., (2007). Effects of Mechanical Flexion on the Penetration of Fullerene Amino Acid-Derivatized Peptide Nanoparticles through Skin. Nano Letters 7 (1), 155-160.

Sabel, B.A., Engelmann, R., Humphrey, M.F., (1997). *In vivo* confocal neuroimaging (ICON) of CNS neurons. Nat. Med. 3 (2), 244–247.

Sabel, B.A., Wang, J., Cárdenas-Morales, L., Faiq, M., Heim, C., Golubnitschaja, O., (2019). Flammer Syndrome: Psychological Causes and Consequences of Visual Impairment. In: Golubnitschaja O. (eds) Flammer Syndrome. Advances in Predictive, Preventive and Personalised Medicine, vol 11. Springer, Cham.

Sagaties, M.J., Raviola, G., Schaeffer, S., Miller, C., (1987). The structural basis of the inner blood-retina barrier in the eye of Macaca mulatta. Invest. Ophthalmol. Vis Sci. 28(12), 2000–2014.

Santander-Ortega, M.J., Csaba, N., Alonso, M.J., Ortega-Vinuesa, J.L., Bastos-González, D., (2007). Stability and physicochemical characteristics of PLGA, PLGA: poloxamer and PLGA: poloxamine blend nanoparticles: A comparative study. Colloids Surf. A Physicochem. Eng. Asp. 296(1-3), 132–140.

Santosh, R., Selvam, M.K., Kanekar, S.U., Nagaraja, G.K., Kumar, M., (2018). Design, Synthesis, DNA binding, and docking studies of thiazoles and thiazole-containing triazoles as antibacterials. ChemistrySelect 3, 3892.

Sato, K., Saigusa, D., Saito, R., Fujioka, A., Nakagawa, Y., Nishiguchi, K.M., Kokubun, T., Motoike, I.N., Maruyama, K., Omodaka, K., Shiga1, Y., Uruno, A., Koshiba, S., Yamamoto, M., Nakazawa, T., (2018). Metabolomic changes in the mouse retina after optic nerve injury. Sci. Rep. 8, 11930.

Schroeter, M., Jander, S., (2005). T-cell cytokines in injury-induced neural damage and repair. Neuromol. Med., 7:1–13.

Schlessinger, J., Axelrod, D., Koppel, D.E., Webb, W.W., Elson, E.L., (1977). Lateral transport of a lipid probe and labeled proteins on a cell membrane. Science 195 (4275), 307–309.

Semete, B., Booysen, L., Lemmer, Y., Kalombo, L., Katata, L., Verschoor, J., Swai, H.S., (2010). *In vivo* evaluation of the biodistribution and safety of PLGA nanoparticles as drug delivery systems. Nanomed.: Nanotechnol. Biol. Med. 6 (5), 662–671.

Simon, L.C., Sabliov, C.M., (2014). The effect of nanoparticle properties, detection method, delivery route and animal model on poly(lactic-co-glycolic) acid nanoparticles biodistribution in mice and rats. Drug Metab. Rev. 46 (2), 128–141.

Singh, R., Lillard Jr, J.W., (2009). Nanoparticle-based targeted drug delivery. Exp. Mol. Pathol. 86. 215–223.

Singh, S.R., Grossniklaus H.E., Kang S.J., Edelhauser H.F., Ambati B.K., Kompella U.B., (2009). Intravenous transferrin, RGD peptide and dual-targeted nanoparticles enhance anti-VEGF intraceptor gene delivery to laser-induced CNV. Gene Ther. 16(5), 645–659.

Sugiyama, K., Gu, Z.-B., Kawase, C., Yamamoto, T., Kitazawa, Y., (1999). Optic nerve and peripapillary choroidal microvasculature of the rat eye. Invest. Ophthalmol. Vis. Sci. 40(13), 3084–3090.

Stauffer, W., Sheng, H., Lim, H.N., (2018). EzColocalization: An ImageJ plugin for visualizing and measuring colocalization in cells and organisms. Sci. Rep. 8, 1–13.

Stewart, P.A., Tuor, U.I., (1994). Blood-eye barriers in the rat: Correlation of ultrastructure with function. J. Comp. Neurol. 340, 566–576.

Strohm, E.M., Berndl, E.S., Kolios, M.C., (2013). Probing red blood cell morphology using high-frequency photoacoustics. Biophys J. 105(1):59-67.

Song, W., Bossy, B., Martin, O.J., Hicks, A., Lubitz, S., Knott, A.B., Bossy-Wetzel, E., (2008). Assessing mitochondrial morphology and dynamics using fluorescence wide-field microscopy and 3D image processing. Methods 46 (4), 295–303.

Song, Z., Feng, R., Sun, M., Guo, C., Gao, Y., Li, L., Zhai, G., (2011). Curcumin-loaded PLGA-PEG-PLGA triblock copolymeric micelles: Preparation, pharmaco-kinetics and distribution *in vivo*. J. Colloid Interface Sci. 354, 116–123.

Tan, J., Thomas, A., Liu, Y., (2012). Influence of red blood cells on nanoparticle targeted delivery in microcirculation. Soft Matter 8, 1934–1946.

Tang, Z., Zhang, S., Lee, C., Kumar, A., Arjunan, P., Li, Y., Zhang, F., Li, X., (2011). An optic nerve crush injury murine model to study retinal ganglion cell survival. JoVE, 50.

Tharwat, A., Moemen, Y.S., Hassanien, A.E., (2017). Classification of toxicity effects of biotransformed hepatic drugs using whale optimized support vector machines. J. Biomed. Inform. 68, 132–149.

Thomas, S., Kalarikkal, N., Stephan, A.M., Raneesh, B., (2014). Advanced nanomaterials: synthesis, properties, and applications, p 182.

Thon, J.N., Italiano, J.E., (2012). Platelets: production, morphology and ultrastructure. Handb. Exp. Pharmacol. (210), 3-22.

Thrimawithana, T.R., Young, S., Bunt, C.R., Green, C., Alany, R.G., (2011). Drug delivery to the posterior segment of the eye. Drug Discov. Today. 16, 270–277.

Toda, R., Kawazu, K., Oyabu, M., Miyazaki, T., Kiuchi, Y., (2011). Comparison of drug permeabilities across the blood–retinal barrier, blood–aqueous humor barrier, and blood–brain barrier. J. Pharm. Sci.100, 3904–3911.

Tomi, M., Hosoya, K., (2010). The role of blood-ocular barrier transporters in retinal drug disposition: an overview. Expert Opin. Drug Metab. Toxicol. 6 (9), 1111–1124.

Trotter, M.W.B., Buxton, B.F., Holden, S.B., (2001). Support vector machines in combinatorial chemistry. Meas. Control. 34 (8), 235–239.

Tzankova, V., Gorinova, C., Kondeva-Burdina, M., Simeonova, R., Philipov, S., Konstantinov, S., Petrov, P., Galabov, D., Yoncheva, K., (2016). *In vitro* and *in vivo* toxicity evaluation of cationic PDMAEMA-PCL-PDMAEMA micelles as a carrier of curcumin. Food Chem. Toxicol. 97, 1–10.

Urquhart, B.L., Kim, R.B, (2009). Blood–brain barrier transporters and response to CNS-active drugs. Eur. J. Clin. Pharmacol. 65(11), 1063–1070.

Urtti A., Pipkin J.D., Rork G., Sendo T., Finne U., Repta A.J., (1990). Controlled drug delivery devices for experimental ocular studies with timolol 2. Ocular and systemic absorption in rabbits. Int. J. Pharm. 61, 241–249.

van den Berg, B.M., Vink, H., Spaan, J.A.E., (1992). The endothelial glycocalyx protects against myocardial edema. Circ. Res. 92(6), 592–594.

Voigt, N., Henrich-Noack, P., Kockentiedt, S., Hintz, W., Tomas, J., Sabel, B.A., (2014). Surfactants, not size or zeta-potential influence blood–brain barrier passage of polymeric nanoparticles. Eur. J. Pharm. Biopharm. 87 (1), 19–29.

Wajer, S.D., Taomoto, M., McLeod, D.S., McCally, R.L., Nishiwaki, H., Fabry, M.E., Nagel, R.L., Lutty, G.A., (2000). Velocity measurements of normal and sickle red blood cells in the rat retinal and choroidal vasculatures. Microvasc. Res. 60, 281–293.

Wang, A.Z., Gu, F., Zhang, L., Chan, J.M., Radovic-Moreno, A., Shaikh, M.R., and Farokhzad, O.C., (2008). Biofunctionalized targeted nanoparticles for therapeutic applications. Expert Opin. Biol. Ther. 8(8), 1063–1070.

Wang, B., He, X., Zhang, Z., Zhao, Y., Feng, W., (2013). Metabolism of nanomaterials *in Vivo*: blood circulation and organ clearance. Acc. Chem. Res. 46, 3761–769.

Wang, Y., Qu, W., Choi., S.H., (2016). FDA's regulatory science program for generic PLA/PLGA – Based drug products. Am. Pharm. Rev. 19 (4), 5-9. Retrieved from http://www.americanpharmaceuticalreview.com/Featured-Articles/188841-FDA-s-Regulatory-Science-Program-for-Generic-PLA-PLGA-Based-Drug-Products/

Watanabe, K., Nishimura, Y., Nomoto, T., Umemoto, N., Zhang, Z., Zhang, B., Kuroyanagi, J., Shimada, Y., Shintou, T., Okano, M., Miyazaki, T., Imamura, T., Tanaka, T., (2012). *In vivo* assessment of the permeability of the blood-brain barrier and blood-retinal barrier to fluorescent indoline derivatives in zebrafish. BMC Neuroscience 13,101.

Weber, A.J., Harman, C.D., Viswanathan, S., (2008). Effects of optic nerve injury, glaucoma, and neuroprotection on the survival, structure, and function of ganglion cells in the mammalian retina. J. Physiol. 586, 4393–4400.

Win, K.Y., Feng, S., (2006). *In vitro* and *in vivo* studies on vitamin E TPGS-emulsified poly(D,L-Lactic-co-Glycolic acid) nanoparticles for paclitaxel formulation. Biomaterials. 27(10), 2285–2291.

Wisniewska-Kruk, J., Hoeben, K.A., Vogels, I.M.C., Gaillard, P.J., Van Noorden, C.J.F., Schlingemann, R.O., Klaassen, I., (2012). A novel co-culture model of the blood-retinal barrier based on primary retinal endothelial cells, pericytes and astrocytes. Exp. Eye Res. 96, 181e190.

Wohlfart, S., Khalansky, A.S., Gelperina, S., Maksimenko, O., Bernreuther, C., Glatzel, M., Kreuter, J., (2011). Efficient chemotherapy of rat glioblastoma using doxorubicin-loaded PLGA nanoparticles with different stabilizers. PLoS One 6(5), e19121.

Xie, J., Farage, E., Sugimoto, M., Anand-Apte, B., (2010). A novel transgenic zebrafish model for blood-brain and blood-retinal barrier development. BMC Dev. Biol. 10, 76.

Xue, C.X., Zhang, R.S., Liu, H.X., Yao, X.J., Liu, M.C., Hu, Z.D., Fan, B.T., (2004). QSAR models for the prediction of binding affinities to human serum albumin using the heuristic method and a support vector machine. J. Chem. Inf. Comput. Sci. 44 (5), 1693–1700.

Yoganathan, A.P., Cape, E.G., Sung, H-W., Williams, F.P., Jimoh, A., (1988). Review of hydrodynamic principles for the cardiologist: Applications to the study of blood flow and jets by imaging techniques. J. Am. Coll. Cardiol. 12 (5), 1344–1353.

You, Q., Hopf, T., Hintz, W., Rannabauer, S., Voigt, N., van Wachem, B., Henrich-Noack, P., Sabel, B.A., (2019). Major effects on blood-retina barrier passage by minor alterations in design of polybutylcyanoacrylate nanoparticles. J. Drug Target. 27(3), 338–346.

Yu-Wai-Man, P., Griffiths, P.G., (2013). Steroids for traumatic optic neuropathy. Cochrane Database Syst Rev. 2013(6), CD006032.

Yue B., (2014). Biology of the extracellular matrix: an overview. J. Glaucoma, 23, S20–S23.

Zhang, E.**,** Osipova, N., Sokolov, M., Maksimenko, O., Semyonkin, A., Wang, M., Grigartzik, L., Gelperina, S., Sabel, B.A., Henrich-Noack, P., (2021). Exploring

the systemic delivery of a poorly water-soluble model drug to the retina using PLGA nanoparticles. Eur. J. Pharm. Sci., online.
https://doi.org/10.1016/j.ejps.2021.105905

Zhang, E., Zhukova, V., Semyonkin, A., Osipova, N., Malinovskaya, Y., Maksimenko, O., Chernikov, V., Sokolov, M., Grigartzik, L., Sabel, B.A., Gelperina, S., Henrich-Noacka, P., (2020). Release kinetics of fluorescent dyes from PLGA nanoparticles in retinal blood vessels: *In vivo* monitoring and *ex vivo* localization. Eur. J. Pharm. Biopharm. 150, 131–142.

Zhao, J.P., Ma, Z.Z., Song, C., Li, X.H., Li, Y.Z., Liu, Y.Y., (2010). Optic nerve lesions in diabetic rats: blood flow to the optic nerve, permeability of micro blood vessels and histopathology. Int. J. Ophthalmol. 3(4), 291-294.

Zhi, Z., Cepurna, W.O., Johnson, E.C., Morrison, J.C., Wang, R.K., (2012). Impact of intraocular pressure on changes of blood flow in the retina, choroid, and optic nerve head in rats investigated by optical microangiography. Biomed. Opt. Express 3, 2220–2233.

Appendix

I. Supplementary Figures

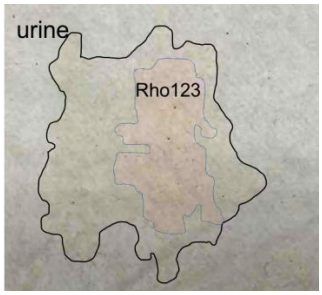

Figure S1 Rho123 was eliminated from rats at 90 min post injection showing hints on the paper.

Urine: area enclosed with black line. Rho123: area enclosed with blue line.

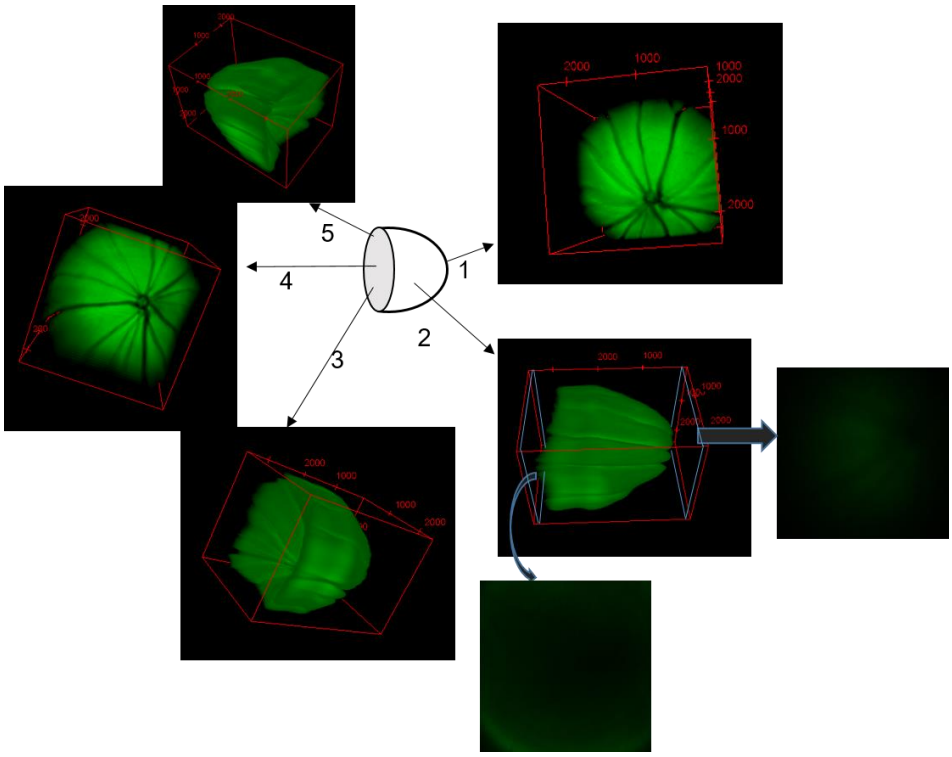

Figure S2 The possible distribution of Cou6 signal in 3D.

The preliminary 3D reconstruction of Cou6 from *in vivo* imaging. Due to the individual difference, the limitation of different eye orientation after anesthesia, the signals are captured on limited diameter of retina. Numbers 1 to 5 represent that the reconstructed 3D

Cou6 signal was observed from 5 different directions and the corresponding images to each position. The bold arrows show the top plane and the bottom plane.

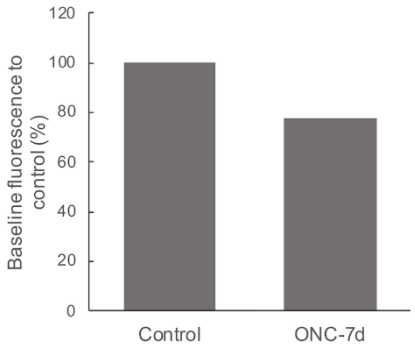

Figure S3 The baseline fluorescence of retina post optic nerve crush group by day 7 under the Cy5.5 measurement.

Control: rat without optic nerve crush. ONC-7d, rat post optic nerve crush group by day 7.

II. Supplementary Table

Table S1 Dataset used for statistical learning in Study III

Agents	MW	XLogP	HBDC	HBAC	RBC	TPSA	BBB[#]
1-hydroxymidazolam	341.8	2.7	1	4	2	50.4	P
2-Methylpentane	86.18	3.2	0	0	2	0	P
Acebutolol	336.4	1.7	3	5	10	87.7	P
Acetaminophen	151.16	0.5	2	2	1	49.3	P
Aldosterone	360.4	1.1	2	5	3	91.7	N
Aminopyrine	231.29	1	0	3	2	26.8	P
Amitriptyline	277.4	5	0	1	3	3.2	P
Amobarbital	226.27	2.1	2	3	4	75.3	P
Amphetamine	135.21	1.8	1	1	2	26	P
AmphotericinB	924.1	0	12	18	3	320	N
Aspirin	180.16	1.2	1	4	3	63.6	P
Astemizole	458.6	6	1	5	8	42.3	N
Atenolol	266.34	0.2	3	4	8	84.6	N
Atovaquone	366.8	5.2	1	3	2	54.4	N
Azelaic acid	188.22	1.6	2	4	8	74.6	N
Azithromycin	749	4	5	14	7	180	N
Beloxepin	295.4	2.8	1	3	0	32.7	P
Benzene	78.11	2.1	0	0	0	0	P
Bethanechol	161.22	0	1	2	4	52.3	N
Bretazenil	418.3	3.1	0	4	3	64.4	P
Brl 52974	393.3	2.9	1	3	4	52.2	N
Bromocriptine	654.6	3.8	3	6	5	118	N
Bromperidol	420.3	3.3	1	4	6	40.5	P
Caffeine	194.19	-0.1	0	3	0	58.4	P
Carbamazepine	236.27	2.5	1	1	0	6.3	P
Carbamazepineepoxide	252.27	1.3	1	2	0	58.9	P
Carbidopa	226.23	-2.2	5	6	4	116	N
Carebastine	499.6	3.6	1	5	11	66.8	N
Cefradine	349.4	0.4	3	6	4	138	N
Cetirizine	388.9	1.7	1	5	8	53	N
Chlorothiazide	295.7	-0.2	2	6	1	135	N
Cimetidine	252.34	0.4	3	4	7	114	N
Ciprofloxacin	331.34	-1.1	2	7	3	72.9	N
Clobazam	300.74	2.1	0	2	1	40.6	P
Clofazimine	473.4	7.1	1	4	4	40	N
Clonidine	230.09	1.6	2	1	2	36.4	P
Codeine	299.4	1.1	1	4	1	41.9	P
Colchicine	399.4	1	1	6	5	83.1	N
Corticosterone	346.5	1.9	2	4	2	74.6	N

Cortisol	362.5	1.6	3	5	2	94.8	N
CP 102	183.2	0.3	2	4	3	60.8	N
Cyclohexane	84.16	3.4	0	0	0	0	P
Daunorubicin	527.5	1.8	5	11	4	186	N
Delavirdine	456.6	2.4	3	7	6	119	N
Demeclocycline	464.9	0.7	6	9	2	182	N
Desipramine	266.4	4.9	1	2	4	15.3	P
Dexrazoxane	268.27	-1.4	2	6	3	98.8	N
Diazepam	284.74	3	0	2	1	32.7	P
Dichloromethane	84.93	1.5	0	0	0	0	p
Didanosine	236.23	-1.2	2	5	2	88.7	N
Diethylether	74.12	0.9	0	1	2	9.2	P
Difloxacin	399.4	1.6	1	8	3	64.1	N
Dihydroergotamine	583.7	2.4	3	6	4	118	N
Domperidone	425.9	3.9	2	3	5	67.9	P
Dopamine	153.18	-1	3	3	2	66.5	N
Doxorubicin	543.5	1.3	6	12	5	206	N
Ebastine	469.7	7.2	0	3	10	29.5	N
Efavirenz	315.67	4	1	5	1	38.3	N
Enalapril	376.4	-0.1	2	6	10	95.9	N
Enflurane	184.49	2.1	0	6	3	9.2	P
Enoxacin	320.32	-0.2	2	8	3	85.8	N
Epinephrine	183.2	-1.4	4	4	3	72.7	N
Ethanol	46.07	-0.1	1	1	0	20.2	P
Ethylbenzene	106.16	3.1	0	0	1	0	P
Etoposide	588.6	0.6	3	13	5	161	N
Fleroxacin	369.34	-0.1	1	9	4	64.1	N
Flumazenil	303.29	1	0	5	3	64.4	P
Flunitrazepam	313.28	2.1	0	5	1	78.5	P
Fluphenazine	437.5	4.4	1	8	6	55.2	P
Furosemide	330.74	2	3	7	5	131	N
Gabapentin	171.24	-1.1	2	3	3	63.3	P
GR-94839	414.3	1.5	1	4	4	64.1	N
Guanadrel	213.28	0	2	3	2	82.9	N
Haloperidol	375.9	3.2	1	4	6	40.5	P
Halothane	197.38	2.3	0	3	0	0	P
Heptane	100.2	4.4	0	0	4	0	P
Hexobarbital	236.27	1.5	1	3	1	66.5	P
Hydrochlorothiazide	297.7	-0.1	3	7	1	135	N
Hydroxyzine	374.9	3.7	1	4	8	35.9	P
Ibuprofen	206.28	3.5	1	2	4	37.3	P
Icotidine	379.5	2.6	2	5	9	88.5	N
Imipramine	280.4	4.8	0	2	4	6.5	P
Indometacin	357.8	4.3	1	4	4	68.5	N

Isoflurane	184.49	2.1	0	6	2	9.2	P
Isoxicam	335.34	3	2	7	2	121	N
Itraconazole	705.6	5.7	0	9	11	101	N
Kanamycin	484.5	-6.9	11	15	6	283	N
Ketorolac	255.27	1.9	1	3	3	59.3	N
L-663581	357.8	2.4	0	5	2	77	N
Lomefloxacin	351.35	-0.8	2	8	3	72.9	N
Loperamide	477	5	1	3	7	43.8	N
Loratadine	382.9	5.2	0	3	2	42.4	N
Lupitidine	413.5	1.5	2	6	10	108	N
Mannitol	182.17	-3.1	6	6	5	121	N
Meloxicam	351.4	3	2	7	2	136	N
Mepyramine	285.4	3.3	0	4	7	28.6	P
Mesoridazine	386.6	4.5	0	5	4	68.1	P
Metaraminol	167.2	-0.4	3	3	2	66.5	N
Methohexital	262.3	2.3	1	3	3	66.5	P
Methotrexate	454.4	-1.8	5	12	9	211	N
Methoxyflurane	164.96	2.2	0	3	2	9.2	P
Mianserin	264.4	3.4	0	2	0	6.5	P
Midazolam	325.8	2.5	0	3	1	30.2	P
Mifepristone	429.6	3.8	1	3	3	40.5	N
Mirtazapine	265.35	3.3	0	3	0	19.4	P
Morphine	285.34	0.8	2	4	0	52.9	P
Nafcillin	414.5	2.9	2	6	5	121	N
Nelfinavir	567.8	5.7	4	6	10	127	N
Nevirapine	266.3	2	1	4	1	58.1	P
Norfloxacin	319.33	-1	2	7	3	72.9	N
Northioridazine	356.6	5.4	1	4	4	65.9	P
Ofloxacin	361.4	-0.4	1	8	2	73.3	P
Omeprazole	345.4	2.2	1	6	5	96.3	N
Org 12962	265.66	2.5	1	6	1	28.2	P
Org 30526	271.74	3.3	1	2	0	21.3	P
ORG-13011	370.4	2.3	0	7	6	39.7	P
Oxazepam	286.71	2.2	2	3	1	61.7	P
Paraxanthine	180.16	-0.2	1	3	0	67.2	P
Pefloxacin	333.36	0.3	1	7	3	64.1	N
Pentobarbital	226.27	2.1	2	3	4	75.3	P
Phenazopyridine	213.24	1.9	2	5	2	89.6	N
Phenoxymethylpenicillin	350.4	2.1	2	6	5	121	N
Phenserine	337.4	2.3	1	4	3	44.8	P
Phenylbutazone	308.4	3.2	0	2	5	40.6	P
Phenytoin	252.27	2.5	2	2	2	58.2	P
Physostigmine	275.35	0.7	1	4	2	44.8	P
Pirenzepine	351.4	0.1	1	5	2	68.8	P

Piroxicam	331.3	3.1	2	6	2	108	N
Promazine	284.4	4.5	0	3	4	31.8	P
Promethazine	284.4	4.8	0	3	3	31.8	P
Propranolol	259.34	3	2	3	6	41.5	P
Quinine	324.4	2.9	1	4	4	45.6	N
Ranitidine	314.41	0.3	2	7	9	112	N
Risperidone	410.5	2.7	0	6	4	61.9	P
Ritonavir	720.9	6	4	9	18	202	N
RO19-4603	319.4	1.9	0	5	3	92.7	P
Rufloxacin	363.4	-0.3	1	8	2	89.4	N
Salbutamol	239.31	0.3	4	4	5	72.7	N
Saphris	401.8	3.9	2	6	2	87.1	P
Saquinavir	670.8	4.2	5	7	13	167	N
Sparfloxacin	392.4	0.1	3	9	3	98.9	N
Streptomycin	581.6	-8	12	15	9	336	N
Streptozotocin	265.22	-1.4	5	8	2	152	N
Sulforidazine	402.6	4.6	0	5	4	74.3	P
Teflurane	180.93	2.6	0	4	0	0	P
Temelastine	442.4	3.7	2	4	8	79.3	N
Tenoxicam	337.4	1.1	2	7	2	136	N
Terfenadine	471.7	6.6	2	3	9	43.7	N
Theobromine	180.16	-0.8	1	3	0	67.2	P
Theophylline	180.16	0	1	3	0	69.3	P
Thiopental	242.34	2.9	2	3	4	90.3	P
Thioridazine	370.6	5.9	0	4	4	57.1	P
Tibolone	312.4	2.4	1	2	1	37.3	P
Triazolam	343.2	2.4	0	3	1	43.1	p
Trichloroethylene	131.38	2.6	0	0	0	0	P
Trichloromethane	119.37	2.3	0	0	0	0	P
Trifluoperazine	407.5	5	0	7	4	35	P
Trimetrexate	369.4	2.5	3	8	6	118	N
Vancomycin	1449.2	-2.6	19	26	13	531	N
Verapamil	454.6	3.8	0	6	13	64	P
Zidovudine	267.24	0	2	6	3	93.2	P
Zolantidine	381.5	5.4	1	5	8	65.6	P

The values of corresponding chemical and physical descriptors of the molecules were obtained from PubChem Database produced by National Center for Biotechnology Information, 2020 (https://pubchem.ncbi.nlm.nih.gov; Kim et al., 2019). #: The permeabilities of selected agents were referred to a previous study (Li et al., 2005). (P: blood-brain barrier permeable agent; N: blood- brain barrier non-permeable agent).

Ehrenerklärung

Ich versichere hiermit, dass ich die vorliegende Arbeit ohne unzulässige Hilfe Dritter und ohne Benutzung anderer als der angegebenen Hilfsmittel angefertigt habe; verwendete fremde und eigene Quellen sind als solche kenntlich gemacht.

Ich habe insbesondere nicht wissentlich:

- Ergebnisse erfunden oder widersprüchliche Ergebnisse verschwiegen,
- statistische Verfahren absichtlich missbraucht, um Daten in ungerechtfertigter Weise zu interpretieren,
- fremde Ergebnisse oder Veröffentlichungen plagiiert,
- fremde Forschungsergebnisse verzerrt wiedergegeben.

Mir ist bekannt, dass Verstöße gegen das Urheberrecht Unterlassungs- und Schadenersatzansprüche des Urhebers sowie eine strafrechtliche Ahndung durch die Strafverfolgungsbehörden begründen kann.

Ich erkläre mich damit einverstanden, dass die Arbeit ggf. mit Mitteln der elektronischen Datenverarbeitung auf Plagiate überprüft werden kann.

Die Arbeit wurde bisher weder im Inland noch im Ausland in gleicher oder ähnlicher Form als Dissertation eingereicht und ist als Ganzes auch noch nicht veröffentlicht.

Magdeburg, 14.07.2021

Enqi Zhang